MORPHOLOGICAL STUDIES OF IONIC RANDOM GRAFT COPOLYMERS BASED ON SCATTERING TECHNIQUES

by

Rasoul Narimani
M.Sc., Isfahane University of Technology, 2006
B.Sc., Isfahane University of Technology, 2003

Thesis submitted in partial fulfillment
of the requirements for the degree of
Doctor of Philosophy

in the
Department of Physics
Faculty of Science

SIMON FRASER UNIVERSITY
Fall 2012

APPROVAL

Name:	Rasoul Narimani
Degree:	Doctor of Philosophy
Title of Thesis:	Morphological studies of ionic random graft copolymers based on scattering techniques
Examining Committee:	Dr. J. Steven Dodge, Associate Professor Chair
	Dr. Barbara J. Frisken Senior Supervisor, Professor
	Dr. Steven Holdcroft Supervisor, Professor, Department of Chemistry
	Dr. Michael Eikerling Supervisor, Professor, Department of Chemistry
	Dr. Karen Kavanagh Supervisor, Professor
	Dr. Michael Plischke Internal Examiner, Professor Emeritus
	Dr. Olivier Diat External Examiner, Researcher, Institut de Chimie Séparative de Marcoule (ICSM)
Date Approved:	December 17, 2012

Partial Copyright Licence

The author, whose copyright is declared on the title page of this work, has granted to Simon Fraser University the right to lend this thesis, project or extended essay to users of the Simon Fraser University Library, and to make partial or single copies only for such users or in response to a request from the library of any other university, or other educational institution, on its own behalf or for one of its users.

The author has further granted permission to Simon Fraser University to keep or make a digital copy for use in its circulating collection (currently available to the public at the “Institutional Repository” link of the SFU Library website (www.lib.sfu.ca) at http://summit/sfu.ca and, without changing the content, to translate the thesis/project or extended essays, if technically possible, to any medium or format for the purpose of preservation of the digital work.

The author has further agreed that permission for multiple copying of this work for scholarly purposes may be granted by either the author or the Dean of Graduate Studies.

It is understood that copying or publication of this work for financial gain shall not be allowed without the author’s written permission.

Permission for public performance, or limited permission for private scholarly use, of any multimedia materials forming part of this work, may have been granted by the author. This information may be found on the separately catalogued multimedia material and in the signed Partial Copyright Licence.

While licensing SFU to permit the above uses, the author retains copyright in the thesis, project or extended essays, including the right to change the work for subsequent purposes, including editing and publishing the work in whole or in part, and licensing other parties, as the author may desire.

The original Partial Copyright Licence attesting to these terms, and signed by this author, may be found in the original bound copy of this work, retained in the Simon Fraser University Archive.

Simon Fraser University Library
Burnaby, British Columbia, Canada

revised Fall 2011

Abstract

In this work, we have studied the morphology of an ionic random graft copolymer, partially sulfonated poly([vinylidene difluoride-*co*-chlorotrifluoroethylene]-*g*-styrene) [P(VDF-*co*-CTFE)-*g*-sPS], using small angle X-ray and neutron scattering (SAXS and SANS), and wide angle X-ray scattering (WAXS) techniques. SAXS and SANS measurements were used to investigate the phase separation and morphology of the polymer at nano-scale lengthscales, and WAXS measurements were used to determine the degree of the crystallinity of the polymer. We have developed a self-consistent morphological model for the studied system. In this model, dry samples consist of quasi-spherical fluorous domains embedded in a continuous phase of partially sulfonated polystyrene. We were able to characterize the size and spacing of the domains and also quantify the degree of phase separation. Our analysis shows that crystallinity acts as a hindering factor in the phase separation of the fluorous domains. Moreover, we find that, generally, partially sulfonated samples possess a less-developed phase separation than the unsulfonated or fully sulfonated samples. The morphology of the wet samples consists of fluorous domains as well as quasi-spherical water-rich domains. We find that samples swell homogeneously at the nano-scale level and that the swelling is consistent with water content measurements for these samples, as long as the water content is $< 80\%$ vol. We have also characterized the spherical water-rich domains of the samples and argue that these water-rich domains are connected with nano-channels of water containing ionic acid groups. Our results suggest that conductivity of the membrane is proportional to the size of the spherical water-rich domains and to the water volume associated with each domain, but is inversely proportional to the spacing between them.

Keywords: Ionic random graft copolymer, morphology, phase separation, proton exchange membranes, structure-morphology-property relationships

Acknowledgments

First and foremost, I would like to thank my supervisor Prof. Barbara Frisken for giving me the opportunity to pursue this degree. I am thankful to Prof. Steven Holdcroft for his critical comments which shaped this project to completeness and also for his being on my supervisory committee. I am grateful to Dr. Laurent Rubatat whom kindly helped me to understand the scattering concepts and also helped with the SANS measurements. I am thankful to the supervisory committee, Prof. Michael Ekerling and Prof. Karen Kavanagh who supplied me with great ideas along the way. I am also in debt to Steve Launspach at NINT for teaching me how to use the SAXS instrument and helped me with running the experiments. I would like to thank Dr. Emily M. W. Tsang and Ms. Ami C. C. Yang for providing the samples and their results. I am really thankful to Jennifer Kauppila, Colin Truncik, Payam Mousavi, Thomas Weissbach for reading the thesis and providing me excellent feedbacks on my writing. I would like to express my gratitude to all the members of the Frisken lab through the years, particularly David Lee and Dr. Gabriel Espinosa. Many thanks to Prof. Martin Zuckermann, Dr. Mohammd Izadi, Ali Amiri, Mehran Shaghaghi and Dr. Kamaran Kaveh for their insightful discussions.

Finally I want to thank my family for their support. Especially, I like to thank my best friend and my wife, Fahameh, who was encouraging, supportive and patient.

"A model should be as simple as possible but not simpler." -Albert Einstein

This thesis is dedicated to the memory of my grandma

Contents

List of Figures

List of Tables

Chapter 1

Introduction

This thesis provides a comprehensive morphological study of a polymeric system, an ionic random graft copolymer. We have used wide angle X-ray scattering (WAXS), and small angle X-ray and neutron scattering (SAXS and SANS) techniques to investigate the morphologyof the polymeric membrane samples. The studied polymeric system is known as partially sulfonated poly([vinylidene difluoride-*co*-chlorotrifluoroethylene]-*g*-styrene) [P(VDF-*co*-CTFE)-*g*-sPS]. To the best of our knowledge, we are the first group to thoroughly investigate the morphology of this type of copolymer by scattering techniques. The initial motivation of synthesizing this material was to examine its properties as polymer exchange fuel cell membranes (PEMFCs) [1]. Therefore, this study has significance to two different subjects of interest: phase separation of ionic random graft copolymers, and morphology-property relations in PEMFCs. The first aspect is one of the active areas in polymer science and will be reviewed in the next chapter. In this chapter, we will describe the second aspect, which is the technological point of interest. At the end of this chapter, we provide an outline of the thesis.

The most important component of the PEMFC is the membrane electrolyte assembly (MEA). The MEA consists of three distinct components: gas diffusion layers, two catalyst layers and a polymer membrane. In the case of hydrogen fuel cell, hydrogen molecules dissociate into protons and electrons at the anode layer and then protons travel through the membrane while electrons create an external current. At the cathode, oxygen molecules combine with protons and electrons to create water. It is the membrane component which is responsible for preventing the mixing of the reactant gases and conducting the protons, while minimizing water crossover [2, 3, 4].

Polymer electrolyte membranes (PEMs) are consist of so-called ionomers which are ion containing polymers. The existence of the acid-bearing functionalities is the deterministic factor in proton conduction. The ion content of the ionomer is expressed in terms of the ion exchange capacity (IEC), which is defined as millimoles of ions per gram of dry material. Ion content is a quantity that can be measured experimentally. Also, it is possible to calculate the expected IEC value for a given chemical structure. [5, 6]. The acid functional groups are highly hydrophilic, and therefore, in the presence of water, the ionomers undergoes nano-phase separation into hydrophobic and hydrophilic domains [6, 7, 8, 9]. This self-organization is due to the minimization of the free energy of the ionomer-water system. In this case, the free energy depends on electrostatic forces between charges, osmotic pressure and mechanical forces due to the polymer matrix. In addition to these factors, environmental conditions such as temperature and method of preparation, have significant effects on the nano-phase morphology of the membrane [6, 10, 11, 12].

The morphology of the membrane, especially the formation of hydrophilic domains, is one of the main factors in the proton conduction of the membrane. Since proton conduction occurs in the hydrated domains, it depends on how well the water domains are connected. In terms of developing new materials for PEM, it is essential to understand how the morphologies of the hydrophobic and hydrophilic domains are affected by the chemical architecture of the polymer, and more importantly, how these morphologies affect the other properties, such as water uptake and conductivity [2, 9]. Although an extensive amount of work has been done in this respect, a fundamental understanding on the structure-morphology-property relationships in PEM has not yet been achieved [2, 10, 11].

The main experimental techniques to examine the morphology of PEM materials are transmission electron microscopy (TEM) and scattering techniques such as wide angle X-ray scattering (WAXS), small angle X-ray and neutron scattering (SAXS and SANS) [5, 13, 14]. Nafion is one of the most widely studied PEM materials to which these techniques have been applied. Several morphological models were proposed to explain the nano-phase septation of this materials, the most famous ones are (1) the local order model [15], (2) rod-like structure [16, 17], (3) network structure [6] and (4) parallel nano-channels [18]. Despite the huge amount of research on Nafion, there is still disagreement regarding its morphology [4, 10, 19, 20, 21]. One alternative approach to gain insight into structure-morphology-property relationships in PEM materials is to design new model polymer systems with controlled morphologies [1, 12, 4, 20]

In this thesis, we have studied the morphology of [P(VDF-*co*-CTFE)-*g*-sPS] membranes. These materials were synthesised in Steven Holdcroft's research lab at Simon Fraser University, in order to systematically study the structure-morphology-property relationships of PEM materials [1, 22]. A preliminary information about the morphology was provided through TEM measurements on dry stained samples and a basic model was proposed to explain the aggregation of the ionic acid groups [1]. This thesis provides a comprehensive morphological study and is based on three different scattering techniques: wide angle X-ray scattering (WAXS), small angle X-ray and neutron scattering (SAXS and SANS). The results of this study include a self-consistent model that can explain how different factors, such as crystallinity, affect the phase separation of the membranes, and under what circumstances the phase separation affects the water absorption of the membrane. The formation of different phases have been quantitatively characterized, and we suggest how the details of morphology, such as size of water domains and their connectivity, can be related to conductivity.

In chapter 2, I will describe general properties of these materials, including the phase separation of the ionic random copolymer, and will review the previous work on the properties of these materials. I will also describe the overall pattern of the TEM images and will provide a Matlab simulation which enhances the capabilities of the proposed model.

Chapter 3 provides the background on experimental techniques and instrumentation. I will discuss the length scale that each technique probes and provide a brief comparison of the capabilities of different instruments. The conditions under which the scattering data were measured will also be explained in this chapter.

The samples that we examined provide a profound basis for systematically examining the effect of crystallinity on the desired properties of the membrane.

In Chapter 4, I will first review different viewpoints on the significance of the crystallinity in the PEM materials. Subsequently, I will describe how the crystallinity of materials is studied, using WAXS measurements and determine how the crystallinity of our samples is affected by the microstructure of the materials.

In Chapter 5, I investigate the phase separation of the fluorous segments of the polymer using both SAXS and SANS measurements on dry and hydrated samples, respectively. According to the review paper published by Wang *et al.* [23], no other group has characterized the fluorous domains in these materials using scattering techniques. In this study, we characterized these domains by fitting the Kinning-Thomas model to the

SAXS and SANS data corresponding to dry and hydrated samples, respectively. The Kinning-Thomas model describes the morphology of spherical domains with random radii scattered randomly in a continuous matrix. Best fit curves, in remarkable agreement with the data, were obtained for both the data corresponding to dry and hydrated samples. I discuss how sulfonation and water absorption affect the morphology of the fluorous domains. Moreover, I will describe how the swelling at the nano-scale is related to the water content values of the membrane. I will also suggest which factors under what conditions can affect the water content properties of these membranes.

Chapter 6 focuses on the water-rich domains. I will first review the different morphological models of PEM materials and address how scattering intensities of these materials have been interpreted, especially the puzzling characteristic peak known as ionomer peak. Diverse ideas have been proposed regarding the origin of this characteristic peak of PEM materials. I will present our SANS data on hydrated samples and rationalize the scattering entities corresponding to each scattering feature. Next, I will describe how the morphological model was fitted to the scattering data. The proposed model is verified based on different approaches to make sure it is self-consistent. Our results indicate that the puzzling SANS feature, the ionomer peak, corresponds to the scattering from spherical water-rich domains. Moreover, my analysis indicates that the total volume of the water-rich domains is less than the total volume of water available in the membrane. Therefore, I suggest that the extra water participate in forming nano-channels of water. Although, the scattering data do not show any evidence of these water nano-channels, their existence is necessary to explain the connectivity of the spherical water domains, as has been suggested by other groups [21, 24]. However, Beers and Barsara [21] claimed that these water nano-channels are ion-free. I argue that, at least for the studied materials, these channels are ionic, and in fact non-aggregated acid groups are the origin of these channels. Finally, I will use a empirical approach to find the correlation between conductivity and details of the morphology of water-rich domains. This approach was proposed by Balog *et al.* [24] and provides compelling support of for our results.

In the last chapter we will discuss the open questions pertaining this study and suggest strategies to resolve them.

Chapter 2

Materials and properties

2.1 General description of the materials

Polymers are large molecules that consist of many smaller molecular units. These units, known as monomers, are linked by covalent bonds. The synthesis of a polymer is a chemical reaction called polymerization and the number of monomers along the polymer chain is called the degree of polymerization. The polymer architecture is the way in which the polymer chain branches. It can be linear, ring, star-branched, comb, *etc*[25].

Depending on their chemical identity, polymers are classified into two categories: homopolymers and copolymers. A homopolymer is a polymer that contains only one type of monomer. Although one chemical identity is enough to express homopolymers, other factors such as degree of polymerization and architecture have a significant effect on the physical properties of homopolymers. Copolymers, on the other hand, consist of different types of monomers. Their properties depend on both the chemical composition of the monomer types and the sequence in which different types of monomers are linked. Therefore, copolymers have unique properties and it is possible to obtain the desirable physical properties by linking suitable monomers when engineering the copolymers. For example, a material comprising hydrophobic behaviour and good mechanical integrity can be obtained by combining a highly hydrophobic polymer with a polymer which has good mechanical integrity [26].

Copolymers can be categorized based on their architectures, the most famous ones being diblock, triblock, starblock, random multiblock and graft architectures. Figure 2.1 schematically illustrates some of these architectures [27]. The simplest cases of copolymers are when the polymer chains consist of only two types of monomers and has a linear

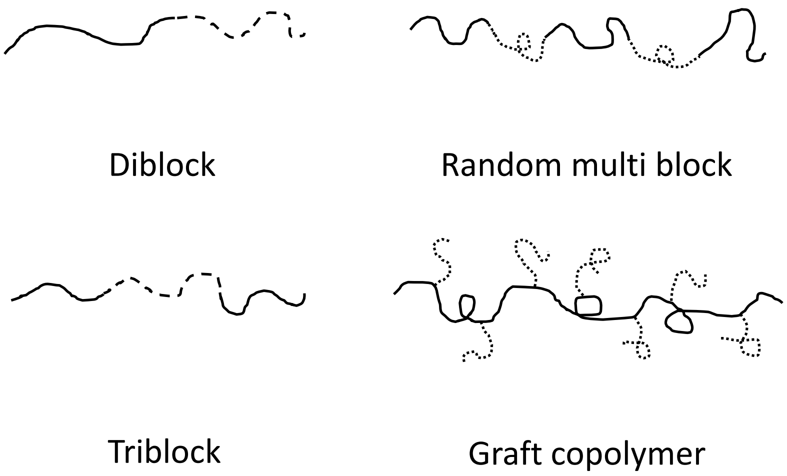

Figure 2.1: Some block copolymer architectures. Solid and dashed lines represent two different polymer chains, representing two different types of the block building the copolymer. [27].

architecture. Depending on the sequence in which monomers are linked, we can define three categories: alternating, random and, block copolymers. The configuration of the monomer in an alternating copolymer is $\cdots-\mathrm{A}-\mathrm{B}-\mathrm{A}-\mathrm{B}-\mathrm{A}-\mathrm{B}-\mathrm{A}-\mathrm{B}-\cdots$ or $(-\mathrm{A}-\mathrm{B}-)_{\mathrm{n}}$, in which A and B are the two different monomer types. For a random copolymer, however, there is no ordered configuration. An example of such a copolymer is $\cdots-\mathrm{B}-\mathrm{A}-\mathrm{B}-\mathrm{B}-\mathrm{A}-\mathrm{A}-\mathrm{B}-\mathrm{A}-\cdots$. On the other hand, block copolymers are made of blocks of different types, in which each block contains several monomers of the same type. If the copolymer contains only two blocks, it is called diblock. Similarly, in the case of three blocks, the copolymer is known as triblock. The copolymer that we investigate in this work is a graft copolymer. A graft copolymer is a copolymer which consists of a backbone with side chains attached to it [27].

Microphase separation of block copolymers is remarkable. At high temperatures chains of the copolymer are mixed homogeneously, as in any polymeric system. However, by decreasing the temperature, different blocks of the copolymer tend to segregate due to their chemical dissimilarities. The interaction between the blocks is usually expressed in terms of a reduced parameter $\chi_{AB}N$, where χ_{AB} is the Flory-Huggins parameter, which depends on the incompatibility of the monomers and the temperature, and N is the copolymer degree of polymerization. At lower temperatures, as monomers tend to segregate, nano-scale domains form in the copolymer and microphase separation occurs, as shown schematically in Fig. 2.2. Copolymers do not form macrophases as their blocks are linked together.

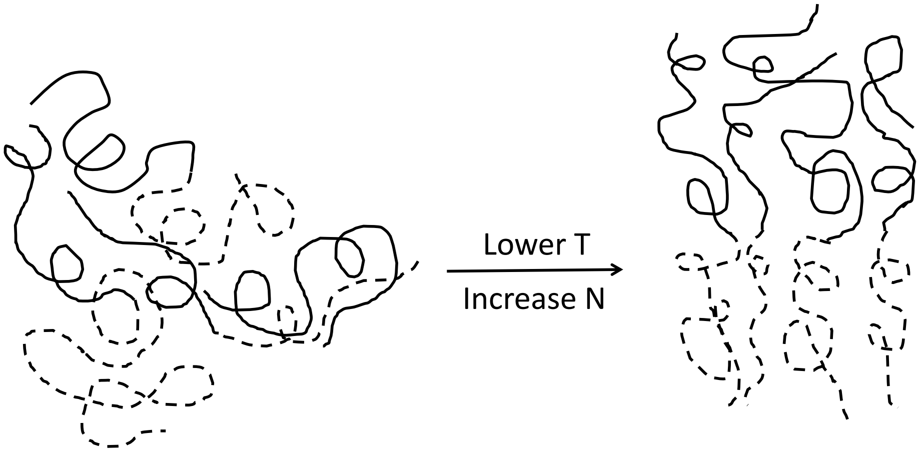

Figure 2.2: Microphase separation in a diblock copolymer melt. A diblock copolymer consists of two blocks, represented by the solid and dashed lines. These blocks tend to phase separate and form an interface at low temperature[27].

The phase diagram of non-charged copolymers having simpler architectures, in particular diblock copolymers, has been investigated extensively. In the case of diblock copolymers, this phase diagram is expressed in terms of the Flory-Huggins parameter and the volume fraction of one of the phases [28]. However, the phase diagrams of more complicated architectures, such as random graft copolymers, have not yet been explored in significant detail and this field is an active area in polymer science [23, 29, 30]. A random graft copolymer is a graft copolymer in which the positions of the side chains along the backbone are randomly located. In addition to the chemical composition of the blocks that make a graft copolymer, a graft system is distinguished by two other parameters: the average density of side chains as compared to the total number of backbone monomers *i.e.* the graft number density GD, and the average polymerization degree of side chains or the length of the side chains n. In fact, the main challenge in investigating graft copolymers is the complicated synthesis process used to produce them. In practice, the big challenge is to obtain random graft copolymers with narrow molecular weight, that have a well defined graft number density [1, 23, 29, 31, 32].

Another active area in this field is the phases formed and the phase diagram of charged copolymers. Charged polymers are also known as ionomers or ionic polymers. When a copolymer is charged, coulombic interactions play a significant role in phase separation. Since coulombic interactions are long-range, establishing a theoretical framework to explain the phase separation is a big challenge [23, 33]. In Chapter 5, we will review some of the most recent morphological oriented work on these systems and address the challenges that polymer scientists are facing within this area.

We should point out that the phase diagram described in theory, is the equilibrium phase diagram within reasonable experimental times. However, factors such as crystallinity can prevent the system from reaching equilibrium. In crystallizable block copolymers, crystalline domains consist of the extended or folded polymer chains rather than a coiled configurations. Figure 2.3 shows an example of such a configuration for a crystallizable diblock system. It has been suggested that the crystallinity can affect morphology and vice versa. The physics of crystalline polymers, is another frontier of polymer physics [25, 27].

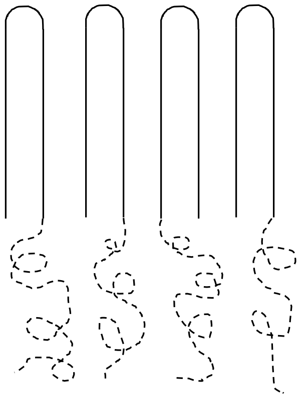

Figure 2.3: Typical configuration of the polymer chains in a crystalline diblock copolymer. [27].

In this thesis, we are dealing with an ionic random graft system which can exhibit crystallinity depending on the details of its architecture and its chemical structure. Therefore, this study covers concepts such as phase separation of random graft copolymers, phase separation of ionic copolymers and also the effect of crystallinity on the phase separation of these systems. We believe that our research can benefit different active areas of polymer science. Moreover, the materials that we are studying were, originally, synthesized in order to investigate structure-morphology-property relations of fuel cell membranes. This is another contribution that we will provide towards materials science, while investigating these ionic random graft systems.

2.2 Material synthesis and membrane casting

In this project, we will investigate two series of fluorous graft copolymers bearing ionic side chains. Each series is distinct based on its graft number density. These materials were synthesized in Steve Holdcroft's lab at Simon Fraser University. Synthesis and characterization of these two series of samples were the focus of two PhD projects completed by Dr. Emily Tsang and Ms. Ami Yang. All the experimental data presented in this chapter are provided by them. They also provided all of the samples we used in our scattering measurements.

One of the goals of our collaboration is to investigate how the details of graft architecture, such as graft number density and length of the side chains, affect the other properties of the studied graft copolymer. Figure 2.4 shows the chemical structure of the studied graft system. This graft copolymer consists of a fluorous backbone and polystyrene (PS) side chains. The fluorous backbone is hydrophobic and responsible for the mechanical properties of the membrane. On the other hand, the side chains can be sulfonated to various degree and, thus, become highly hydrophilic. In this material, the density of the side chains, length of the side chains and sulfonation degree of the side chains can be controlled during the synthesis process, making it a great candidate to investigate the structure-morphology-property relations of fuel cell membranes.

Graft copolymers can be synthesized by different methods including graft atomic transfer radical polymerization (ATRP). This method is considered to be a controlled radical polymerization and provides well-defined and less-polydisperse copolymers compared to other methods such as free-radical polymerization [34]. The key point in synthesizing graft architecture by the ATRP method is the macroinitiator, which plays the role of the backbone in the final chemical structure of the graft system. As shown in Fig. 2.6, by distributing the active sites along the macroinitiator, polymerization from the active sites leads to a graft architecture. In practice, not all of the active sites become exposed to the reaction and lead to a side chain, hence, the graft number density is less than the original density of active sites along the macroinitiator.

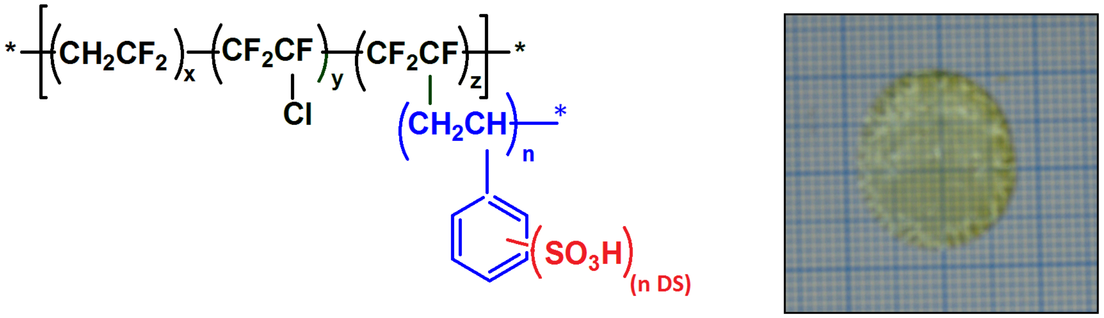

Figure 2.4: Chemical structure of poly([vinylidene diflouride-co-chlorotriflouroethylene]-g-styrene) is shown on the left hand side. The right hand figure shows photo of a typical membrane looks. The size of the major grid is 1 cm.

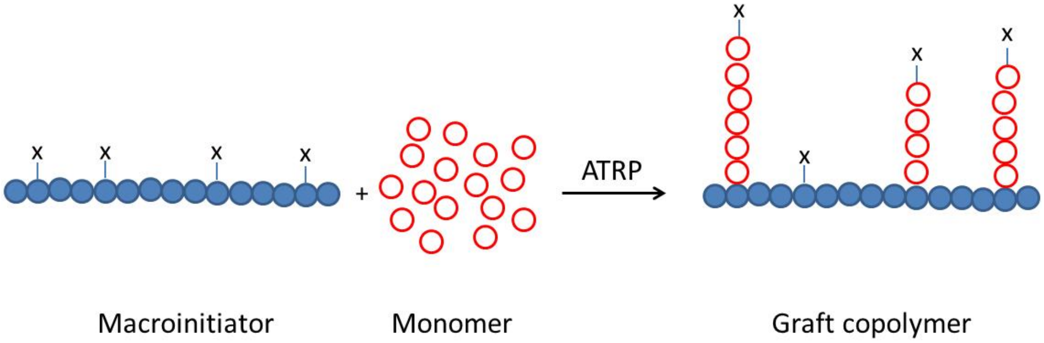

Figure 2.5: Schematic representing the approach to obtain graft copolymers by ATRP. The active sites along the macroinitiator are the key points for polymerization of the side chains necessary to obtain this architecture.

To obtain each graft series, two macroinitiators of poly (vinylidene difluoride-*co*-chlorotrifluoroethylene) (P[VDF-*co*-CTFE]) were prepared, possessing CTFE contents of 5.8 and 2.6 mol%. CTFE sites are the active sites suitable for the polymerization of polystyrene (PS) side chains. ATRP method was utilized to synthesize P[VDF-*co*-CTFE]-g-PS. Longer side chains were obtained by simply running the polymerization process for a longer time. Three different lengths of side chains were acquired based on each macroinitiator. Details of the chemical structure, such as length of the side chain were examined by H^1 nuclear magnetic resonance (H^1 NMR) spectroscopy. Figure 2.4 shows the chemical composition of the samples and Table 2.1 contains details for each set of samples. For simplicity, we refer to the series based on macroinitiators possessing CTFE content of 2.6 and 5.8 mol% as series of low and high graft number densities (LGD and HGD), respectively.

Samples with different ion content values were obtained via sulfonation, a chemical reaction that introduces SO_3 acid groups to the PS monomers. The degree of sulfonation DS is defined as the percent of sulfonated PS (sPS) monomers, expressed by

$$\mathrm{DS} = \frac{n_{\mathrm{sPS}}}{n} , \tag{2.1}$$

in which, n_{sPS} is the average number of sulfonated PS monomers in one side chain and n is the corresponding length of the side chain. Graft samples were sulfonated up to 60% for the HGD series and even up to 100% for the LGD series. The sulfonation process involves using acetyl sulfate as the sulfonating reagent. The advantage of this sulfonation method is that it provides a relatively slow sulfonation rate, thus the sulfonation degree can be controlled by the reaction time. The DS was measured by H^1 NMR spectroscopy. The distribution of acid groups along the side chains cannot be examined. Similarly, it is not possible to determine the distribution of side chains along the backbone, experimentally. However, it is assumed that both of these distributions are random [1].

To examine the properties of these materials, they were cast into the membranes and then protonated. The casting method was a simple drop cast method. The polymeric samples were dissolved in N,N-dimethylacetamide and drop cast onto a Teflon sheet. The membranes were dried at room temperature for 2 days. During this process, the membrane was covered with a lid so that it was exposed to solvent vapour. The membranes were then kept at 60° C in an oven overnight to remove residual solvent. The thickness of the acquired membranes was $\sim 100\ \mu$m. The membranes were protonated by immersing them in 2M HCl for at least four hours. The protonated membranes were rinsed with deionized water to remove the excess acid on the surface of the membranes.

The remaining sections of this chapter summarizes the properties of the polymers used, including mass-volume relationships, ion exchange capacity (IEC), water content, and conductivity. Then we review the TEM results and describe the previous model and address what aspect of this model was not correct. In the last section, we summarize the approach

	x	y	z	GD	n	Fluorous mass ratio	Fluorous vol. ratio	ρ_{unsulf} (g/cm^3)
LGD ($CTFE$ 2.6%)	1830	17	32	1.7	(■) 39 short	0.49	0.36	1.32
					(▲) 62 medium	0.38	0.26	1.25
					(●) 79 long	0.31	0.21	1.21
HGD ($CTFE$ 5.8%)	4375	164	105	2.3	(□) 35 short	0.46	0.33	1.30
		151	119	2.6	(△) 88 medium	0.22	0.14	1.16
		151	118	2.7	(○) 154 long	0.13	0.08	1.11

Table 2.1: We studied two series of ionic graft copolymers. These series were made from macroinitiators containing 2.6 and 5.8% CTFE, respectively. x, y, z and n are specified in Fig. 2.4. GD stands for graft number density and n is the average polymerization degree of the side chains. The fluorous mass ratio of the unsulfonated samples is defined as $\frac{M_{PVDF}}{(M_{PS}+M_{PVDF})}$, where M_{PS} is the mass of polystyrene side chains and M_{PVDF} is the mass of backbone in the polymer. Fluorous volume ratio is calculated based on the PVDF mass ratio and the density of the polymer as explained in Section 2.3.1. ρ_{unsulf} is the mass density of the unsulfonated sample.

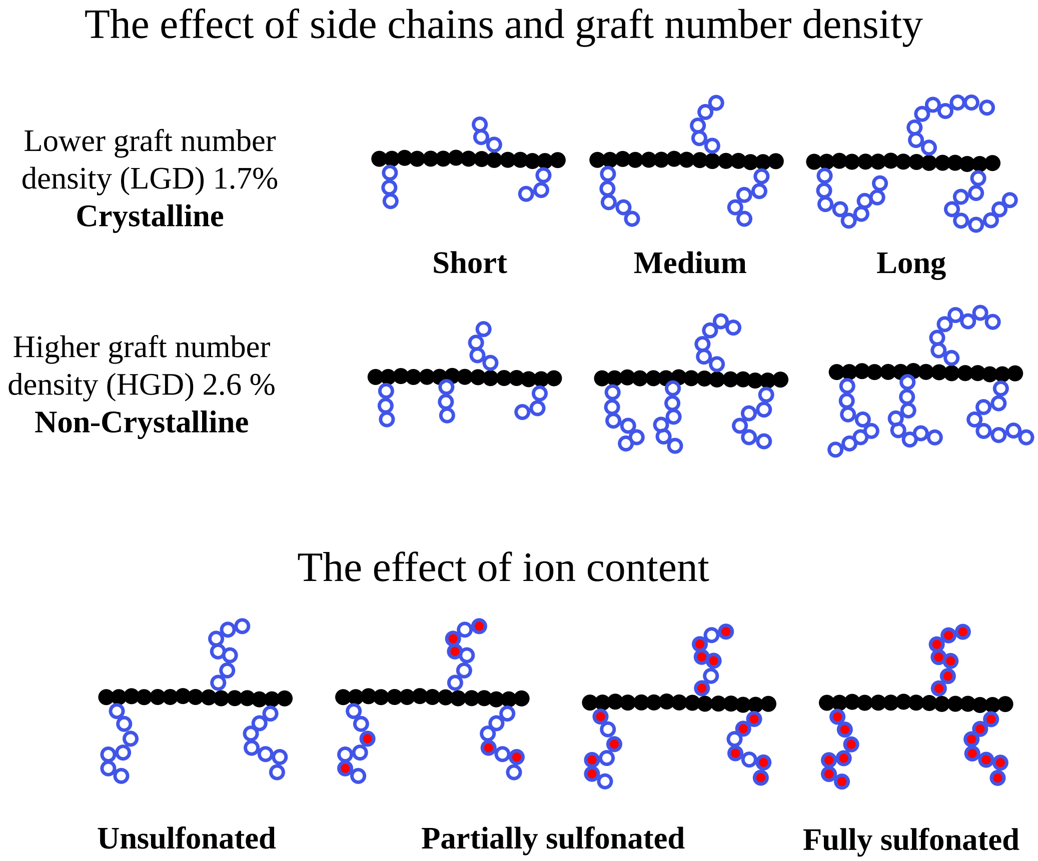

Figure 2.6: Schematic representing the approach to investigate the effect of side chains, graft number density and ion content on the morphology of the studied material.

that we have taken in order to investigate the structure-morphology-property relationships and indicate what characteristics of our study make it distinguishable from similar studies.

2.3 Properties

For this polymer, the hydrophobic backbone is responsible for the mechanical integrity of the membrane, while the side chains, which can be ionic to different degrees, are responsible for the hydrophilic parts. The balance between these two phases is crucial in order to acquire a membrane with good conductivity, yet acceptable mechanical integrity [1]. In this section, we will discuss how the mass densities and volume ratios of these two phases are related to mass ratios and sulfonation degrees. Then we summarize the results of the water content and conductivity of the membranes as reported by Dr. Tsang and Ms. Yang.

2.3.1 Mass, volume and density

Because theories for phase separation in block copolymers and scattering techniques deal with volume ratios, we need to know what are the volume ratios of different blocks. Mass-based quantities are connected to the volume-based quantities by the mass densities. Below, we calculate the mass densities of the different blocks and also introduce other useful parameters, such as the change in volume ratios upon sulfonation.

The mass densities of the PVDF, polystyrene and sulfonated polystyrene are taken from the literature and are ρ_{pvdf}=1.8, ρ_{ps}=1.05 and ρ_{sps}=1.44 g/cm^3, respectively [12, 33, 35]. The mass density of the PVDF depends on its degree of crystallinity, and hence, possesses an uncertainty of 10% [12]. Also this does not take into account the CTEF component: ρ_{ctfe}=2.1 g/cm^3 [35]. The mass density of the unsulfonated samples ρ_{unsulf} can be calculated based on the mass ratio of backbone to PS $\alpha_{\mathrm{m}}=\frac{M_{\mathrm{pvdf}}}{M_{\mathrm{ps}}}$

$$\rho_{\mathrm{unsulf}} = \frac{\alpha_{\mathrm{m}}+1}{\frac{\alpha_{\mathrm{m}}}{\rho_{\mathrm{pvdf}}}+\frac{1}{\rho_{\mathrm{ps}}}} . \tag{2.2}$$

Mass densities, calculated for unsulfonated copolymers, are included in Table 2.1. Note that M_{pvdf} is based on components x, y and z given in Table 2.1 and the monomer masses. When a graft sample becomes sulfonated its mass density changes depending on the PS ratio of the unsulfonated sample and the degree to which the sample is sulfonated. In order to find the mass density of the sulfonated samples, we should notice that the total mass of the sample increases upon sulfonation. Assume that the mass of an unsulfonated graft M_{unsulf} is given by

$$M_{\mathrm{unsulf}} = M_{\mathrm{pvdf}} + M_{\mathrm{ps}} = M_{\mathrm{ps}}(\alpha_{\mathrm{m}}+1) \ . \tag{2.3}$$

Now if this sample obtains a degree of sulfonation of DS, its mass would be

$$\begin{aligned} M_{\mathrm{sulf}} &= M_{\mathrm{pvdf}} + (1-DS)M_{\mathrm{ps}} + rDSM_{\mathrm{ps}} \\ &= M_{\mathrm{ps}}(\alpha_{\mathrm{m}}+1+DS(r-1)) \ , \end{aligned} \tag{2.4}$$

where r is the ratio by which the mass of PS increases upon sulfonation and is equal to the ratio of molar masses of sPS and PS or $r = \frac{M_{C_8H_8SO_3}}{M_{C_8H_8}} = \frac{184}{104}$. Similarly, we can calculate the change in the volume upon sulfonation. For unsolfonated grafts we have

$$V_{\mathrm{unsulf}} = V_{\mathrm{pvdf}} + V_{\mathrm{ps}} = M_{\mathrm{ps}}\left(\frac{\alpha_{\mathrm{m}}}{\rho_{\mathrm{pvdf}}} + \frac{1}{\rho_{\mathrm{ps}}}\right) , \tag{2.5}$$

while for the partially sulfonated cases there are three contributions

$$\begin{aligned} V_{\mathrm{sulf}} &= \frac{M_{\mathrm{pvdf}}}{\rho_{\mathrm{pvdf}}} + \frac{(1-DS)M_{\mathrm{ps}}}{\rho_{\mathrm{ps}}} + \frac{r \times DS \times M_{\mathrm{ps}}}{\rho_{\mathrm{sps}}} \\ &= M_{\mathrm{ps}}\left(\frac{\alpha_{\mathrm{m}}}{\rho_{\mathrm{pvdf}}} + \frac{(1-DS)}{\rho_{\mathrm{ps}}} + \frac{rDS}{\rho_{\mathrm{sps}}}\right) . \end{aligned} \tag{2.6}$$

Using these relationships, we can easily find different volume ratios, such as the volume ratio of sulfonated to unsulfonated PS

$$\frac{V_{\mathrm{sulf\ ps}}}{V_{\mathrm{unsulf\ ps}}} = \frac{\frac{rDS}{\rho_{\mathrm{sps}}}}{\frac{(1-DS)}{\rho_{\mathrm{ps}}}} . \tag{2.7}$$

And finally, mass density of the sulfonated samples can be calculated by dividing its mass Eq. 2.4 by its volume Eq. 2.6

$$\rho_{\mathrm{sulf}} = \frac{M_{\mathrm{sulf}}}{V_{\mathrm{sulf}}} = \frac{(\alpha_{\mathrm{m}} + 1 + DS(r-1))}{(\frac{\alpha_{\mathrm{m}}}{\rho_{\mathrm{pvdf}}} + \frac{(1-DS)}{\rho_{\mathrm{ps}}} + \frac{rDS}{\rho_{\mathrm{sps}}})} . \tag{2.8}$$

Clearly, the density of partially sulfonated samples depends on the degree of sulfonation DS. Based on these equations we can calculate the mass and volume increase upon sulfonation.

2.3.2 Ion exchange capacity (IEC)

The ion exchange capacity is one of the most important quantities in PEMs. It expresses the charge content of the materials and is defined as millimols (mmol) of ions per gram of material. This quantity provides a good framework for comparing different PEM materials. The IEC can be calculated based on the chemical structure or be measured experimentally [5]. For the studied graft system, the expected IEC value based on chemical structure is given by

$$IEC = \frac{nzDS}{x(M_{C_2F_2H_2}) + y(M_{C_2F_3Cl}) + z(M_{C_2F_3}) + nz(M_{C_8H_8}) + nzDS(M_{SO_3H})]} . \tag{2.9}$$

According to this equation one can conclude that not only the degree of sulfonation but also the PS ratio have significant roles in the IEC value. In order to illustrate the significance of the PS ratio in the studied samples, we plot the expected IEC values as a function of DS for the given PS ratios. As shown in Fig. 2.7, the calculated IEC values of all the samples are similar at lower DS values. By increasing DS, the IEC values increase but samples with higher PS ratio obtain higher IEC values for a given DS. This means that to obtain a given IEC value, samples with higher PS ratio need to be sulfonated at much lower degrees compared to the samples with lower PS ratios. For example, for IEC=2 mmol/g, the DS varies from 30% up to 50%, as illustrated by the horizontal dashed line in Fig. 2.7.

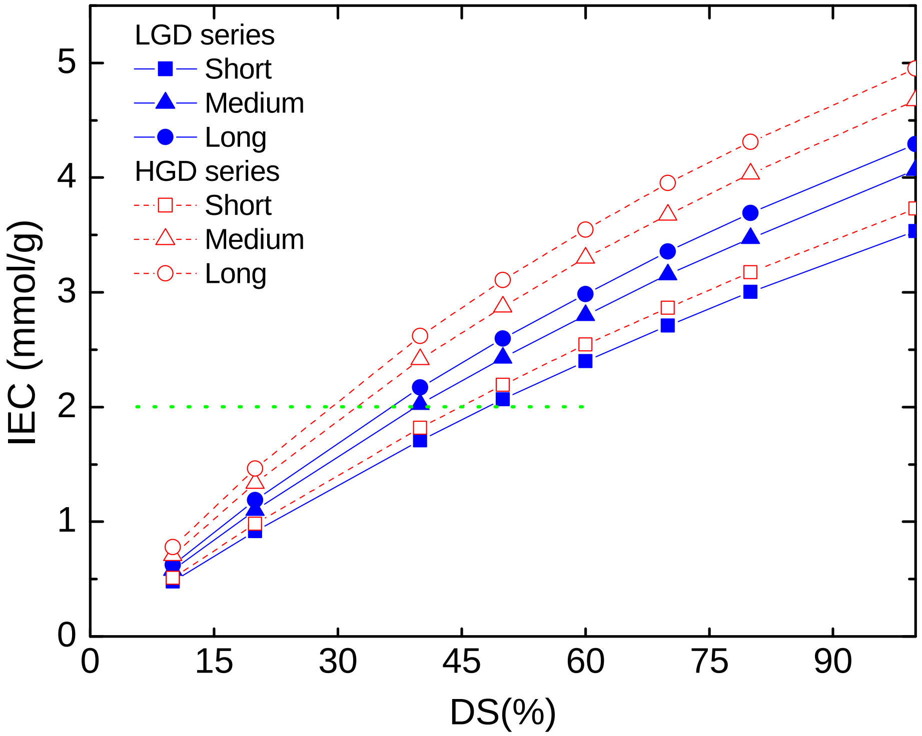

Figure 2.7: Expected IEC values plotted as a function of DS. To obtain a given IEC value samples with lower PS have to be sulfonated to higher degrees. The horizontal dashed line indicates that to obtains the IEC value of 2 mmol/g, the DS varies form 30% up to 50% for samples with the highest and lowest PS rations, respectively.

The IEC values presented in the thesis work were measured experimentally based on the titration method. The protonated membrane was immersed in NaCl (2 M) solution for 4 hours and titrated with a standardized solution of sodium hydroxide NaOH to the phenolphthalein end-point. After titration the membrane was reprotonated in 2M HCl and then dried in a vacuum oven at $\sim 80°\mathrm{C}$ to measure the weight of the dry membrane. The IEC value was calculated as

$$IEC(\text{mmol } SO_3H/\text{g}) = \frac{V_{\text{NaOH}} \times C_{\text{NaOH}}}{M_{dry}} \ , \tag{2.10}$$

where M_{dry} is the mass of the dry membrane, and V_{NaOH} and C_{NaOH} are the volume and concentration of solution, respectively.

It is useful to define volume-based ion content values

$$IEC_{\text{v}} = \rho \times IEC \ , \tag{2.11}$$

in which IEC_{v} is the volume-based IEC and ρ is the mass density of the dry samples. This quantity is useful in morphological studies. We will refer to it in when comparing the morphological aspects of different samples.

2.3.3 Water uptake and water content

Water plays a crucial role in the proton conductivity of PEMs. There are two approaches to investigate structure-morphology-property relationships of PEMs regarding hydration: one is to study water-saturated samples and the other is to examine the properties of the membranes under controlled humidity [36]. In the former approach the membrane is soaked in deionized water, usually overnight and a fully hydrated sample is obtained, while in the second method the membrane is not exposed to water directly. Only data corresponding to the first approach was considered in this work.

Mass-based water uptakes and water contents are defined as

$$\text{Water uptake} = \frac{M_{wet} - M_{dry}}{M_{dry}} \ , \tag{2.12}$$

$$\text{Water content} = \frac{M_{wet} - M_{dry}}{M_{wet}} \ , \tag{2.13}$$

where M_{dry} is the weight of the membrane measured after drying in an oven at 80°C overnight and M_{wet} is the weight measured after soaking the membrane in water overnight. Before measuring the weight of the fully hydrated samples, the surface water was removed by slightly dabbing the membrane using a tissue. The other relevant quantity is the volume-based water content X_v, which is defined as

$$X_\mathrm{v} = \frac{V_{wet} - V_{dry}}{V_{wet}} \ , \tag{2.14}$$

in which V_{wet} and V_{dry} are the volume of the fully hydrated and dry membrane, respectively. This quantity was obtained by measuring the thickness and area of dry and hydrated samples directly. It also can be calculated based on mass-based water content and mass density of the polymer. Results obtained based on these two approaches are consistent.

In Chapter 6, we will discuss the volume ratios of the hydrated samples. Therefore, we need to calculate how volume ratios change upon hydration. The volume of the hydrated sample V_{hyd} can be written as

$$V_{hyd} = M_\mathrm{ps}\left(\frac{\alpha_\mathrm{m}}{\rho_\mathrm{pvdf}} + \frac{(1-DS)}{\rho_\mathrm{ps}} + \frac{rDS}{\rho_\mathrm{sps}}\right) + V_{water} \ . \tag{2.15}$$

where V_{water} is the volume of water and incorporates the water's contribution in Eq. 2.6. Consequently, water content is given by

$$X_\mathrm{v} = \frac{V_{water}}{M_\mathrm{ps}\left(\frac{\alpha_\mathrm{m}}{\rho_\mathrm{pvdf}} + \frac{(1-DS)}{\rho_\mathrm{ps}} + \frac{rDS}{\rho_\mathrm{sps}}\right) + V_{water}} \ , \tag{2.16}$$

and hence

$$V_{water} = M_\mathrm{ps}\left(\frac{\alpha_\mathrm{m}}{\rho_\mathrm{pvdf}} + \frac{(1-DS)}{\rho_\mathrm{ps}} + \frac{rDS}{\rho_\mathrm{sps}}\right)\frac{X_\mathrm{v}}{1-X_\mathrm{v}} \ . \tag{2.17}$$

and therefore, ratios of volume corresponding to water, PS and sPS are given by,

$$V_{water} : V_\mathrm{ps} : V_\mathrm{sps} = \left(\frac{\alpha_\mathrm{m}}{\rho_\mathrm{pvdf}} + \frac{(1-DS)}{\rho_\mathrm{ps}} + \frac{rDS}{\rho_\mathrm{sps}}\right)\frac{X_\mathrm{v}}{1-X_\mathrm{v}} : \frac{(1-DS)}{\rho_\mathrm{ps}} : \frac{rDS}{\rho_\mathrm{sps}} \ . \tag{2.18}$$

Two other useful parameters are the volume-based ion content of hydrated samples IEC_wet and the ion content based on volume of the water IEC_water

$$IEC_\mathrm{wet} = \frac{\text{mmol acid groups}}{V_{wet}} = IEC_\mathrm{v}(1-X_\mathrm{v}), \tag{2.19}$$

Table 2.2: Definition of different IEC values.

IEC (mmol/g)	mass-based IEC of the dry sample
IEC_{v} (mmol/cm^3)	volume-based IEC of the dry sample
IEC_{wet} (mmol/cm^3)	volume-based IEC of the hydrated sample
IEC_{water} (mmol/cm^3)	volume-based IEC of the water

and

$$IEC_{\mathrm{water}} = \frac{\text{mmol acid groups}}{V_{water}} = \frac{IEC_{\mathrm{wet}}}{X_{\mathrm{v}}} = IEC_{\mathrm{v}}\frac{(1 - X_{\mathrm{v}})}{X_{\mathrm{v}}}. \tag{2.20}$$

We will use these parameters in Chapter 6. Table 2.2 summarizes the different IEC values that have been introduced in this chapter.

2.3.4 Water content properties

Figures 2.8 (a) and (b) show the water content properties as a function of IEC of samples in the HGD and LGD series, respectively. The general trend is that water content increases with IEC. Water content of samples with long and medium side chains have a concave trend, while samples with short side chains in both series have a concave trend for lower IEC values followed by a convex trend at medium IEC values. Samples with short side chains of the LGD series exhibit another concave trend at IEC values larger that ~ 2.7 mmol/g. In our previous work based on TEM results [1], we suggested that samples of the HGD series with the shortest side chains have a lower percolation threshold than HGD samples with long and medium chains.

2.3.5 Conductivity

Through-plane proton conductivity was measured using AC impedance spectroscopy. Data was collected using a Solartron 1260 frequency response analyser. This was done by sandwiching the membrane between two platinum electrodes. The data was collected using an AC voltage of 10 mV with frequency varying from 10 MHz-100 Hz. The resulting Nyquist plots were analysed to obtain the membrane resistance R_m. Details of this analysis are explained elsewhere [37]. The membrane conductivity σ is calculated

$$\sigma = \frac{L_m}{R_m A}\ , \tag{2.21}$$

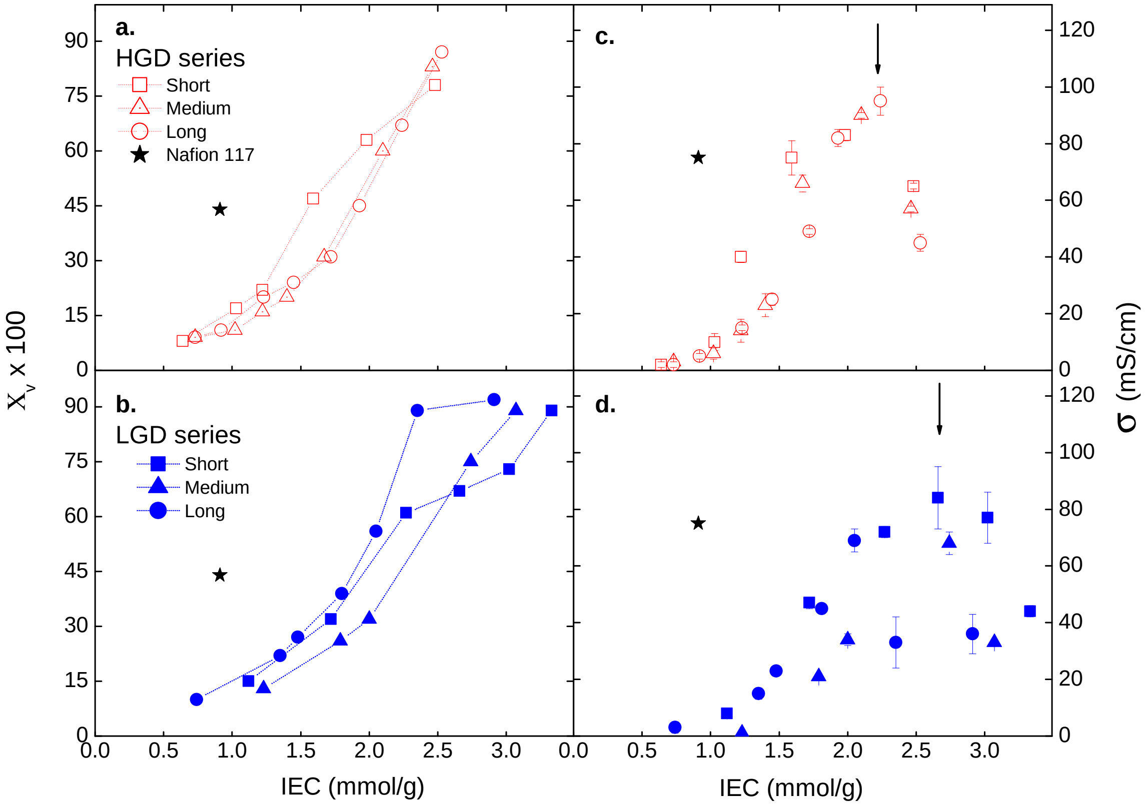

Figure 2.8: Water content (a, b) and conductivity (c, d) of ionic graft copolymers, (a) and (c) correspond to samples of the HGD series with short (□), medium (△) and long (○) side chains, and (b, d) correspond to samples of the LGD with short (■), medium (▲) and long (●) side chains. The arrows in (c) and (d) indicate the position of the maximum conductivity. Data provided by Dr. Tsang and Ms. Yang [1, 22].

in which L_m and A are the membrane thickness and area, respectively. Figure 2.8 (c) and (d) show the conductivity of samples of the HGD and LGD series, respectively, as a function of IEC. The general behaviour in each set of samples is similar, with minor differences. All samples show an increase of conductivity with IEC followed by a fall-off at high IEC values, so that all of them have a maximum conductivity. However, the position of the maximum is shifted to higher IEC values for samples of LGD series. These differences have been associated with the differences in the details of the chemical structure [1, 22]. We will address these properties in the Chapter 6.

2.3.6 TEM images

In the initial work, the morphology of the membranes was studied by TEM [1, 22]. The samples were stained with lead acetate for TEM measurements. Since the electron density of lead is quite high compared to that of the polymer, domains containing lead scatter electrons more and look darker in the TEM image. We also know that the lead acetate can only penetrate the water domains during staining. The result is that the hydrophilic domains or ionic clusters will be the dark areas in the TEM image, while bright areas are the hydrophobic domains.

Sample preparation for TEM was as follows: membranes were soaked in saturated lead acetate solution overnight, then rinsed with water and dried in an oven as explained before. Spurr's epoxy resin was used to support the specimen, before cutting the samples into ~ 70 nm thick slices. Slicing was performed on a Leica UC6 ultramicrotome, using a diamond knife. TEM images were acquired on a Hitachi H7600 TEM. Data was collected at an accelerating voltage of 100 kV.

Figures 2.9 and 2.10 show the typical TEM images for samples in the LGD and HGD series, respectively. All the images show a random morphology. In Fig. 2.9 all the samples with higher IEC values (Fig. 2.9 right hand side) are fully sulfonated, while the other samples (Fig. 2.9 the left hand side) have a degree of sulfonation around 20%. In the case of fully sulfonated samples, the bright areas represent the fluorous-rich domains. These images strongly indicate that the fluorous component of the system forms random quasi-spherical domains. In the case of partially sulfonated samples, the bright areas represent both unsulfonated PS and fluorous-rich domains. All the TEM images available for the HGD series (Fig. 2.10) belong to partially sulfonated samples. The sulfonation degree and IEC values corresponding to these samples are included in Tables 2.3. Image analysis indicates

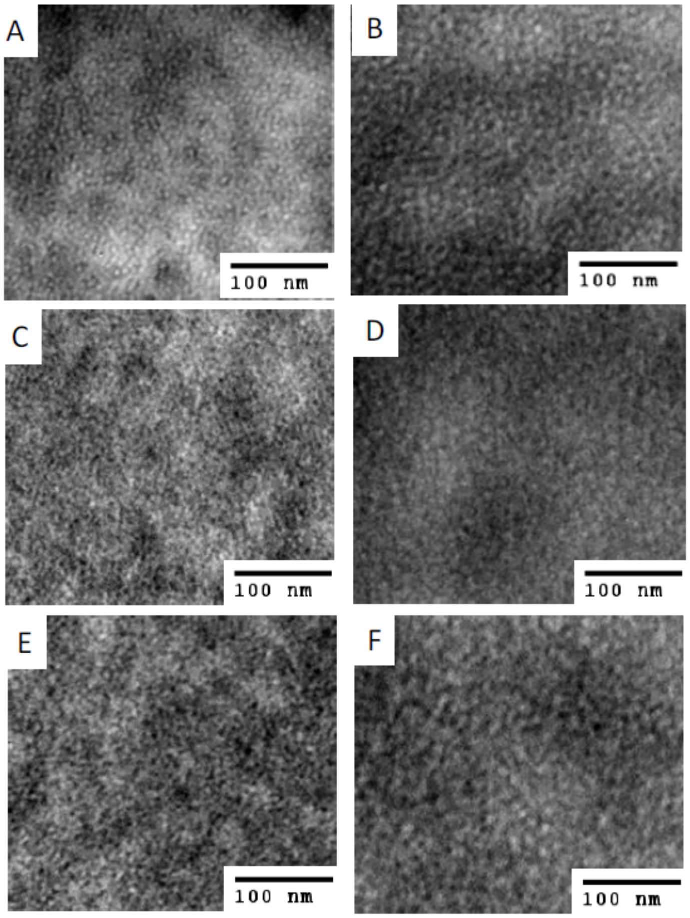

Figure 2.9: TEM images of stained samples of LGD series with short side chain (top row) A) IEC=1.12 mmol/g and B) IEC=3.52 mmol/g , medium side chains (middle row) C) IEC=1.23 mmol/g and D) IEC=4.05 mmol/g, and long side chains (bottom row) E) IEC=1.35 mmol/g and F) IEC=4.29 mmol/g. The samples with higher IEC values are all fully sulfonated. Bright area in these images are the fluorous-rich domains. Images are provided by Ms. Yang.

Table 2.3: Size and number density of the ion-rich domains as obtained based on TEM images. Data corresponds to samples of the HGD series and were provided by Emily M. W. Tsang [1].

n	(IEC)	DS (%)	ionic cluster width (nm)	2-D no. density (nm^{-2}) $\times 10^3$
Short	0.64	13	2.2 ± 0.4	21 ± 2
Short	2.48	59	3.3 ± 0.4	19 ± 2
Medium	0.73	10	1.9 ± 0.3	26 ± 3
Medium	2.46	41	2.6 ± 0.4	28 ± 2
Long	0.73	9	1.8 ± 0.3	25 ± 3
Long	2.53	33	2.1 ± 0.3	35 ± 3

that, generally, the size of the ionic clusters increases with increasing IEC values, however, these results indicate that samples with shorter side chains obtain bigger domain sizes and that their cluster number density (2-D no. density) shows a smaller variation (Table 2.3). The image analysis was done manually, by measuring the size and number density of the dark areas of the image using ImageJ software version 1.41. Figure 2.11 schematically illustrates how the size and number density of the ion-rich domains change as IEC value increases. According to this analysis, a model consisting of ionic aggregates surrounded by unsulfonated PS embedded in a continuous phase of fluorous matrix was proposed, as shown in Fig. 2.12.

Tsang *et al.* [1] suggested that the level of sulfonation and the proximity of the acid groups along the side chain play an important role in determining the size of the ion clusters. In fact, for a given IEC value, samples with short side chains have a higher degree of sulfonation compared to the samples with medium and long side chains, as shown in Fig. 2.7. Consequently, at low IEC values, the formation of the larger ion-rich domains in series with short side chains lead to higher water content values. On the other hand, a relatively low degree of sulfonation for samples with longer side chains is equivalent to more hydrophobic PS domains. Therefore, at low IEC values, the ion-rich domains are surrounded by PS shells. These PS shells hinder the connectivity of the ion-rich domains and, hence, lead to lower conductivity. Thus, samples with longer side chains have lower conductivity at $IEC = 1.2$ mmol/gr, beyond this point all the samples reach the percolation threshold and have the same conductivity.

Generally, TEM techniques based on staining should be considered in light of the

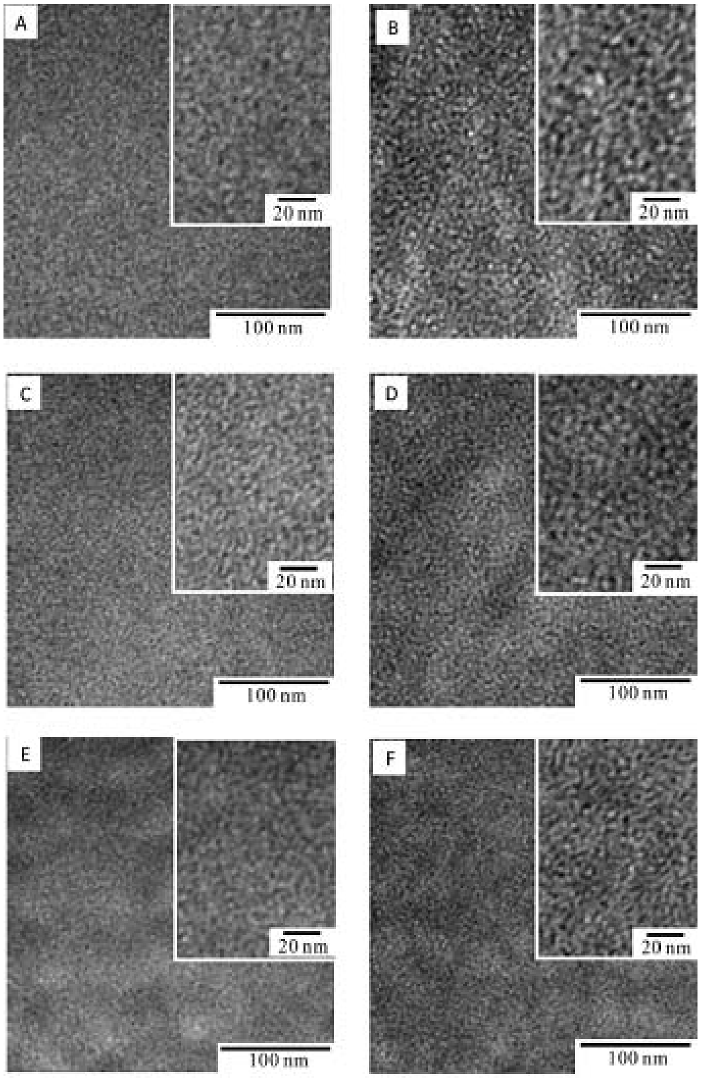

Figure 2.10: TEM images of stained samples of the HGD series with short side chain: short side chain (top row) (A) IEC=0.64 mmol/g, and (B) IEC=2.48 mmol/g , medium side chains (middle row) (C) IEC=0.73 mmol/g, and (D) IEC=2.46 mmol/g, and long side chains (bottom row) (E) IEC=0.73 mmol/g and (F) IEC=2.53 mmol/g. From [1], used with permission.

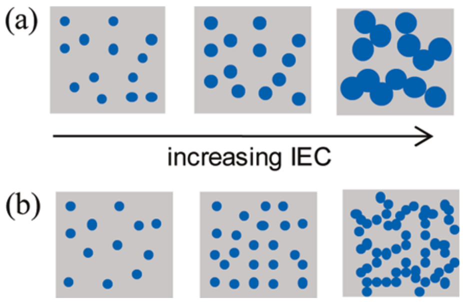

Figure 2.11: Schematic diagram of the morphology of ion-rich domains based on TEM. (a) For samples possessing short side chains, the size of the domains increases upon IEC but the number density of the domains stays the same. (b) For samples possessing long and medium side chains, the size of the domains stays the same as IEC values increase; but instead, number density increases.From [1], used with permission.

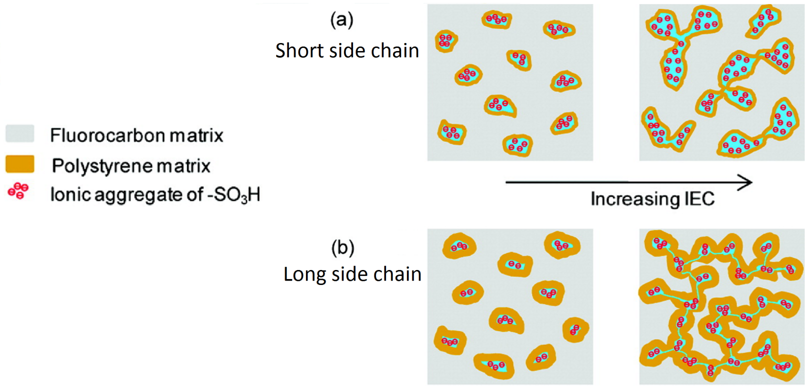

Figure 2.12: Schematic diagram of the overall morphology of the ionic graft membrane. According to this model ion-rich domains are surrounded by a PS shell and embedded in a fluorous continuous phase. Depending on the length of the side chains membranes obtain different domain size and number density. From [1], used with permission.

following: First, the acid groups are exchanged with heavier ions. This process might affect the morphology of the membrane. The other challenge is that the size of the ionic aggregates is much smaller than the thickness of the samples probed *i.e.* 2 nm versus 70 nm. This means that a dark area in the TEM images is not a representative of an individual ion cluster, but instead could represent a stack of several clusters. In practice, we believe that this technique is a rather subjective method and extra caution should be considered during measurement and data interpretation.

This thesis intends to reconcile the morphology of fluorous domains and show that the previously proposed model is not entirely correct. In fact, the volume ratio of PVDF is smaller than 35% vol for all of the samples, which is inconsistent with a fluorous continuous matrix. Instead we suggest that the morphology consists of fluorous domains embedded in a continuous phase of partially sulfonated PS. In order to examine whether this proposed morphology is consistent with TEM images, we did some preliminary simulations.

2.4 Matlab simulations and TEM images

In order to simulate the TEM images, we should consider that the microtome slice of the samples has a thickness of 60 to 100 nm. Therefore, we considered a matrix of $100 \times 100 \times 100$ pixels, each pixel representing 1 nm. Ten percent of the volume of the cube was filled by spheres with size of 4 to 6 nm, representing fluorous domains. The minimum spacing between spheres was set to be 16 nm and the spheres were randomly distributed in the cube volume. In the next step, the available void space in the cube volume was filled with spheres with radii between 2 to 4 nm, to result in 30% volume fraction, representing the ion-rich domains. The minimum spacing of these spheres was set to be 3 to 5 nm. We also take into account that spheres of different type have a minimum spacing of 12 nm. The reason to chose a minimum spacing larger than the sum of the radii is to account for a PS shell around each domain. The rationale behind these numbers, and the thickness of the PS shell, will be discussed extensively in this thesis. At this stage we want to show that the model is consistent with the TEM images.

Figure 2.13 (a) and (b) show the 3-D morphologies of fluorous and ion-rich domains created in Matlab and Fig. 2.13 (c) and (d) show their corresponding 2-D projections, respectively. The rest of the cube volume is the continuous unsulfonated PS matrix. The 2-D projection of a 3-D morphology is how TEM reveals information about the morphology of

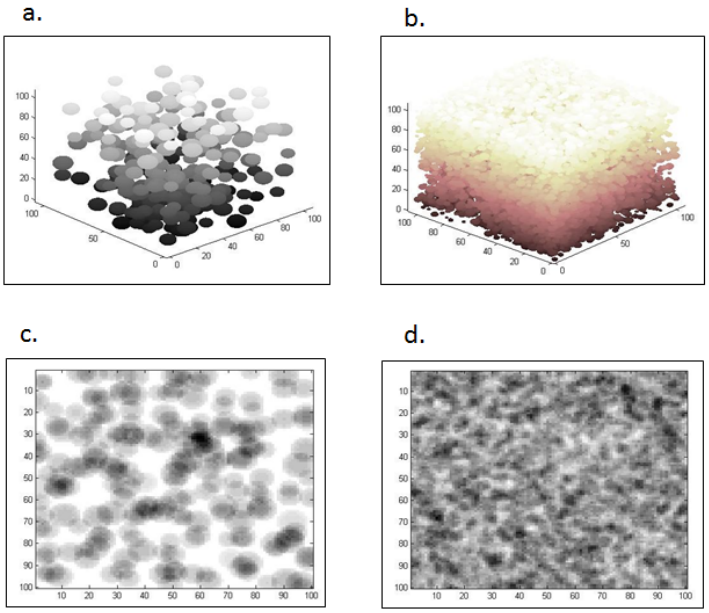

Figure 2.13: Matlab simulation of the proposed morphology. Figure (a) and (b) show the 3-D morphologies of fluorous and ion-rich domains and (c) and (d) show their corresponding 2-D projections. A 2-D projection of the ion-rich domains is what we can see in TEM images. These results are in good agreement with the TEM images.

these membranes. Moreover, in the TEM images, the fluorous domains are indistinguishable from the unsulfonated matrix. In fact, not realizing this, was what misled us when proposing the model based on TEM images. However, as shown in Fig. 2.13 (d), the spherical ion-rich domain morphology is in a good agreement with TEM images. We will show how SAXS and SANS can be used to clarify the details of this morphology.

2.5 Summary and motivation

Two series of graft copolymers with controlled architectures have been designed and synthesized in order to investigate structure-morphology-property relationships of polymers for PEMFCs. Properties such as water uptake and conductivity were studied and a model based on TEM images was presented to explain observed trends. In this thesis, our focus is to examine the details of the morphology at a deeper level, in particular the size and spacing of the fluorous and the water-rich domains in this system.

In a similar study, two series of P[VDF-*co*-CTEF]-g-sPS membranes were studied by Zhang *et al.* [38] in order to investigate the effect of the molecular weight of the backbone and graft number density on the bulk properties of their membranes. They investigated the morphology of the membrane using the TEM imaging techniques only. The molecular weight of the backbones in this study were 312000 and $15000 - 20000$ g/mol. For the high molecular series, five different graft number densities were considered, namely 0.3, 0.8, 1.4, 1.7 and 2.4 mol %, possessing graft lengths of 120, 37, 21, 17 and 14 repeating units per side chain, respectively. For any given unsulfonated sample, only two sulfonated samples with different degrees of sulfonation were examined. For the low molecular weight series, samples with 4 different graft number densities; 0.4, 0.8, 1.4 and 1.8 mol % were studied. In order to obtain the desired IEC range, both length and degree of sulfonation of the graft were varied. With this system, they were not able to study the effect of the length of the side chain on the size of ionic aggregates, for example. In this study, we have considered three different lengths of side chains for any given graft number density and then obtained different IEC ranges for each length of the side chain by changing one parameter: the degree of sulfonation. In summary, our approach provided an excellent frame-work to distinguish the effect of side chains and graft number density on different properties of this material. Furthermore, one of the factors that significantly differentiates our work from similar studies is that we studied P[VDF-*co*-CTEF]-g-sPS systems in which the ratio of partially sulfonated polystyrene is larger than 50 weight%.

Chapter 3

Experimental techniques

3.1 Introduction

Over several years, different scattering techniques, such as X-ray and neutron scattering, have been developed to study the structure of matter at sub-micron levels. In scattering techniques, a beam of photons or particles is scattered from the materials of interest in order to examine the structure of the materials. The experimental results are then used to confirm or to reject models based on a theoretical framework. In contrast to the microscopy techniques in which the experimental results consist of a magnified image, the results of scattering techniques contain information about the structure of the material expressed in reciprocal or Fourier space [39, 40, 41].

One of the most famous scattering experiments is that of Ernest Rutherford. By investigating the scattering of the alpha particles from a thin gold film, Rutherford determined the proper model for the distribution of positive and negative charges in the atom. At that time it was well known that matter consisted of discrete negatively charged electrons, however, it was assumed that the positive charges were distributed homogeneously (pudding) through out the material which balanced the electric charge of the electron (plums). Rutherford noticed that most of the alpha particles easily went through the gold film and only one or two percent of them were deflected. Consequently, he discarded the plum-pudding model and suggested that most of the mass of matter is concentrated in a small volume fraction that is positively charged [42]. Generally, this concept can be used to study a wide range of length scales, from micron size particles to fundamental particles such as the Higgs boson, by adjusting the energy of the probe beam. The higher the energy of the beam; the smaller the length scales probed. The theory by which the scattering results are interpreted differs from experiment to experiment and depends on factors such as the energy scale, the type of the interaction between the scatterer and the probe beam and even the relative ratio of the size of the scatterer and wave length of the beam [39, 40, 41].

In polymer science, scattering techniques are used to examine the polymeric system at two different length scales; one is the order between atoms and deals with length scales of the order of an angstrom, the other aspect is the existence of the meso-scale domains and focuses on length scales from a few nanometers to hundreds of nanometers. The former method examines whether the polymer is crystalline, and if so what kind of crystal structure it has and to what degree it is crystalline. The second method studies the phase separation in the system and is especially used for copolymer systems in which different segments of the copolymer have the ability to phase separate into different morphologies.

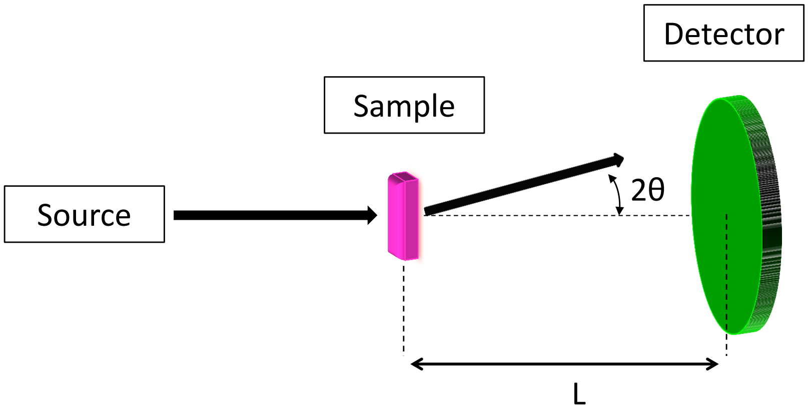

Figure 3.1: Schematic of the scattering set up in transmision mode.

Both techniques were used in this thesis. The principles of the experimental setup used for both methods are similar and illustrated in Fig. 3.1. The incident beam goes through the sample and then the scattered beams are detected at different scattering angles 2θ by a detector located at a distance L from the sample, where the scattering angle 2θ is the angle between incident and scattered beams. This transmission mode setup is employed for polymeric systems because polymers in particular and soft materials in general scatter and absorb fewer X-rays or neutrons compared to other materials with higher densities.

Scattering patterns are displayed in terms of intensity as a function of angle θ. In this case the position of the scattering features, *i.e.* characteristic peak positions, depends on the wavelength of the incident beam. Alternatively, the scattered intensities can be depicted as a function of scattering wave vector q, where

$$q = \frac{4\pi}{\lambda} \sin(\theta) \ , \tag{3.1}$$

in which λ is the wavelength of the probing beam. The scattering vector is defined as $\vec{q}=\vec{k_f} - \vec{k_i}$ in which $\vec{k_i}$ and $\vec{k_f}$ are the initial and final beam wave vectors. One should consider that in these kinds of morphological studies, we only consider elastic scattering, in which no energy is transferred to the target, and the wavelength of the beam before and after the scattering is the same. Since $\vec{k_i}$ and $\vec{k_f}$ have the same magnitudes and the angle between them is 2θ one can calculate q. One advantage of plotting scattering data in q-space is that we can easily compare the scattering patterns from different instruments with different wavelengths as in q-space the position of the characteristic features do not depend on the wavelength. In this representation every characteristic feature of the scattering pattern corresponding to a given q value can be associated with a length scale $d = \frac{2\pi}{q}$. Substituting q in Equation 3.1 yields $2d\sin(\theta) = \lambda$, which is Bragg's condition. The d values are inversely proportional to q values, which implies that for a given wavelength the characteristic features of the larger scale appear at lower q values, which is equivalent to smaller scattering angles. In fact, scattering techniques in soft materials are classified based on the length scales probed and named by the range of scattering angle that they investigate.

This chapter overviews the experimental techniques that we used to study the morphology of the membranes: wide and small angle X-ray scattering (WAXS and SAXS), and small angle neutron scattering (SANS).

3.2 X-ray scattering techniques

X-rays interact with the electron cloud surrounding the nucleus of atoms. The scattered X-rays interfere on their way to the detector and create diffraction patterns that depend on the variation of the electron density from point to point in the sample. When atoms in the material lie on a lattice, each interplanar d-spacing can result in a peak in the diffraction pattern at a scattering angle θ which obeys Bragg's law: $n\lambda = 2d\sin(\theta)$, where λ is the wavelength of the X-ray and typically is of the order of 0.1 nm. For d 0.57 nm the typical scattering angle would be smaller than 5°. Based on this fact, X-ray scattering techniques are classified into two main areas, small and wide angle X-ray, corresponding to different length scales on the order of nano-meter and subnano-meter, respectively [43, 44].

3.2.1 Instrumentation

Wide angle X-ray scattering

Wide-angle diffraction measurements were performed on two different diffractometers, both utilizing a copper source (X-ray wavelength, $\lambda = 0.154$ nm): a Rigaku Rapid Access XRD with a a fixed image plate detector, and a Siemens D5000 with a point detector. In both instruments, data was acquired in transmission mode under ambient conditions. The Rigaku instrument was operated at 46 kV and 42 mA. A pinhole with a radius of 0.8 mm at a distance of 2 cm from the sample was used to collimate the beam. Data acquisition times of 2 minute were typically sufficient to achieve adequate signal to noise ratios. The Siemens D5000 was run at 50 kV and 30 mA. The instrument was equipped with one slit in front of the source and another one in front of the detector. Slit sizes of 0.1 mm were chosen to collect data. Since this instrument has a point detector, each run was made overnight

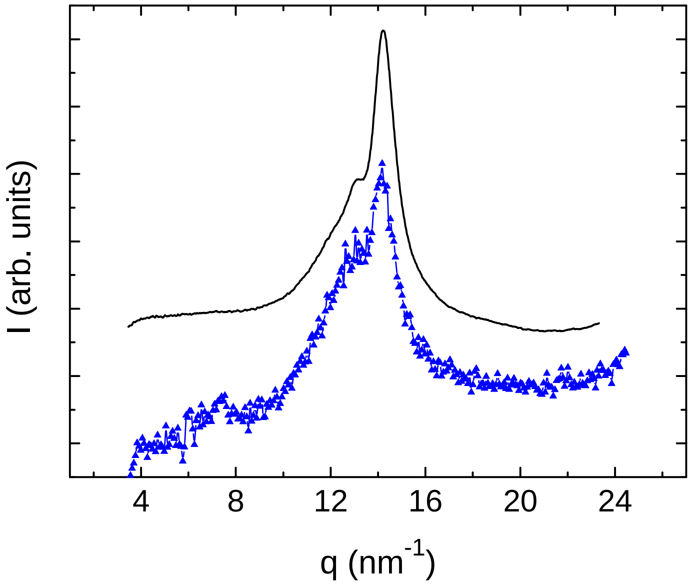

Figure 3.2: Intensity of scattered X-rays as a function of the scattering wave vector for the macroinitiator possessing 5.6% CTFE comparing a 2 minute run at Rigaku Rapid Axis (—) and a 10 hour run at Siemens D5000 (▲).

to obtain a reasonable signal to noise ratio and 3 to 6 layers of the sample were stacked to obtain a sufficient intensity scattering for X-ray measurements. Figure 3.2 compares the wide angle X-ray intensities of the same sample obtained by each instrument, where the data for the lower curve was taken with the Siemens D5000. Clearly, the main features are similar, except for the fact that the Siemens D5000 produces a noisier spectrum. Most of the WAXS measurements in this thesis were performed on the Rigaku instrument.

The majority of the X-ray data presented in this thesis was obtained from dry samples. Each sample was kept at 60° C in the oven overnight in order to dehydrate the samples before measurements were taken.

Small angle X-ray scattering

Small angle X-ray scattering measurements were obtained with two instruments: a Bruker Nanostar SAXS instrument located at NINT in Edmonton, Alberta and a Rigaku S-MAX located at the Adolphe-Merkle Institute in Fribourg, Switzerland. In both cases, the X-ray source was a copper rotating anode operating at 45 keV and 110 mA. Coupled Gobel mirrors were used to focus the divergent beam and to select a Cu K_α radiation wavelength of 0.154 nm. In order to decrease the scattering due to air molecules, the volume between the source and detector, including the sample holder, is maintained at low pressure (2×10^{-2} bar). Data was acquired in transmission mode. An Ag-Behenate sample was used as the standard for calibration and each data set is corrected for incoherent scattering background by subtracting the empty beam. The 2-D scattering intensities were isotropic, hence, the data was analysed in terms of the azimuthal average. We obtained SAXS measurements on five different spots on each sample to check sample uniformity. For further analysis we used the average of the five different runs. As shown in Fig. 3.3, data acquired for the same sample using these two instruments is consistent.

3.3 Neutron scattering techniques

Neutrons are massive particles with no charge and they interact with the nuclei through nuclear forces. For a single nucleus, this interaction depends on the spin state of the interacting neutrons and nucleus. For such a simple case, scattering is expressed in terms of a scattering length b, which depends on how strong the neutron scatters from a given

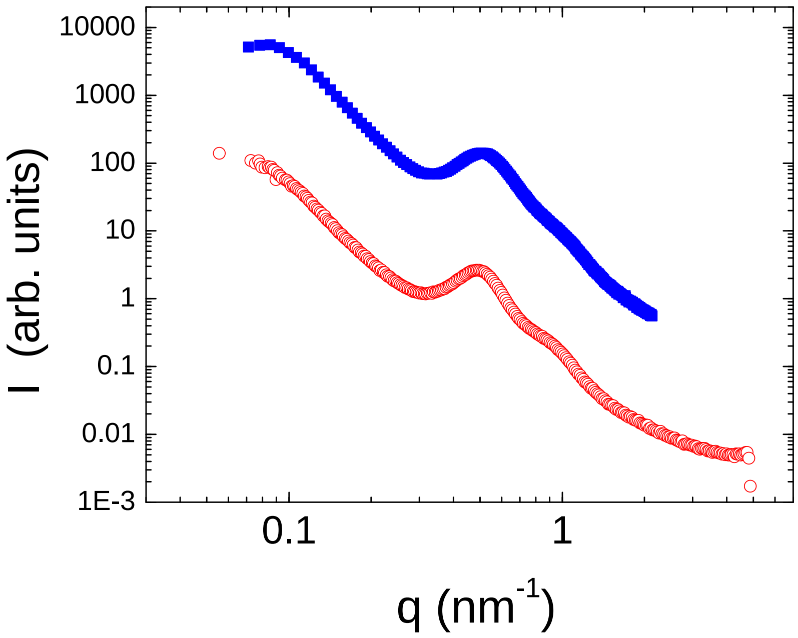

Figure 3.3: SAXS data obtained by Bruker Nanostar (■) and Rigaku S-MAX SAXS (○) instruments. Data corresponds to the unsulfonated sample of HGD series with medium side chain. Data is displaced in y-direction for clarity.

nucleus. The scattering length is defined as [41]

$$b^2 = \frac{d\sigma}{d\Omega} \ , \tag{3.2}$$

where $\frac{d\sigma}{d\Omega}$ is the differential scattering cross section of the nucleus. For an assembly of spin-zero nuclei of the same isotope, the value of b is identical. However, if the nuclei are not spin-less, there will be two values for b. These values arise from the fact that neutrons have two spin states: $\frac{1}{2}$ and $-\frac{1}{2}$. Considering this, one can calculate the coherent scattering length

$$b_{coh} = < b > \ , \tag{3.3}$$

in which $<>$ indicates the expectation value of b with regard to different possible spin states. When the material is composed of different elements with different isotopes, the scattering length density SLD is defined as the sum of the scattering lengths b_α weighted by the spatial distribution of the nucleic centres n_α

$$\mathrm{SLD} = \Sigma_\alpha b_\alpha n_\alpha \ . \tag{3.4}$$

For a molecule possessing N_m atoms and a total volume of V_m, we can rewrite the above equation as

$$SLD = \frac{\Sigma_{i=1}^{N_m} b_i}{V_m} \ , \tag{3.5}$$

Given the chemical structure and the mass density, one can calculate SLD values for any molecule. To calculate SLD values for our samples, we used NIST online calculator [45].

The fact that neutrons interact only with nuclei makes neutron scattering a unique tool. It is possible to vary the SLD of given molecules without changing the chemical structure of the molecules by incorporating different isotopes. For example the SLD values of H_2O and D_2O are -0.56×10^{-4} and $6.22 \times 10^{-4}\mathrm{nm}^{-2}$, respectively. This method is called contrast matching. By utilizing this technique, one can distinguish between different phases in the sample. Figure 3.4 illustrates how this technique can be utilized to study a three phase system. Assume that two different phases (blue and black domains) exist in a continuous phase, as shown in Fig. 3.4 (a) on the left side. Presumably, the SANS intensities reveal two characteristic features corresponding to different spherical domains embedded in the continuous phase (Fig. 3.4 (a) right side). Assume it is possible to change the contrast of the blue domains. As shown in Fig. 3.4 (b) left side, by matching the SLD value of this phase to the continuous phase, this phase becomes invisible and hence its characteristic peak disappears. Furthermore, if the SLD values of the blue domains is matched to that of black domains, they will be visible to the neutrons but indistinguishable from the other domains. This means that the peak corresponding to these domains reappears in the SANS intensity, but has a different amplitude compared to that of the first case.

In this thesis all the SANS measurements were acquired on hydrated samples. Four different mixtures of (D_2O:$\mathrm{H_2O}$), namely (100:0), (60:40), (30:70) and (0:100), were considered for the contrast matching experiment. Table 3.1 compares the SLD values of these solvents to that of different segments of the studied copolymers. Each sample was soaked in the solvent for at least 2 hours before running the SANS measurements. During data collection, fully hydrated samples were kept between two quartz windows in order to avoid evaporation.

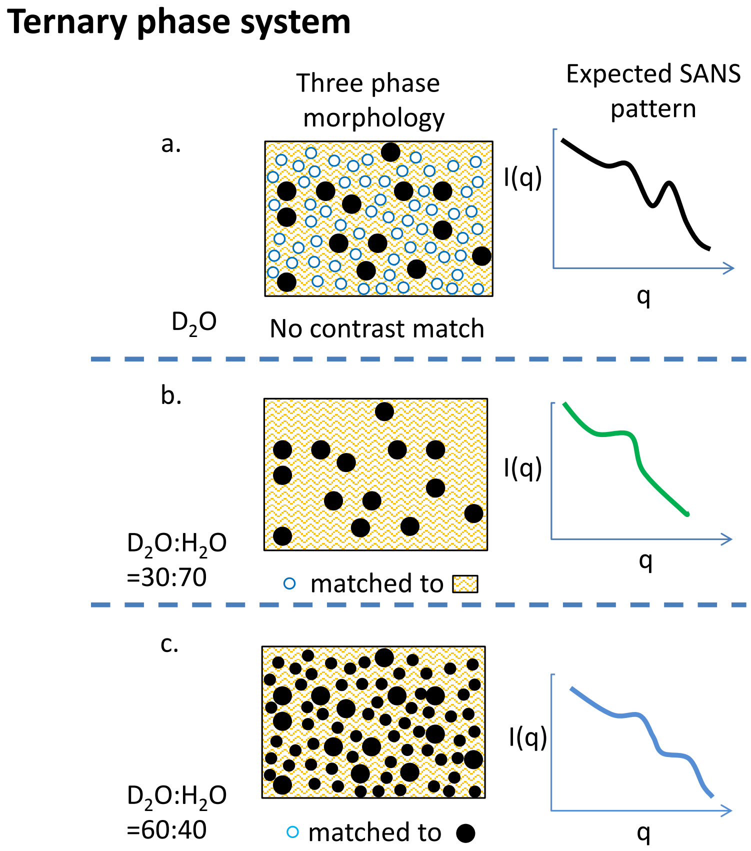

Figure 3.4: (a) A three phase system consisting of two phases of spheres possessing two different average sizes and distributions, big (•) and small (○), embedded in a third continuous phase. Presumably, these two different distributions produce two characteristic peaks in the SANS pattern, as shown on the right hand side. If we can match the SLD of the smaller spherical domains (○) to that of the continuous phase, we reduce the contrast between the two phases and thus the scattering. By matching the contrast of this phase with that of the continuous phase we expect the peak associated with this phase to disappear, as shown in (b). Finally, if we match the contrast of the phases that form spherical domains, as shown in (c), we would expect to see both of the peaks again. By designing such an experiment we can discriminate between a two phase and three phase system and also identify which phase, each scattering feature corresponds to.

3.3.1 Instrumentation

We used the D11 instrument located at Institut Laue-Langevin, Gronoble France. Figure 3.5 shows a schematic diagram of the experimental set up. The neutron beam goes through a velocity selector to obtain the desired wave length. Then it passes through the collimator and hits the sample. The scattered beam travels towards a detector which is kept in an evacuated tube.

For this thesis experiments were done in two runs. During the first run, the wave length of the beam was 0.8 nm and in the second run it was 0.6 nm.

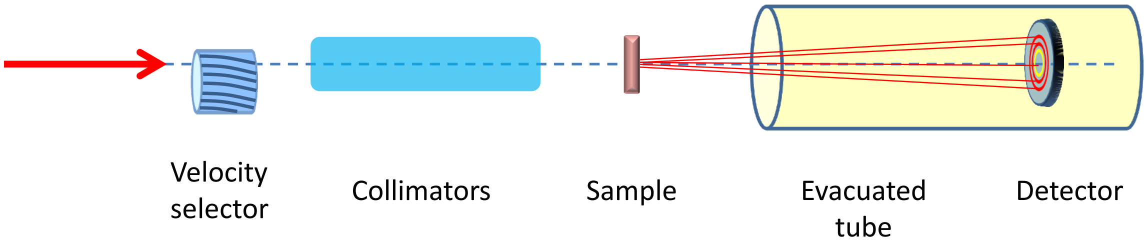

Figure 3.5: Schematic shows the SANS set up.

In each run the detector was positioned at three locations. In the first run d = 1.1, 5 and 28 m and in the second run d = 1.2, 5 and 20 m. The data corresponding to these distances correspond to large, medium and small q-ranges, respectively. An overall q range of 0.05 - 2.4 nm^{-1} and 0.03 - 5 nm^{-1} was investigated in the first and second run, respectively.

SANS data in the large q range were corrected for camera sensitivity based on scattering intensities of the solvents. Data were merged at large and medium q ranges at $q = 0.85\ \text{nm}^{-1}$, and medium and small q ranges at $q = 0.22\ \text{nm}^{-1}$. The incoherent scattering background was estimated by averaging the last 5 data points of the SANS intensity and was subtracted from each data set.

Table 3.1: SLD values of different solvents used in SANS measurements and SLD values corresponding to different segments of the graft copolymer. These values are obtained using the NIST online calculator: http://www.ncnr.nist.gov/resources/sldcalc.html.

Solvent ($D_2O : H_2O$)	$SLD \times 10^{-4}(\mathrm{nm}^{-2})$
100 : 0	6.22
60 : 40	3.59
30 : 70	1.52
0 : 100	-0.56
copolymer segment	$SLD \times 10^{-4}(\mathrm{nm}^{-2})$
$PVDF$	2.9
PS	1.41
sPS	2.06

Chapter 4

Crystallinity

4.1 Introduction

The arrangement of atoms in an ordered manner at an atomic level is known as crystallinity. However, in a polymer the tendency of atoms to form crystalline structure is suppressed by the entanglement of the polymer chains. Hence, polymers are normally semi-crystalline which means the crystalline polymers consist of small randomly oriented crystalline regions in an intervening amorphous phase. Furthermore, not all polymers have the ability to crystallize. The rate and extent to which polymers crystallize depends on different factors such as the rate of cooling when annealing the sample, the substrate, the amount of chain branching, molecular weight, and chemical perturbations such as co-units [27, 46].

The typical length to diameter ratio of polymer molecules is 10000. These relatively long molecules try to line up to minimize Gibbs free energy in their equilibrium state but the entanglement of the chains limits the mobility of the monomers and hinders alignment of the chains. Random folding of the molecules in the polymer gives rise to non-crystalline domains; this occurs when the molecules cannot rearrange to align and find the minimum free energy during the process of cooling or solvent evaporation. In fact, experimental results have shown that crystallinity in dilute polymer solutions, in which the molecules are isolated coils, is larger compared to that of melt-crystallized polymer films [46].

The chains in the crystalline regions of the polymers lie side by side along particular directions and the crystalline structure can be specified by a regular repeat pattern of atoms. The repeating unit is called the unit cell. In polymers each unit cell can have tens to hundreds of different atoms. In a crystal domain, atoms are bound together by covalent bonding along the polymer chain but held together by hydrogen bonding or van der Waals forces between chains. When a large single crystal of a material is available, it is possible to determine the structure of the crystal using X-ray diffraction and a three dimensional picture of the unit cell can be obtained according to the positions and intensities of the peaks in the X-ray diffraction profile of the sample. Since large single crystals are not available for polymers, modified methods are used to determine the crystalline structure and results are not as precise as they are for single crystals. According to Bragg's law, each peak in the X-ray diffraction pattern is related to specific crystallographic planes in the unit cell. In order to determine the structure, each peak should first be assigned to the crystallographic indices hkl. The indexing process is complicated even for single crystals and is much more difficult for semi-crystalline polymers. In polymers, crystalline regions are small, of the order of 10 nm, and the crystal orientations are not perfect, consequently the peaks are broader which means X-ray diffraction patterns have less resolution compared to large single crystals. Therefore, indexing usually is not sufficient for determining the structure and sometimes further information can help eliminate possibilities. For example, facts such as the nature of the polymer chain does not change due to binding in the crystal and the closest distance of the atoms in the structure cannot be less than the van der Walls' radii, can be taken into account [44, 46].

X-ray diffraction patterns for amorphous polymers or amorphous materials such as glasses or liquids contain one or two broad features or 'halos' while highly crystalline polymers demonstrate sharp peaks in their X-ray profiles. By comparing the peak positions of these crystalline peaks to that of the known crystalline structures of the polymer it is possible to index the peaks and consequently find out what crystalline phase can be attributed to the crystalline peak.

When the material that causes the X-rays to scatter is the same in the crystalline and amorphous regions of the sample, the degree of crystallinity x_{cr} can be estimated as [44, 46]:

$$x_{cr} = \frac{\int_0^\infty I_{cr}(q) q^2 dq}{\int_0^\infty I_{total} q^2 dq} \times 100\% \ , \tag{4.1}$$

where I_{cr} is the scattering due to the crystalline regions and I_{total} is the total scattering. We will use this method for a graft system in which the material of the crystalline domains is not necessarily the same as that of the amorphous domains. However, this method still provides a good estimate of the overall degree of crystallinity of the samples.

4.2 Crystallinity in PEMs

Morphological studies on Nafion and other PEM materials indicate that crystallinity can play an important role in the properties of the PEM. It has been suggested that crystallinity has a strong effect on the mechanical properties and the water content of the membrane, and that crystallinity can be used as a way to manage water uptake [47, 18, 48]. More importantly, crystallinity can affect the phase separation [26] and hence influence morphological related properties such as conductivity. Moreover, WAXS studies have been used to help interpret the characteristic features found in SAXS and SANS data. For example, Schmidt-Rohr and Chen proposed a model for Nafion [18] which consists of parallel cylindrical water channels with diameters between 1.8 to 3.5 nm and a persistence length of 20 nm. According to this model, the water nano-channels are continued in a stiff polymer backbone matrix which contains 10 vol% crystallites. The crystallites form domains parallel to the water channels. They suggest that the crystalline domains help to align the water nano-channels. The SAXS and SANS feature at lower q values was attributed to these crystallites.

Studies show that the crystallinity of Nafion is negatively correlated with the IEC values [49, 50, 51, 52]. This observation can be understood based of the facts that, in Nafion, the IEC value depends on the density of the side chains along the backbone, and that increasing the density of side chains generally leads to a decrease in the crystallinity of the backbone [49, 50, 51, 52].

Sacca *et al.* [53] have compared the nanostructure of recast Nafion membranes with that of commercial Nafion. They dried recast membranes at 80°C and 150°C and obtained a semi-crystalline structure. By comparing the SAXS results of the water swollen samples with samples at ambient humidity they suggested that the polymer matrix in recast membranes undergoes less deformation when the membranes are soaked in water. Based on the observation that the recast membranes were more crystalline they indicated that crystallinity increases the elastic energy of the PTFE matrix which leads to an increase of the stiffness of the structure and improves the mechanical properties of the membrane leading to lower water uptake.

In an earlier study Gebel *et al.* [48], using wide angle x-ray scattering, were able to show that the size of the crystalline domains can be increased by annealing the Nafion membranes at temperatures higher than 80°C. Also, they noticed that annealing leads to development of long-range order in the membrane. Moore and Martin [54] compared high-temperature ($> 125°C$) and low-temperature ($< 70°C$) solution-cast films with as-received Nafion and found that, although both of the recast membranes contain ionic clusters, only the high-temperature solution-cast membranes are partially crystalline and that they have better mechanical properties. They also reported that the low-temperature solution-cast membranes are brittle with poor mechanical properties and high water uptake. As a result of this observation they suggest that the crystalline domains act as cross-links in the polymer and provide a stiffer matrix which absorbs less water. The wide angle X-ray data in their study were noisy so that they were only able to distinguish samples containing crystalline domains based on their asymmetric X-ray patterns and were not able to estimate the degree of crystallinity.

Luan *et al.* [55] have studied another perfluorosulfonic ionomer which is similar to Nafion. They found that samples cast at higher temperatures include larger crystal domains while samples cast at lower temperatures have a higher degree of crystallinity but smaller crystals, as their crystalline peaks were wider. They observed that samples with bigger crystal domains absorb less water and have better mechanical properties. Therefore, they suggested that having larger crystal domains is more important than the degree of crystallization in the membrane in order to acquire better mechanical properties.

According to the studies listed above, it appears that crystallinity could be a key parameter in controlling the water swelling properties of PEMs. However, Nafion membranes prepared at higher temperatures have both a higher degree of crystallinity and larger crystalline domains. So it is not possible to decide which factor is more important. Also, as mentioned previously, the amount of crystallinity in Nafion depends on both the IEC value and the density of side chains along the backbone, therefore it is not clear in what way each of these factors affects crystallinity. Investigating the correlation between crystallinity, phase separation, and water content of ionic graft membranes is one of the goals of this study.

The copolymer that we are investigating consists of a fluorous backbone; P[VDF-*co*-CTFE]. PVDF is a crystallizable polymer and three crystalline phases have been observed in this polymer [56, 57]. Phase I has a polar structure with planer-zigzag (all *trans*) chains packed in the unit cell and carbon difluoride CF_2 dipoles parallel to the b axis. This structure is monoclinic. Conformation of the chains in phase II is *trans gauche trans gauche' (TGTG')* and its structure is orthorhombic. It also has the most stable structure and can be easily obtained under normal circumstances and thus is the most common one. Phase III of PVDF is thought to have an intermediate polar configuration between phase I and II. Polystyrene side chains on the other hand, are not crystalline, although the WAXS patterns of polystyrene show two broad peaks.

4.3 WAXS results

WAXS results for PVDF and four P[VDF-*co*-CTEF] macroinitiators are shown in Fig. 4.1; the CTFE mol% of these macroinitiators are 1.1, 2.6, 4.4 and 5.8 mol%, where macroinitiators with 2.6 and 5.8 mol% CTFE are the ones that were used to synthesize the graft copolymers that are the focus of this thesis. All of these WAXS patterns possess a rather sharp peak on top of a broad peak. The broad peak is associated with scattering from the amorphous part of the sample while the peak positioned at $q = 14.5$ nm^{-1}, is the crystalline peak, resulting from scattering from the crystalline part of the samples. The peak position of this peak is consistent with scattering from (100) planes of the type II crystal phase of PVDF. As the mol % of CTFE increases the crystalline peak diminishes. These results are consistent with the fact that co-units along the backbone chains act as defects and hinder the crystallization of the backbone [27].

Figure 4.2 compares the WAXS data for unsulfonated and sulfonated PS with that of the 2.6 mol% CTFE macroinitiator. WAXS data of unsulfonated PS has two amorphous peaks. The peak positioned at higher q values is a typical amorphous peak observed for amorphous polymers, and corresponds to the length scale of $d = 0.5$ nm. However, the peak located at smaller q values corresponds to the length scale of $d = 1$ nm and indicates that there exists some preferred alignment for the polymer chains at larger scale. In the case of PS, this peak is associated with the chain-to-chain spacing [58]. As the sample becomes partially sulfonated this peak disappears, indicating that the sPS chains are randomly oriented and the pre-existing order is reduced upon sulfonation.

Figure 4.3 shows the X-ray intensities for samples of the LGD series with different lengths of side chains and Fig. 4.4 shows the WAXS results for samples of the HGD samples with short side chains. For each set of data we observed 3 or 4 peaks. The first peak is positioned near $q = 7$ nm^{-1} and indicates the polystyrene chain-to-chain order [58], consistent with the low q peak seen for PS in Fig. 4.2. The intensity of this peak decreases as the degree of sulfonation increases which implies that the chain-to-chain order for the polystyrene chains

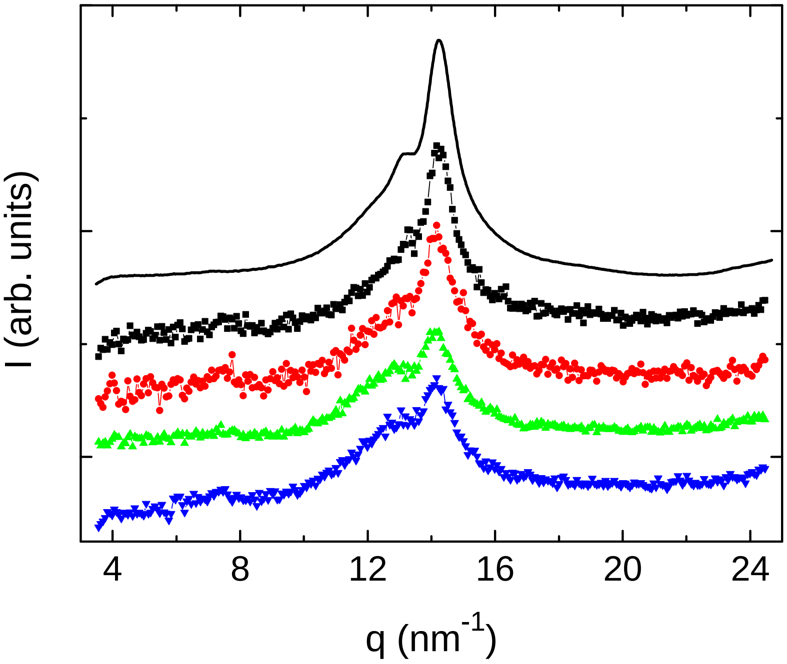

Figure 4.1: X-ray diffraction data for P(VDF-*co*-CTFE) containing 1.1 (■), 2.6 (●), 4.4 (▲) and 5.8 mol% (▼) CTFE compared to that of PVDF (—). X-ray intensity is plotted as a function of scattering vector q. Data for macroinitiators were acquired on the Siemens D5000 and that for PVDF on the Rigaku Rapid Axis. X-ray data are shifted vertically to improve visualization.

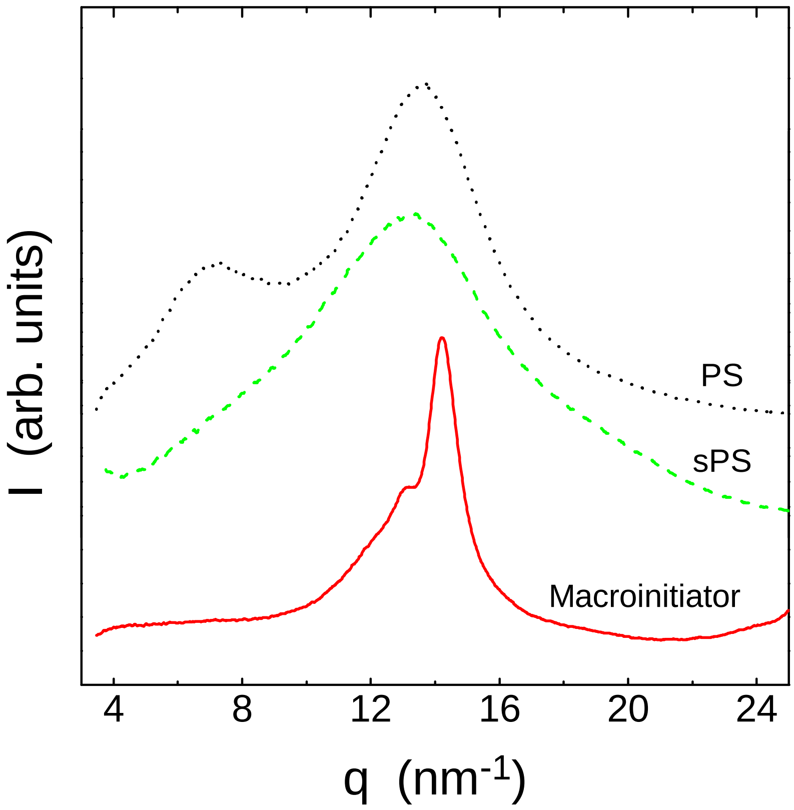

Figure 4.2: WAXS data of unsulfonated polystyrene (PS) compared to that of partially sulfonated polystyrene (sPS) and macroinitiator containing 2.6% CTFE. The broad peak positioned at 7 nm^{-1} is associated with the arrangement of polystyrene chains when not sulfonated. This peak disappears upon sulfonation.

decreases as the polymer becomes sulfonated.

The second peak, observed at $q = 12$ nm^{-1}, is the main amorphous peak. The amorphous parts of the samples, including both backbones and side chains, contribute to this peak.

The third peak, located on the large-angle side of the amorphous peak and positioned around $q = 14.5$ nm^{-1}, is the crystalline peak. This peak is due to scattering from the crystalline domains of the backbone. The peak position of this peak is consistent with the one observed in WAXS data of PVDF and macroinitiators and hence this peak is attributed to the scattering from (100) planes of the type II crystal phase of PVDF.

Some samples also show evidence of a fourth peak, a broad bump centred around $q =$ 20 nm^{-1}. After doing a number of experiments on hydrated samples, we have concluded that this peak corresponds to the water molecules in the sample. In these experiments, a fully hydrated sample was obtained by putting a sample in water overnight. The sample was removed from the water and a sequence of WAXS measurements were performed with an interval of 10 minutes. During this period the sample was exposed to air and became dehydrated. As shown in Fig. 4.5, the fully hydrated sample shows a rather huge amorphous peak positioned at $q = 20$ nm^{-1}. The amplitude of this peak decreases as the sample dries, while the amorphous and crystalline peak at lower q become more pronounced. It is interesting to notice that the crystalline peak is always present, even when the sample is completely hydrated.

In order to estimate the degree of crystallinity, we fit three Gaussians to the data in the range of 4.5 to 16 nm^{-1}. These curves correspond to: the chain-to-chain order of the polystyrene, the amorphous domains including both the backbone and polystyrene side chain, and the crystalline domains of the backbone. Figure 4.6 (a) and (b) contain the fit results to the WAXS data corresponding to the unsulfonated and partially sulfonated samples of the LGD, receptively. As shown in these figures, we avoid the hydration peak, during the fitting procedure, because it does not have a well-defined behaviour. From the Gaussian curves we calculated the crystallinity using Eq. 4.1, the results are shown in Fig 4.8. We use Igor Pro. 6 to fit the data. The fitting procedure is based on least squares curve fitting.The baseline was chosen such that it was tangent to the WAXS data at larger q values. In order to set the initial values for the fitting process, peak positions of the Gaussian curves were chosen close to the peak positions of the WAXS data. For the first few iterations the peak positions were fixed. This eventually leads to a fitting curve that is close to the data. At this point the peak positions were allowed to float and the best fit was obtained after a

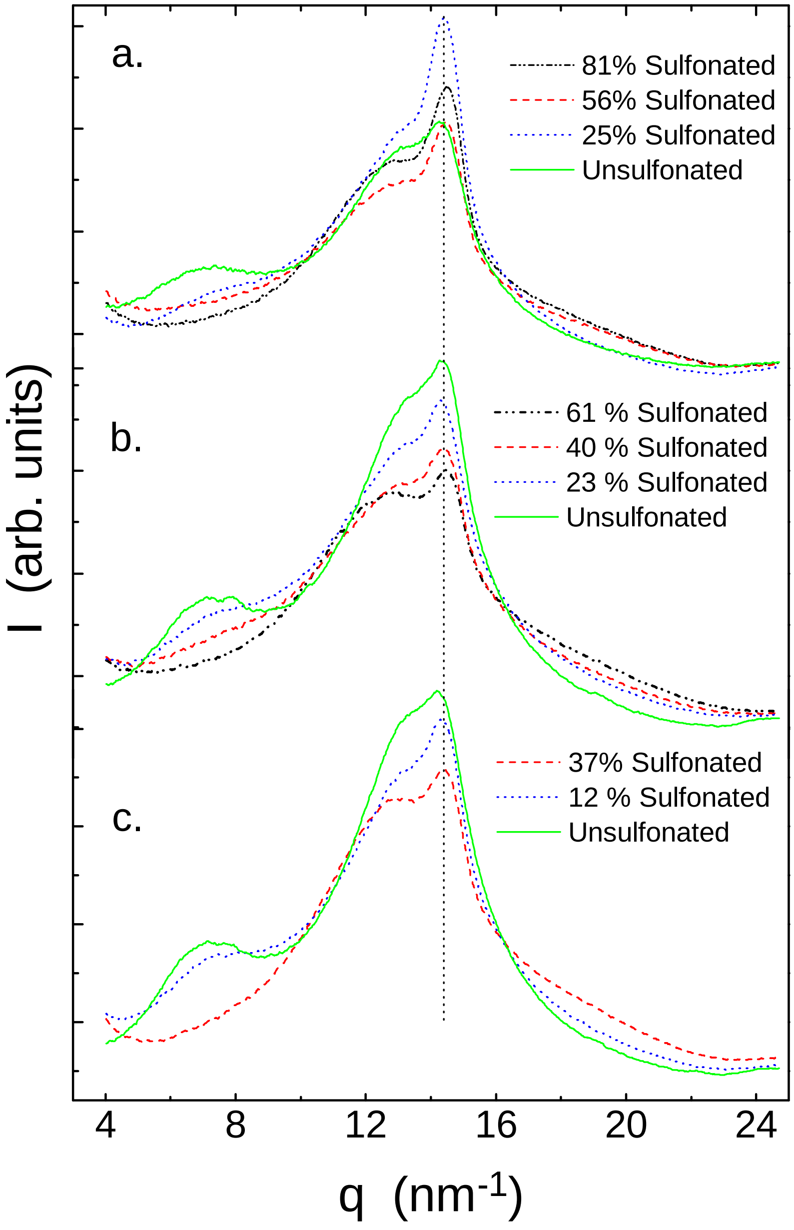

Figure 4.3: X-ray diffraction data for samples of the LGD series with (a) short, (b) medium, and (c) long side chains, corresponding to degrees of polymerization of $n = 39$, 62 and 79, that have been sulfonated to different degrees. X-ray intensity is plotted as a function of the scattering vector q. X-ray patterns for each set are shifted vertically to improve the visualization.

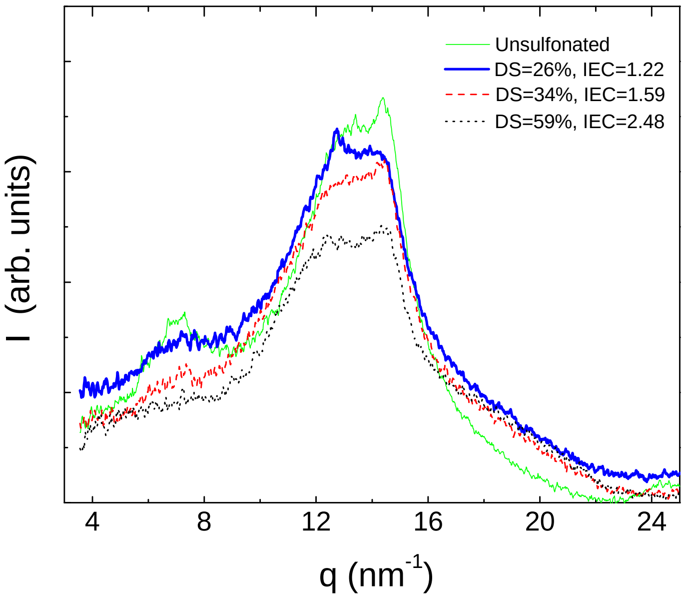

Figure 4.4: WAXS patterns corresponding to samples of the HGD series with the shortest side chains at different degrees of sulfonation.

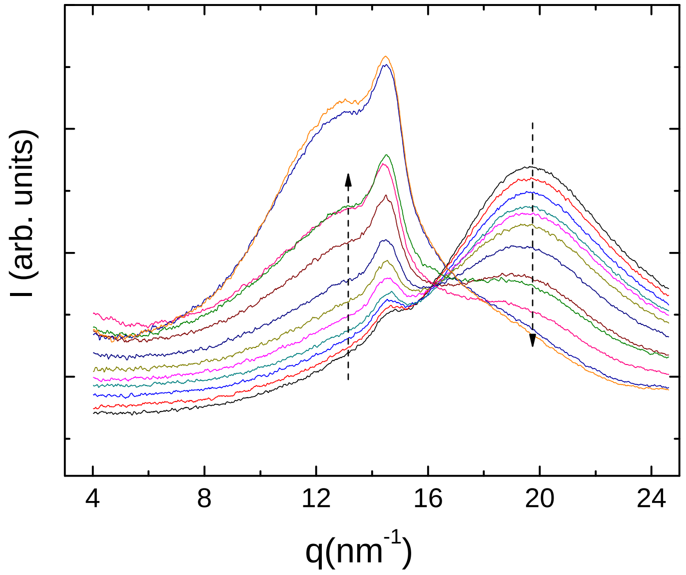

Figure 4.5: X-ray diffraction patterns of a sample from the LGD series with a long side chain and degree of sulfonation of 43%. A fully hydrated sample was mounted in the X-ray instrument and data were collected as the sample became dehydrated in the instrument. Data collection for each run took 2 min and the time interval between each run was 10 min. Arrows show the direction of time as the WAXS data evolves over time.

few iterations. All parameters except the baseline were floated for the final fit results. For each sample, data was collected at three different points in the sample to make sure that the sample is uniform. The mean value obtained for the degree of crystallinity was reported as the degree of crystallinity. The mean square root was considered as the uncertainty of the measurements.

Unlike samples of the LGD series, the degree of crystallinity in the samples of the HGD series was estimated to be lower than 4%. As illustrated in Fig 4.4, WAXS intensities of these samples show only a weak crystalline peak.

4.4 Discussion

The factors that might affect the degree of crystallinity in our copolymers are: the amount of CTFE along the backbone, the graft number density, the length of the side chain, and finally the degree of sulfonation of the side chains.

For the macroinitiator there are only the CTFE co-units along the backbone to hinder the crystallization. Figure 4.7 shows how the degree of crystallinity of the macroinitiators is affected by the percent of the CFTE co-units compared to that of PVDF. Our results indicate that 1.1% CTFE does not affect the degree of crystallinity, however, beyond this CTFE content the degree of crystallinity decreases linearly; the degree of crystallinity is only 12% in samples where the CTFE has been increased to 5.6%. Therefore, we conclude that the CTFE content is one of the important limitations of the crystallization process.

The degree of crystallinity in the backbone is reduced by roughly 60% for all of the LGD samples when compared to that of the macroinitiator, except for the sulfonated samples with short side chains (n=39). The decrease in crystallinity for these samples is only about 25% and indicates that crystallinity is affected by sulfonation only when the sample has a rather short side chain. At this stage we do not have a precise explanation for these behaviours.

Graft number density is another hindering factor and we expect to see less crystallinity for graft polymers compared to their macroinitiators. We should be cautious, as graft side chains incorporate amorphous PS/sPS, which inherently decreases the overall degree of crystallinity of the sample. Moreover, we should keep in mind that these three factors, graft number density, length of the side chain and the styrene ratio, are not independent factors. Comparing the short samples of different macroinitiators with roughly the same styrene ratio we can say that graft density along the backbone and CTFE density are the most important factors.

Our results are in agreement with results obtained by Zhang *et al.* [38, 59]. They investigated the crystallinity of graft systems using differential scanning calorimetry (DSC). Although they did not quantitatively analyse their data, their results indicate that the CTFE content of the backbone and the graft number densities act as hindering factors of crytallinity. Furthermore, their results show that the overall pattern of DSC data stays the same upon sulfonation which indicates that degree of crystallinity is not much affected by sulfonation and consistent with our results.

4.5 Summary and conclusion

We studied crystallinity in graft samples based on two macroinitiators. We observed considerable crystallinity in all of the samples of the LGD series. In contrast, crystallinity in the HGD samples was determined to be $< 5\%$. Our results indicate that crystallinity is affected by sulfonation at least in samples with short side chains, although we have not observed a systematic effect with degree of sulfonation. More over, the co-units and side chains act to hinder the crystallinity. These results are consistent with the results obtained for similar polymeric systems [38, 59].

Figure 4.9 compares the water content of the LGD and HGD samples with short side chains, as a function of IEC. These two sample sets have very similar PS ratio and length of the side chain, however, the water content values of the LGD samples are less that the other set. As LGD samples are crystalline, we suggest that the lower water content in this case originates from their crystallinity. In the next chapter, I will discuss the effect of the crystallinity on the phase separation and argue whether crystallinity has a direct impact on water content, or its effect on water content is through affecting the phase separation.

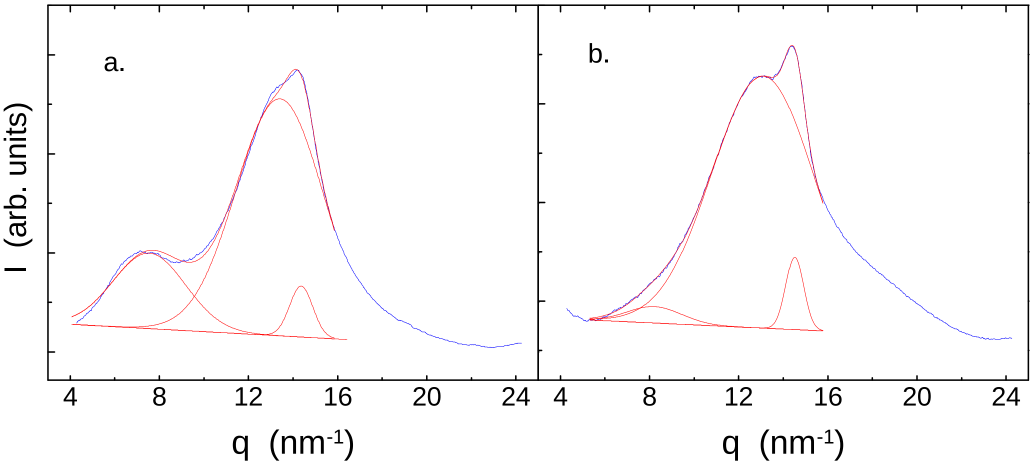

Figure 4.6: WAXS data and fits for samples with low graft number density and long side chains: (a) unsulfonated, (b) $DS = 43\%$. Three Gaussian curves and a baseline were fit to the data to analyse the WAXS patterns. The upper limit of the q range used in the fit was set to $q = 16\ \mathrm{nm}^{-1}$ to avoid the peak due to water domains.

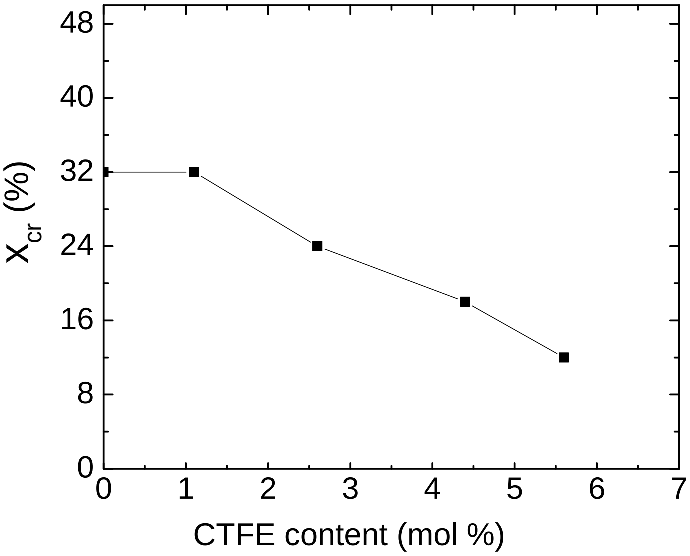

Figure 4.7: Degree of crystallinity for macroinitiators with different CTFE % cast under the same condition.

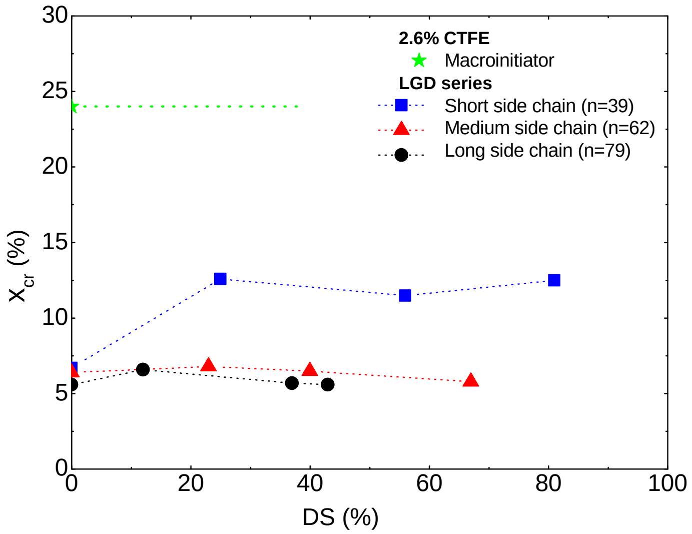

Figure 4.8: Degree of crystallinity for samples of LGD and the macro initiator. These values belong to the overall degree of crystallinity and are not corrected for the PVDF ratio.

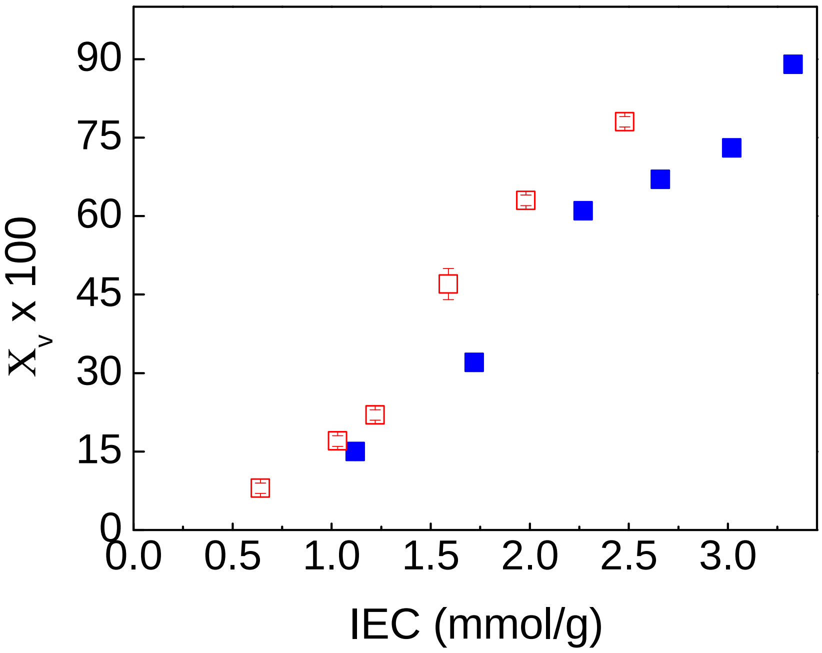

Figure 4.9: Water content values of HGD (□) and LGD (■) samples with short side chains plotted as a function of IEC. Samples of LGD have a lower water content compare to the other sample set. The unsulfonated samples of these two series have similar PS ratios and length of side chains. The biggest difference is that LGD samples are crystalline. Therefore we associate their lower water content with their cystallinity.

Chapter 5

Fluorous domains

5.1 Introduction

In this chapter we investigate the phase separation of the fluorous backbone. First I review some the relevant works on the morphology of ionic copolymers and present the SAXS and SANS results. I will introduce the Kinnig-Thomas model which was used to fit our scattering data. Based on this model, we characterise the fluorous domains and find out how factors such as crystallinity and sulfonation affect the morphology. In conclusion, I argue how different factors such as fluorous volume ratio and crystallinity affect the water content properties.

Figure 5.1 shows a typical SAXS data of Nafion which contains ultra SAXS results, as well as SAXS measurement. The main characteristic features in this data are two peaks; one peak located at higher q values ($0.2\mathring{A}^{-1}$), which is humidity dependent, and the other peak located at smaller q values ($0.04\mathring{A}^{-1}$), which is correlated to the degree of crystallinity. These two characteristic features are known as ionomer peak and matrix knee, respectively. There have been several attempts to interpret the SAXS/SANS features of Nafion and to distinguish the origins of these peaks [6, 15, 16, 17, 18, 50, 60, 61, 62, 63, 64, 65]. However, there is no consensus among researchers regarding the morphology of Nafion [10, 11, 20, 64]. These complications motivated researchers to design model polymeric systems to investigate the structure-morphology-property relationships of the PEM materials. It is important that extracting the morphology of these model polymeric systems be simpler than that of Nafion. Ionic copolymer systems are desirable candidates to be considered as model polymeric systems of PEMs [2, 12, 26, 66, 67]. These types of ionomers are usually designed such that one block is ionic, and has the ability to form hydrated domains, when exposed to water, while the other block is neutral and can provide good mechanical properties. In principle, the ionic block is responsible for proton conduction and the neutral block maintains the mechanical integrity of the membrane. Without doubt, the phase separation and morphology of ionic copolymers is more complicated than the conventional (non-ionic) copolymers, yet, can be much simpler than that of Nafion [20, 26]. In the ionic copolymers, phase separation consists of two aspects: the segregation of the two different types of blocks, and the aggregation of acid groups, the second one being dominant as it is caused by electro-static interactions.

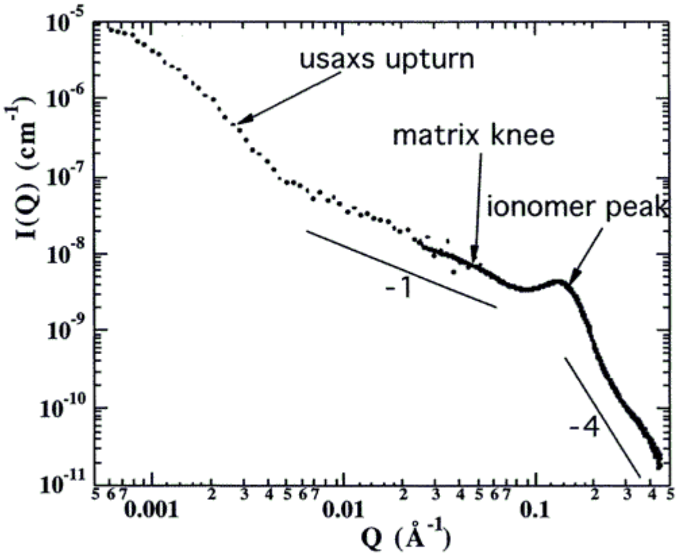

Figure 5.1: SAXS data corresponding to hydrated Nafion. From [17], used with permission.

The simplest ionic copolymer system is the diblock system. In contrast to conventional diblocks, phase separation of the ionic diblocks is not very well studied. In fact, recent studies indicate that these materials have unusual behaviours [33, 68]. Balsara *et al.* [33] studied the effect of degree of sulfonation and molecular weight on the morphologies of sulfonated poly(styrene-*b*-methylbutylene) (sPS-*b*-PMB) possessing very narrow molecular weight. They used SAXS and TEM techniques to investigate the morphology and noticed that varying the degree of sulfonation leads to different morphologies, even though no morphological change was expected due to changes in the volume fraction upon sulfonation.

They also discovered that molecular weight plays an important role in determining the morphology of the studied systems. Similar unconventional behaviours were reported by other groups [69, 70, 71]. The conventional phase behaviour in ionic diblocks was also reported. Rubatat *et al.* [12] studied two series of sulfonated poly([vinylidene fluoride-*co*-hexafluoropropylene]-*b*-styrene diblock copolymers. One series was partially sulfonated (20 to 40%) with PS volume fraction of 44%. The other series was fully sulfonated with low PS ratio (10%). They observed that the first series obtained lamellar structure, while the second series formed disordered morphology. The formation of disordered morphology was attributed to the low values of χN. In their work, the morphology was examined by both TEM and SANS measurements.

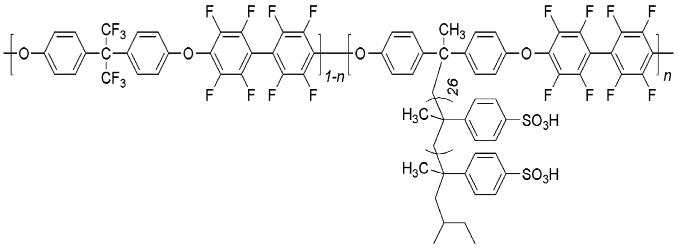

Figure 5.2: Chemical structure of comb-shaped copolymer studied by Nieh *et al.* [72]. From [72], used with permission.

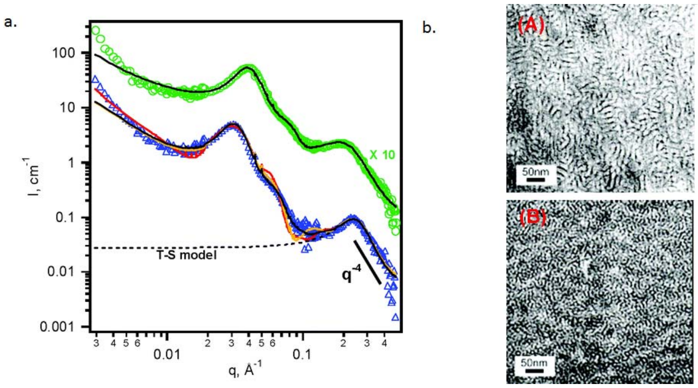

Figure 5.3: (a) SANS data corresponding to hydrated comb-like copolymers possessing IEC values of 0.87 (△) and 1.6 (○) mmol/g. (b) shows the corresponding TEM images [72]. From [72], used with permission.

In contrast to the ionic diblock copolymers, the morphology of the ionic graft systems have been examined by a few groups. The main reason is that creating well-defined microstructures possessing controlled ion content is very challenging in terms of synthesizing the materials. Moreover, most of these studies used only TEM techniques to investigate the morphology [1, 38, 73, 74]. In fact, an in-depth morphological study on ionic graft systems such as PEM materials has not yet been established [2].

Regarding this particular architecture, Nieh *et al.* [72] studied the morphology of a series of ionic comb-shaped copolymers using TEM and SANS measurements. Figure 5.2 shows the chemical structure of the studied materials. In this work, three samples with IEC values of 0.87, 1.2, and 1.6 mmol/g were investigated. As shown in Figs. 5.3 (a) and (b), SANS data of the hydrated samples exhibit two characteristic peaks and their TEM images reveal worm-like morphology. Therefore, they proposed a morphological model which had two independent contributions. One contribution consisted of a worm-like form factor $F_{WL}(q)$ and hard disk structure factor S_{HD}. The form factor was inspired by worm-like objects observed in the TEM images, and the structure factor was considered to account for multiple scattering from multiple worm-like objects. Hence, the scattering function for the peak located at lower q values was written as the product of the form factor and structure factor

$$I(q) = K S_{HD}(q) F_{WL}(q), \tag{5.1}$$

where K is the amplitude and depends on three factors: the difference between SLD values of the phases, volume fraction of the hydrophobic domains, and the volume fraction of individual cylindrical aggregations. Nieh *et al.* [72] only discussed the fit results of samples with highest and lowest IEC values. According to their results, the effective average radius of the hard disk corresponding to these two samples were 9 and 6.7 nm, respectively. In this study, the other peak was attributed to water-rich domains in the sample. They considered a bicontinuous morphology to describe this peak. This part of the model will be discussed in the next chapter.

Similar to the comb-like system studied by Nieh *et al.* [72], the ionic graft system that we investigated in this thesis consists of a hydrophobic backbone and hydrophilic side chains. We will examine two aspects of the morphology of this system: the formation of hydrophobic domains, and formation of water-rich domains. In this chapter, we investigate the first aspect based on the SAXS and SANS data corresponding to dry and hydrated samples, respectively.

5.2 SAXS and SANS measurements

The initial focus of this study was on sulfonated samples as one of the goals was to shed light on the relation between the structure-morphology-property of PEM materials. However, we decided to examine the morphology of unsulfonated samples, as well, because knowing the morphology of unsulfonated samples facilitates better understanding of the morphology of sulfonated samples. It also provides insight on the effect of sulfonation on the morphology of the membrane.

Unsulfonated samples

The morphology of the unsulfonated samples is due to the phase separation between the fluorous backbone and the PS side chains. Therefore, it is less complicated compared to the morphology of sulfonated samples, where there is a possibility of separation into three phases. Although unsulfonated samples do not absorb water, we ran the scattering measurements on these samples under the same condition in which we measured the sulfonated samples, for the sake of consistency, *i.e.* unsulfonated samples were also immersed in D_2O for SANS measurements.

Figure 5.4 (a) and (b) contain SAXS and SANS data of the unsulfonated samples of LGD and HGD series, respectively. Generally, the scattered intensity of both SAXS and SANS data decreases gradually over the q range of 0.02 to 2 nm^{-1} and contains one characteristic peak. For samples with long and medium side chains this peak is followed by another characteristic feature. Since it is located at $q \sim 2q^*$, where q^* is the position of the main peak, it can be interpreted as a second order peak. The existence of this second order peak indicates that theses samples have a more ordered morphology. The position of the main peak for the same sample is generally located at a similar q-value for both SAXS and SANS data. Peak positions of SANS and SAXS data are consistent in the LGD series (Fig. 5.4 (a)). There is some variation with the peak position for samples with different length of side chain. For example, peak positions of samples with long and medium side chains in the LGD series (Fig. 5.4 (a)) are located at $q = 0.35$ nm^{-1}, while shifted to $q = 0.45$ nm^{-1} for samples with short side chains. In the case of the HGD series (Fig. 5.4 (b)), peak positions of the SANS and SAXS data are slightly shifted to the left or right. In this series, the characteristic peaks for samples with medium and long side chains are located at $q = 0.5$ nm^{-1} (Fig. 5.4 (b)) , while they are located at $q = 0.6$ nm^{-1} for the sample with short side chains. This scattering feature is characteristic of nano-size domains with weak ordering. Since these samples are primarily polystyrene, the fluorous volume fraction is less than 35%, we infer that backbone segments phase separate and form nano-size domains embedded in PS continuous phase.

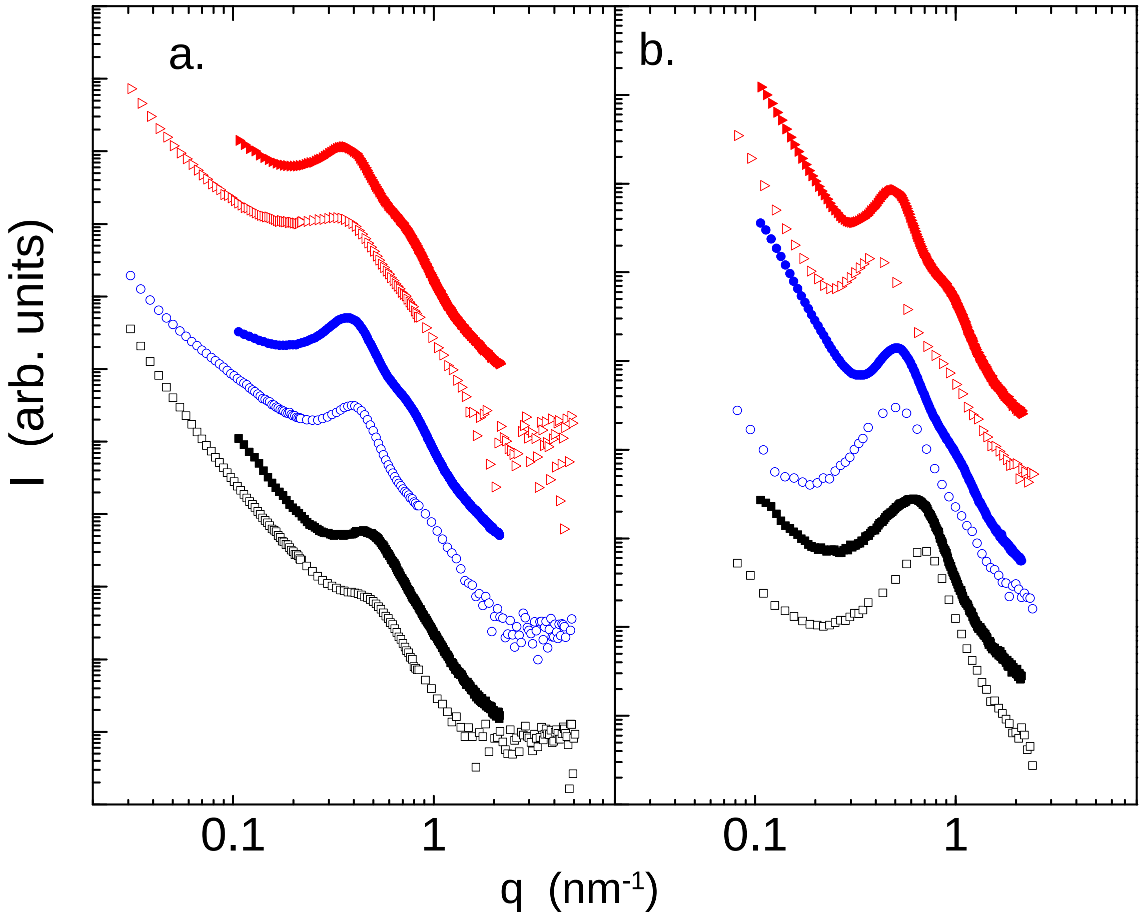

Figure 5.4: SAXS (solid symbols) and SANS (open symbols) patterns corresponding to unsulfonated samples of the (a) LGD and (b) HGD series. ▷, ▶ : long side chain, ○, ●: medium side chains and □, ■: short side chains. Vertical axis is integrated intensity and horizontal axis is q in nm^{-1}.

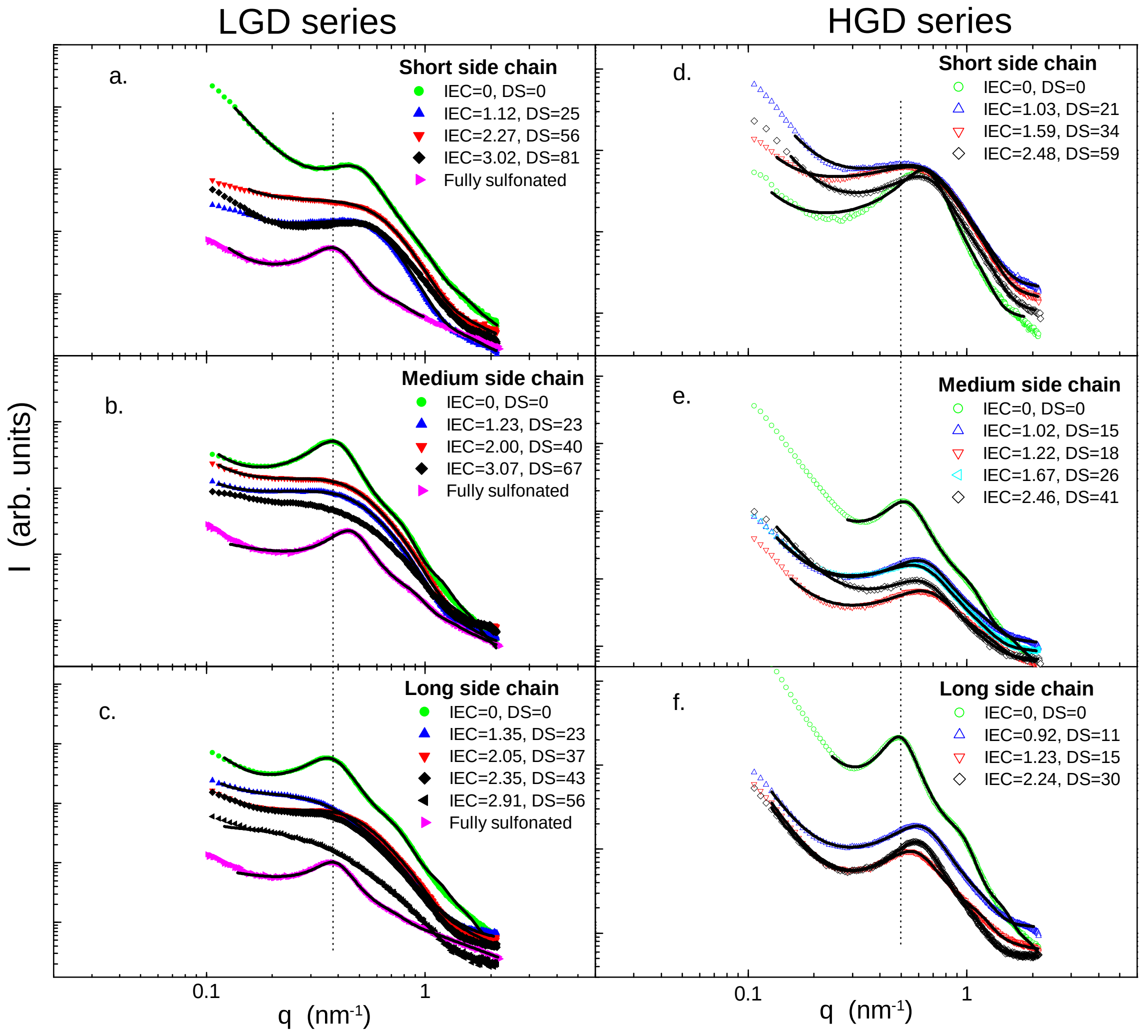

Figure 5.5: SAXS data for graft copolymers of the LGD and HGD series shown on left and right hand side, respectively; on the left hand side (a) short series (n=35) (b) medium series (n=88) and (c) long series (n=154) and on the right hand side (d) short series (n=39) (e) medium series (n=62) and (f) long series (n=79). Vertical axis is integrated intensity and horizontal axis is q in nm^{-1}. The solid line on each data set shows the fitting results.

Sulfonated samples

Figures 5.5 (a)-(c) and (d)-(f) show the SAXS data corresponding to the sulfonated samples, in addition to that of unsulfonated ones, for the LGD and HGD series, respectively. The general SAXS profiles of the sulfonated samples are similar to those of the unsulfonated samples and the position of the main peak is generally very similar. However, the main peak is generally less-pronounced in the sulfonated samples. This indicates that the morphology is less ordered upon sulfonation. SAXS data of fully sulfonated samples are also available the LGD series. It is interesting to notice that in the case of fully sulfonated samples, the characteristic peak becomes more pronounced and the second order peak is distinguishable (Figs. 5.5(a)-(c)). These observations suggest that unsulfonated and fully sulfonated samples are more ordered than partially sulfonated ones.

These samples are not stained or hydrated, therefore characteristic features corresponding to water-rich or ion-rich domains are not pronounced in the SAXS data [13, 14]. In addition, the consistency between the peak positions in the unsulfonated, partially and fully sulfonated samples led us to conclude that the characteristic peaks in SAXS data originated from the scattering of fluorous domains embedded in a fully/partially sulfonated polystyrene continuous phase. Further evidence regarding the origin of these features will be provided based on SANS patterns of hydrated samples.

In order to study the effect of hydration on the morphology of fluorous domains, we performed SANS measurements on samples immersed in a solvent of (D_2O:H_2O=70:30). As mentioned in Chapter 3, the scattering length density of this solvent matches that of PS, reducing the contrast between PS and water domains so that we could study the fluorous domains embedded in a matrix that was effectively uniform. Figure 5.6 shows the SANS data obtained for hydrated samples of LGD series. The overall scattering profiles of the hydrated samples are similar to that of dry samples except that the characteristic peak moves to smaller q values as the water content increases. This shift to smaller q indicates that these samples undergo moderate swelling upon hydration at the nano-scale level. At low water content ($X_\mathrm{v} < 0.8$) the shape of the peak is relatively constant. At higher water content, the peak broadens as it continues to move to smaller q. These samples swelled excessively and were very soft and delicate to handle. The similarity in peak shape below $X_\mathrm{v} = 0.8$ indicates that the morphology is relatively constant at moderate swelling.

In our previous work [1, 22], as described in Chapter 3, we examined the morphology

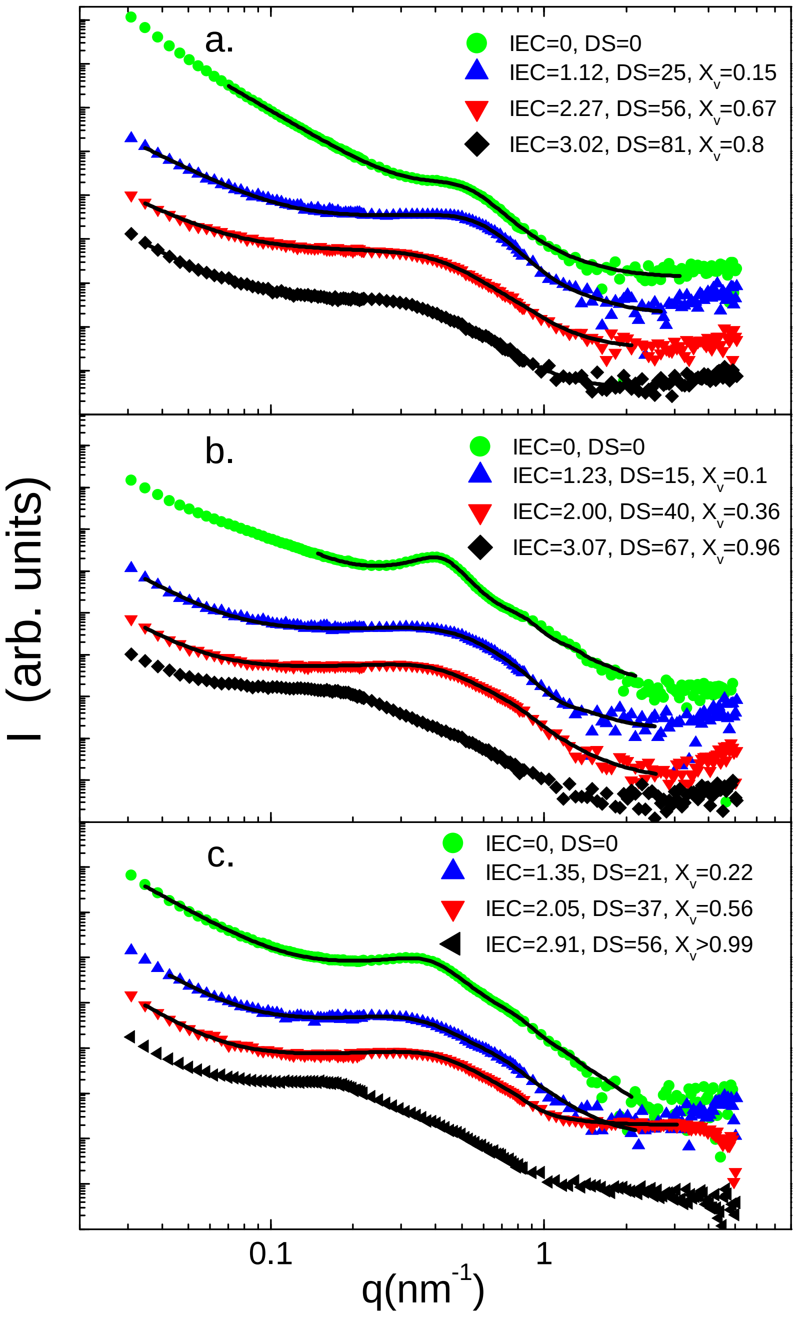

Figure 5.6: SANS data for graft copolymers samples of LGD series: (a) short (n=39), (b) medium (n=62) and (c) long (n=79) side chains. Samples are immersed in D_2O:H_2O=70:30 in order to match the contrast between PS and solvent. The vertical axis is integrated intensity and the horizontal axis is q in nm^{-1}. The solid line on each data set shows the fitting results.

of the ionic aggregates using TEM imaging techniques. Our results indicated that the overall morphology for ionic aggregates was a random spheres morphology and there was no evidence of lamellar or cylindrical morphology. Consequently, we assume that fluorous domains also form random quasi-spherical domains. Although fluorous domains are not distinguishable from unsulfonated polystyrene, in TEM images, previous studies of copolymers showed that, if hydrophobic domains form lamellar structure, water-rich domains also up take lamellar order [12, 72]. Furthermore, TEM images on fully sulfonated samples suggest the existence of semi-quasi spherical fluorous domains. Therefore, we approximate these fluorous domains as spherical domains. Presumably, each fluorous domain is surrounded by its own graft side chains, therefore, it is logical to consider that a shell is associated with each domain. This configuration is schematically shown in Fig. 5.7. The consistency of this morphology with TEM images was tested by simulations, as discussed in Chapter 2. Kinning and Thomas [75, 76] used such a morphological model to describe the phase separation of polymeric systems such as poly(styrene-butadiene) diblock copolymer/polystyrene homopolymer blends. They studied a series of polymer membranes possessing a thickness of 1 mm. The membranes were acquired by solution casting method. TEM and SAXS measurements indicated that beyond a critical concentration of diblock copolymer, polybutadiene block forms micelles in a continuous phase of PS. These micelles have different shapes such a spherical, cylindrical or lamellar, depending on the concentration of the diblock copolymer. Kinning and Thomas used this model to examine the phase separation of the blend samples with spherical micelle configuration. They were able to characterize factors such as core radius, polydispersity of the core radius, shell thickness and concentration of unsegregated copolymer. They also studied the correlations between these parameters and other factors such as the molecular weight of copolymer [75, 76].

In fact, the Kinning and Thomas model is a modified version of the Percus-Yevick [77] hard sphere fluid model. The explicit mathematical calculations behind the model are summarized in Appendix A. In this chapter, we apply this model to investigate the phase separation of the fluorous backbone. In the next chapter, we use the same model to investigate formation of the water domains.

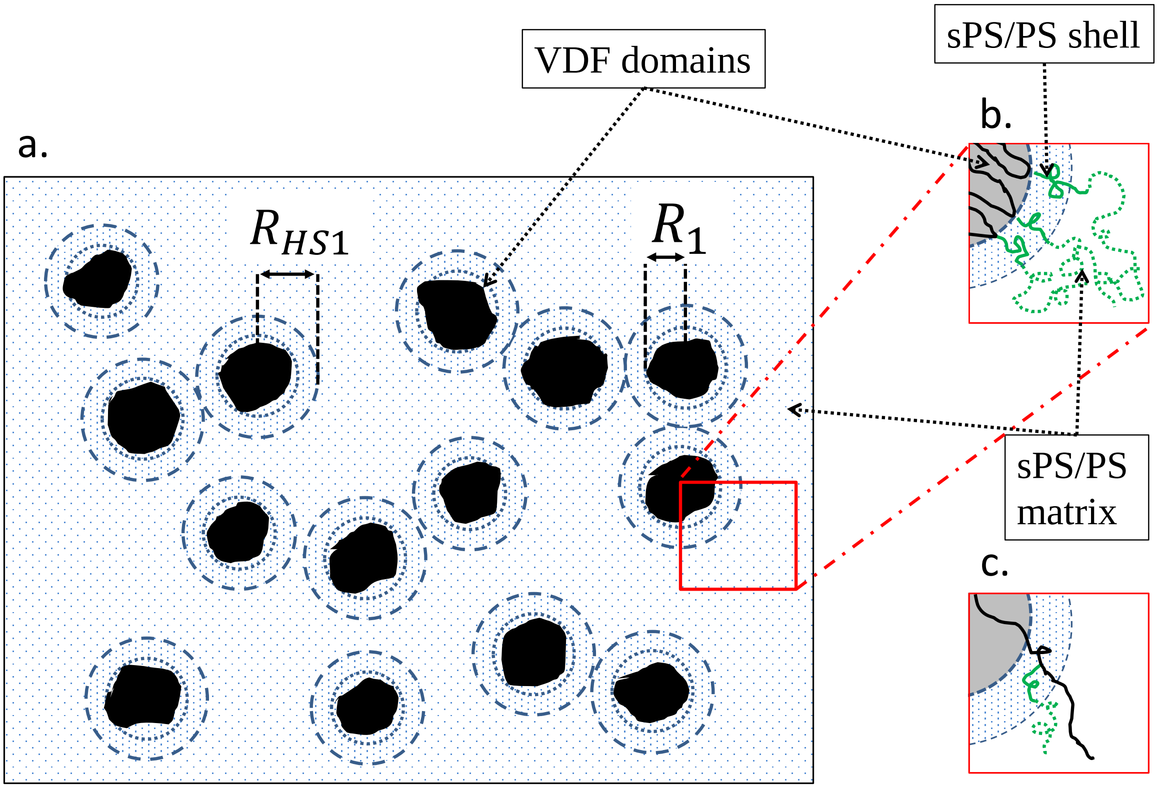

Figure 5.7: Schematic of the proposed model for morphology of the fluorous domains. We suggest the fluorous backbones form quasi-spherical domains, which can be approximated as polydisperse spheres embedded in a continuous phase of PS. In the graft architecture, side chains are chemically bound to the backbone, therefore, we considered a shell of PS for each domain. Inset (b) shows a possible configuration of chains in the PVDF core and PS shell. Inset (c) illustrates how the unsegregated backbone chains and their pendent side chains can contribute to the shell.

5.3 Characterization

We consider two contributions to analyse the scattering data in addition to a constant background. The first one is the Kinning-Thomas model to interpret the characteristic peaks, and the second is an exponential decay to account for the scattering at lower q values.

In the Kinning-Thomas model, the scattering is attributed to polydisperse spheres of radius R_1, as shown in Fig. 5.7 (a). In our particular system, the spheres are made of fluorous segments and are embedded in a continuous matrix a PS/sPS mixture. The Kinning-Thomas model also assumes a rigid shell around each domain. In principle, in graft system, this shell mainly consists of sPS/PS chains attached to the backbone chains that build a given domain, as shown in Fig. 5.7 (b). We refer to the core and its surrounding shell as a hard-sphere. The radius of the hard-spheres is R_{HS1} and are assumed to have a liquid like order. The volume fraction of these hard spheres is expresed as η_1. The relationship between the number density of the domains n_{D1} and volume of the membrane per domains V_{p1} are as follow

$$\eta_1 = \frac{4\pi}{3} R_{HS1}^3 n_{D1} \ , \tag{5.2}$$

and

$$V_{p1} = \frac{1}{n_{D1}} . \tag{5.3}$$

We observe an upturn at low q range in all the scattering intensities. This upturn is associated with large scale inhomogeneities in the samples [78]. Since this upturn has a decay exponent close to -4, we used an exponential decay with power of -4 in order to fit this feature. Other models, such a Debye-Buche [79], were examined for this upturn but were not successful. In fact, we do not have sufficient data points to fit any potential model to this upturn properly, hence we do not expect to extract significant information based on this upturn. Indeed, a more accurate analysis for this upturn would require ultra small angle X-ray scattering measurements [65, 78]. We also included a constant to account for the background and, therefore, the fitting function is expressed as

$$I_{KT}(q; A_1, R_1, \sigma_1, R_{HS1}, \eta_1, A_2, \alpha, Bkg) = A_1 \cdot I_{KT}(q; R_1, \sigma_1, R_{HS1}, \eta_1) + A_2 \cdot q^{-\alpha} + Bkg \ , \tag{5.4}$$

where R_1 and R_{HS1} are the average fluorous domain and hard sphere radii, as illustrated

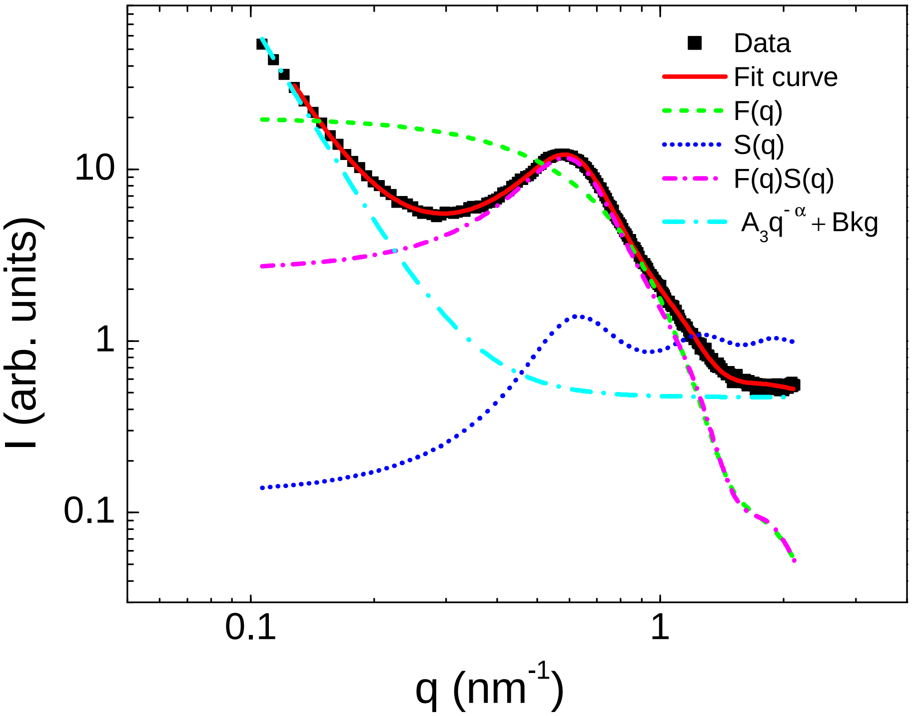

Figure 5.8: SAXS data corresponding to the sample with long side chains and $IEC = 2.24$ mmol/g. Different contributions to the fitting function are plotted.

in Fig. 5.7, σ_1 is the polydispersity of the domain size, A_1 and A_2 are the amplitudes for Kinning-Thomas and power law contributions, respectively, and Bkg is the constant background. In order to fit the results we used Igor Pro 6. We chose the initial fitting parameters such that the position of the peak in the fitting curve was close to that of the data. This was done by choosing R_1 in the range of 3 to 5 nm and R_{HS1} in the range of 4 to 7 nm. Polydispersity σ_1 and hard-sphere volume fraction η_1 were set to 0.2, initially. The amplitudes and background were selected such that the fitting curve had the same order of magnitude as that of the data. During the first few iterations R_1 and R_{HS1} were kept fixed. After the first round of iterations, reasonable values were obtained for the amplitudes and background. The final fitting was done by letting all the parameters float except α, which was held at $\alpha = 4$. The fitting process was robust and not sensitive to the initial values. We used the same procedure to fit the SAXS and SANS data corresponding to dry and hydrated samples, respectively. Figure 5.8 shows a typical fit curve and the contribution of different terms. In the Kinning-Thomas model, the peak arises from the structure factor while the form factor is responsible for the gradual decay. The exponential decay $q^{-\alpha}$ is effective only at lower q values.

5.3.1 Dry samples

The fits to the SAXS data were shown in Fig. 5.5. The results for the fit parameters R_1, R_{HS1} and η_1 are shown in Figs. 5.9 (a)-(c), respectively, where the filled blue symbols are fit parameters for the LGD samples and the open red symbols are the fit parameters for the HGD samples. As shown in Fig. 5.9 (a); the size of the fluorous domains in partially sulfonated samples of both series is smaller than that of their corresponding unsulfonated samples. It is interesting to note that samples of LGD series with the longest side chain obtained the largest fluorous domain when fully sulfonated. Unsulfonated samples in this series have a domain size around 3.5 nm, while in the HGD series, the domain sizes are around 2.8 nm. However, the size of the fluorous domains in the LGD series decreases faster upon increasing IEC, such that at IEC values of 2.2 mmol/g both series have comparable domain sizes. The smaller size of the fluorous domains in the case of partially sulfonated samples can be understood by the fact that in these samples phase separation of the fluorous segments is suppressed by the aggregation of the ionic acid groups. Later in this chapter, we will address this aspect of the phase separation in a more quantitative approach.

The hard-sphere radius (R_{HS1}) also decreases with the degree of sulfonation (and consequently IEC). In both series, unsulfonated samples with long and medium side chains have similar R_{HS1} values, which are larger than those of corresponding short samples. Among sulfonated samples, all samples of the HGD series and samples with short side chains from the other series have similar R_{HS1} values, while R_{HS1} values of the other remaining sample sets are slightly larger. Among the sulfonated samples, samples with the longest side chains of the LGD series have the largest R_{HS1}.

As shown in Fig. 5.9 (c), the hard-sphere volume fraction η_1 of unsulfonated samples is larger in the HGD series. Hard-sphere volume fraction also decreases upon sulfonation, samples of LGD series always having smaller η_1 values. This is consistent with our conjecture that these samples are less ordered; in the hard-sphere model, ordering increases with volume fraction. In the case of the LGD series, η_1 increases at higher IEC values such that samples with long and medium side chains possess the highest η_1 values among all the sulfonated samples. Our results indicate that unsulfonated and fully sulfonated samples provide the most ordered systems. We suggest that in these two cases, fluorous domains

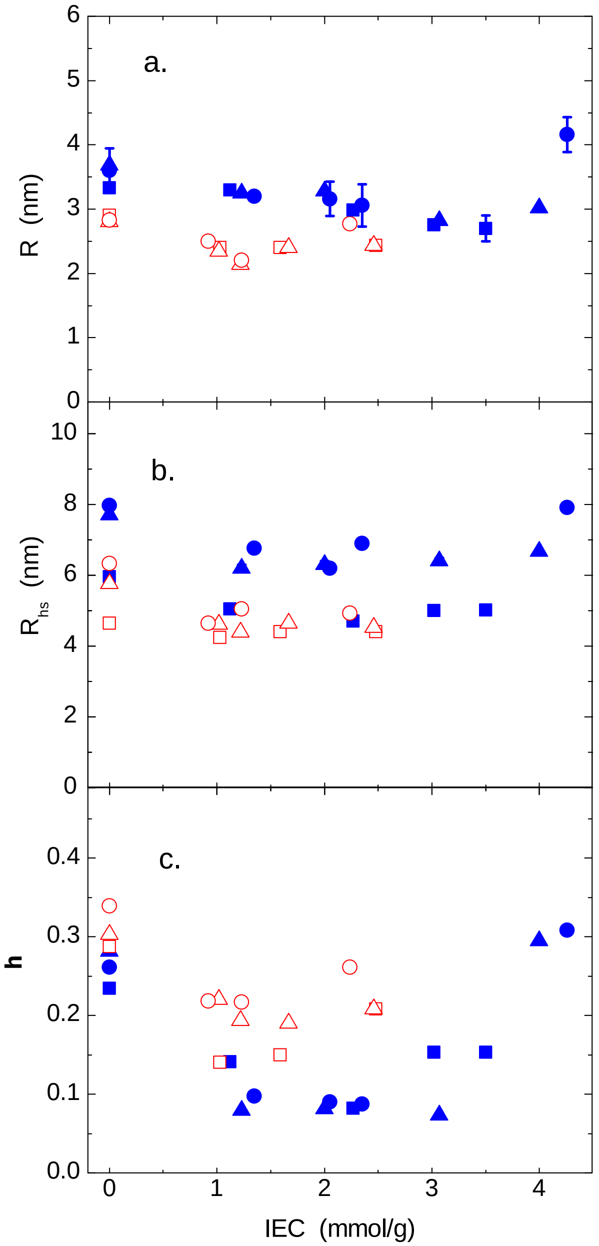

Figure 5.9: Parameters obtained from fitting the model to SAXS data, plotted as a function of IEC; (a) Radius of the fluorous core (b) hard-sphere radius, and (c) hard-sphere volume fraction. The symbols are consistent with the ones used in Table 2.1. The horizontal axis starts from the negative value to better visualize the data point corresponding to unsulfonated samples.

are embedded in a uniform continuous phase of either unsulfonated or fully sulfonated polystyrene, and therefore, the interparticle interactions can induce long-range order in the morphology. While in the case of partially sulfonated samples, the inherent random location of the acid groups along the side chains and their aggregation, along with the random nature of the morphology, perturb the interaction between them and destroy the long-range order between the fluorous domains. Similar behaviour was reported in the case of diblocks; studies by Holdcroft *et al.* indicated that sulfonation destabilizes the long order lamellar morphology in the P[(VDF-*co*-HFP)-*b*-sPS] diblock system [12, 80, 81]. Studies on partially sulfonated polystyrene-*b*-poly(ethylene-*alt*-propylene) (PS-PEP) by Gromadzki *et al.* also indicated that sulfonation leads to less ordered morphology [82].

5.3.2 Hydrated samples

This model also works for hydrated samples, as long as they maintain their mechanical integrity as solid membranes and do not become a gel upon excessive water uptake. Figure 5.6 illustrates how well this model can be fit to the SANS data of the hydrated samples. Figure 5.10 compares both R_1 and R_{HS1} of the hydrated samples of the LGD series to that of corresponding dry ones. Our results show that size of the fluorous domains R_1 does not change upon hydration. This suggests that these domains can tolerate the elastic force exerted due to the hydration of the PS matrix, and hence, can be responsible for the mechanical integrity of the membrane. As we will address later, the model breaks down when the water content of the membranes is higher than $X_{\mathrm{v}} = 0.8$. The hard-sphere radius also does not change upon hydration in the case of samples with IEC values smaller than 1.5 mmol/g. However, beyond this IEC value, R_{HS1} increases. This behaviour is consistent with the swelling of the membrane and will be discussed in the next section.

5.4 Discussion

In this section, we address the ways in which the details of architecture, such as graft number density and length of the side chains, are correlated with details of the morphology, such as spacing between fluorous domains and the overall phase separation.

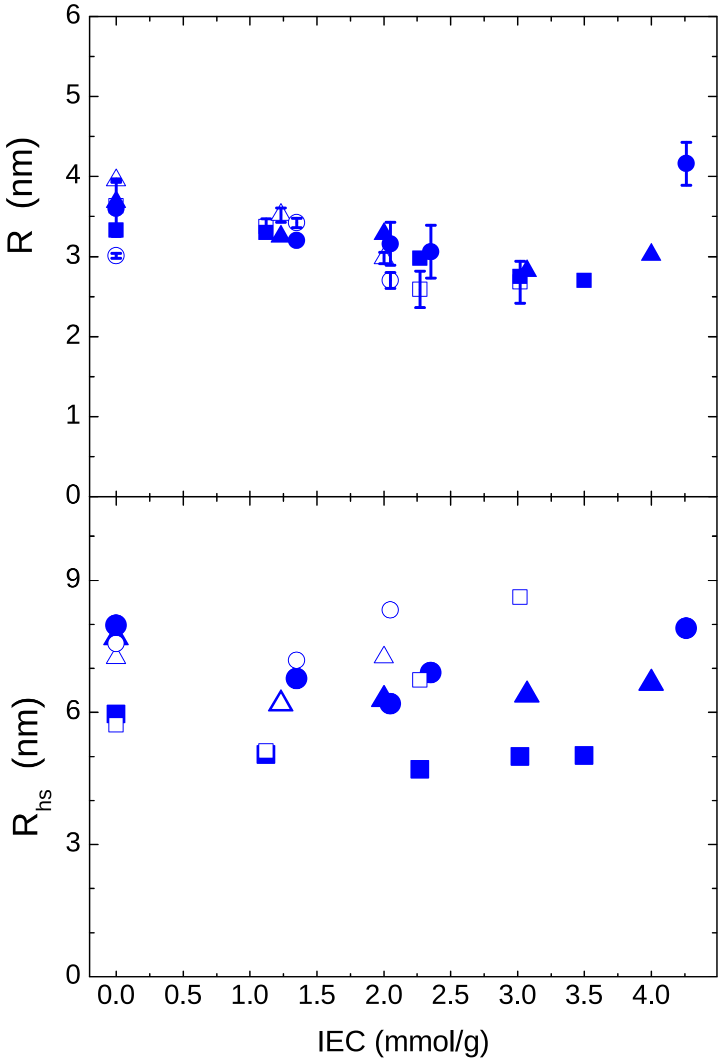

Figure 5.10: Parameters obtained from fitting the model to SANS and SAXS data for the LGD series, plotted as a function of IEC. (a) Radius of the fluorous core (b) closest approach distance. Open symbols correspond to SANS data and hydrated samples: □, △ and ○ are related to samples with short, medium and long side chains. Solid symbols are associated with the SAXS measurements and dry samples; these symbols are consistent with the ones used in Table 2.1. The horizontal axis starts from the negative value to better visualize the data point corresponding to unsulfonated samples. At higher IEC values, samples form a gel and the model no longer describes the data.

5.4.1 Fluorous domains and the PS shell

In this graft system, each fluorous domain is surrounded by its side chains. The number of side chains associated with each fluorous domain depends on the number of fluorous monomers of that domain and the graft number density. This allows us to estimate the minimum thickness of the shell corresponding to each given fluorous domain, just by considering the pendent PS side chains of a given fluorous domain. Knowing the average size of the fluorous domains, we can estimate how many fluorous monomers exist in each domain $p_{monomer}$

$$p_{monomer} = \frac{\frac{4\pi}{3}R_1^3}{V_{PVDFmonomer}} \ , \tag{5.5}$$

in which R_1 is the radius of the domain and $V_{PVDFmonomer}$ is the volume of a single fluorous monomer. The volume of any given monomer V_i can be estimated based on the polymer mass density ρ_i, and its molar mass M_i

$$V_i = \frac{M_i}{\rho_i N_A} = \frac{64(\mathrm{gr/mol})}{1.8(\mathrm{gr/cm^3}) \times 6.02 \times 10^{23}} \times 10^{21}(\mathrm{nm^3/cm^3}) = 0.059\ \mathrm{nm^3} \ , \tag{5.6}$$

where, N_A is the Avogadro number. It is also possible to calculate the number of side chains attached to each domain N_s and the number density per surface area of the fluorous domain n_H

$$\begin{aligned} N_s &= p_{monomer} \times GD \ , & (5.7) \\ n_H &= \frac{N_s}{4\pi R_1^2} \ . & (5.8) \end{aligned}$$

In the LGD series, $p_{monomer}$ is estimated to be ~ 3400 monomers for unsulfonated samples having medium and long side chains, while it is roughly equal to 2500 for unsulfonated sample with short side chains, while the number of monomers per backbone is approximately 1800. One can conclude that each domain consists of more than one backbone. In the HGD series, the number of monomers per domain $p_{monomer}$ is estimated to be ~ 1500 monomers, which is close to $\frac{1}{3}$ of the number in the corresponding backbone chain. The densities of the side chain per surface area of the flourous domains n_H for unsulfonated samples of the LGD and HGD series are estimated to be 0.34 and 0.4 $\mathrm{nm^{-2}}$, respectively.

Having defined the above mentioned parameters, we can analyse the shell attached to the fluorous domains. Our approach is to first estimate both the minimum and maximum values of the shell thickness, by assuming that the shell only consists of PS chains corresponding to the given fluorous domain size. Then, we will compare the experimental values of the shell thickness to the minimum and maximum values. If the experimental values do not satisfy the minimum and maximum conditions, we can conclude that our assumption is not precise *i.e.* the shell is not pure PS.

We can determine the minimum shell thickness by assuming a dense PS shell around the fluorous core. Since we know how many side chains are attached to each fluorous domain, we can approximate the PS volume associated with each fluorous domain

$$V_{shell} = n \times N_s \times V_{PSmonomer} \ , \tag{5.9}$$

in which n is the length of the side chain, N_s is the average number of side chains attached to the fluorous domain and $V_{PSmonomer} = 0.167$ nm^3 and is estimated based on Eq. 5.6. The thickness of this PS shell t is given by

$$t = \left(\frac{3(V_{shell} + V_{domain})}{4\pi} \right)^{\frac{1}{3}} - R_1 \ , \tag{5.10}$$

in which $V_{domain} = \frac{4\pi}{3} R_1^3$ and is the volume of the fluorous domain.

The other scenario is based on calculating the radius of gyration R_g of the PS side chain, which gives us an upper limit of the thickness corresponding to that given polymer chain [83]. The radius of gyration for PS chains in a good solvent can be calculated using [84]

$$R_g = 1.2 \times 10^{-2} (n M_{PS})^{0.6} \ \text{nm}, \tag{5.11}$$

where n is the polymerization degree. In this case we assume that the PS chains form a Gaussian conformation and are independent of each other, while attached to the surface of the fluorous domain.

The experimental value for the domain spacing is equal to $R_{HS} - R_1$. Figure 5.11 (a) and (b) compare the experimental thickness of the shell of the unsulfonated samples to the calculated values of t and R_g, respectively. In the case of the HGD series, the experimental values of $R_{HS} - R_1$ lie between the values obtained for the two scenarios *i.e.* $R_g > R_{HS} - R_1 > t$. On the other hand, for the LGD series, these experimental values are higher than both of the estimated values *i.e.* $R_{HS} - R_1 > R_g$ and t.

If all of the backbone segments participate in the phase separation, we would expect

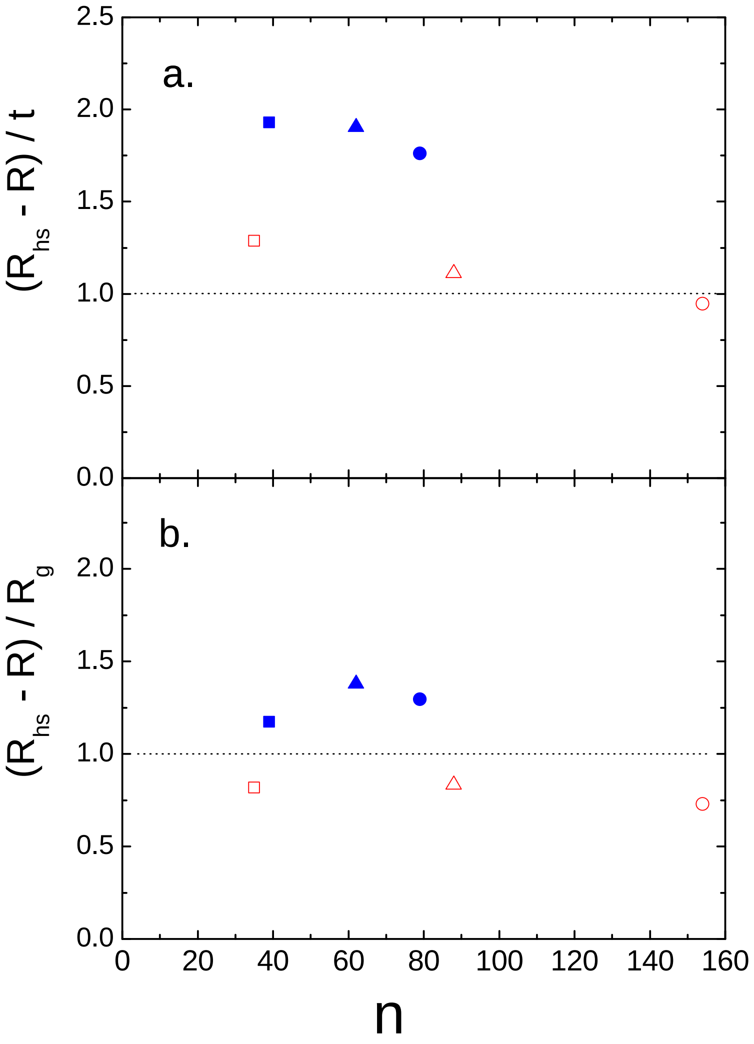

Figure 5.11: Thickness of the shell as obtained by dividing the experimental data by estimates based on two different scenarios, as described in the text and assuming a pure PS shell. Blue-solid and red-open data sets belong to unsulfonated samples of the LGD and HGD, respectively. The horizontal axis is the length of the side chains. Note that the size of the fluorous domains for each given length of side chain is different.

that the thickness of the shell would be the same as t, based on the assumption that the shell only consists of PS. But all of the backbone segments do not necessarily participate in forming fluorous domains, hence, the unsegregated fluorous fraction and its corresponding PS chains could also contribute to the shell, as shown in Fig. 5.7 (c). In this case, $R_{HS} - R_1$ would be bigger than t. This condition is satisfied in both series, however, $R_{HS} - R_1$ values obtained for the LGD series are almost twice as large as t (6.15 (a)). On the other hand, the thickness of the shell for samples of the HGD series is smaller than t and larger than R_g, consistent with diblock studies. Therefore, we conclude that these samples have the most improved phase separation and the PS shells in these samples mostly contains of PS segments, especially for the sample with the long side chains. We used this approach to investigate the shell thickness of the unsulfonated samples. In the next section, we quantitatively analyse the phase separation of both unsulfonated and sulfonated samples, with the focus being on sulfonated samples.

5.4.2 Phase separation

As mentioned previously, the existence of a second order peak in the SAXS intensities of unsulfonated and fully sulfonated samples indicates that these samples have more developed and ordered morphologies, compared to the partially sulfonated samples. In the case of sulfonated samples, phase separation is determined by two contributions: the segregation of fluorous segments and the aggregation of ionic domains. In the partially sulfonated samples, the phase separation is defined by three component and the randomness of locations of the acid groups along the side chains will affect the overall order in the system. For fully sulfonated samples, this randomness disappears as all of the PS segments are sulfonated and phase separation is between two component again. To quantify the degree of phase separation, we estimate how much of the fluorous backbone participates in phase separation.

We define a parameter Ω as the ratio of volume of the fluorous domains in the sample to the total volume of fluorous backbone available ϕ_{PVDF}. The volume of the fluorous domains is equal to the average volume of one domain times the domain number density: $\frac{4\pi}{3}R_1^3 \times n_D$, where the domain number density depends on the volume fraction of the hard-sphere η_1 and R_{HS1}, as expressed in Eq. 5.2. Therefore, Ω is

$$\Omega = \frac{\frac{4\pi}{3}R_1^3 \times n_D}{\phi_{\mathrm{PVDF}}} \ , \tag{5.12}$$

in which volume fraction of the fluorous segments in the sample ϕ_{PVDF} is calculated based on the degree of sulfonation, as discussed in Chapter 2. For the case of fully phase separated backbones, this ratio would be equal to 1. Figure 5.12 shows the values obtained for the two series as a function of the volume-based ion content IEC_{v}. All of the unsulfonated samples in the LGD series have the same level of phase separation, while for the HGD series, phase separation of unsulfonated samples is improved by increasing the length of the side chain, with the longest side chains sample being characterized by significant phase separation. The second case is consistent with the phase separation of conventional copolymers, in which phase separation depends on χN. We believe that in the first case crystallinity hinders the phase separation. This behaviour has been reported in several other crystalline copolymers [27]. In fact, the formation of the crystalline domains induces kinetically trapped domains in the system and the polymer may never reach the equilibrium state [27]. Our results show that partially sulfonated samples have a smaller degree of phase separation compared to the corresponding unsulfonated or fully sulfonated samples, the only exception being samples with long side chains of the HGD series. To the best of our knowledge, no other groups have studied the morphology of the fluorous domains in such a system using SAXS measurements. Moreover, this is the first time that the effect of sulfonation on phase separation of these ionic-graft copolymers has been analysed quantitatively. Generally, our results suggest that phase behaviour in samples with long side chains and a low degree of crsytallinity (samples of the HGD series) are similar to that of conventional copolymers. But the other two sets of samples in this series show unusual phase behaviours in that their degrees of phase separation decrease upon sulfonation. Phase separation of samples of the LGD series, on the other hand, is dictated by crystallinity and, hence, all of these samples follow a similar trend in terms of the degree of phase separation as a function of volume-based ion content. We hope that these results shed light on the phase separation of the ionic copolymer systems, in general, and on the phase separation of ionic random graft copolymers in particular.

5.4.3 Water absorption at nano-scale level

In this section, we study two aspects of the water absorption related to the morphology: the existence of water in the vicinity of the fluorous domains as seen by analysing the hard-sphere radius, and also by analysing the effect of the water on the average spacing between the domains. Figure 5.10 shows that the size of the fluorous domains is not affected by hydration, however, the hard-sphere radius of the samples increases upon hydration for samples with $IEC > 1.5$ mmol/g. We suspect that water penetrate in to the shell and the hard-sphere swell as the water content increases. Is the increase in the hard-sphere volume consistent with the swelling of the sample? We can compare the increase in hard-sphere volume to the overall swelling of the membrane by comparing the hard-sphere volume of the hydrated V_{HS}^{wet} and dry V_{HS}^{dry} samples assuming uniform swelling. The expected V_{HS}^{wet} value upon water content X_{v} is given by

$$V_{HS}^{wet} = \frac{V_{HS}^{dry}}{1 - X_{\mathrm{v}}} , \tag{5.13}$$

in which $V_{HS}^{dry} = \frac{4\pi}{3} R_{HS1}^3$ is obtained based on SAXS measurements of the dry samples. The hard-sphere volume of the hydrated samples V_{HS}^{wet} can be calculated directly from SANS measurements of hydrated samples. Figure 5.13 shows the values obtained based on these two different approaches as a function of water content. The fact that these two values agree indicates that the PS shell around the fluorous domain swells the same as the rest of the sPS/PS matrix. We conclude that hydrated sPS/PS matrix swell homogeneously even in the vicinity of the fluorous domains.

We can also determine the correlation between the swelling properties of the membrane and volume increase at the nano-scale level, based on the average spacing between the domains. Let V_p^{dry} be the volume of the membrane per fluorous domain, as obtained based on SAXS measurements. We can estimate the effect of water content on this parameter by assuming that the number of fluorous domains remains the same upon hydration

$$V_p^{wet} = \frac{V_p^{dry}}{1 - X_{\mathrm{v}}} , \tag{5.14}$$

in which V_p^{wet} is the expected volume of membrane per fluorous domain after hydration. This parameter can also be obtained directly based on SANS measurements on hydrated membranes. Figure 5.14 compares the values obtained for V_p^{wet} from both methods as a function of water content. The calculated values are in a good agreement with the experimental values except for the sample with $X_{\mathrm{v}} = 0.8$. These results suggest that, generally, swelling of the membrane is homogeneous at both nano-scale and micron-scale. Two possible scenarios might have happened in the case of the sample with $X_{\mathrm{v}} = 0.8$: the total number of fluorous domains decreased upon sulfonation and/or water starts to form

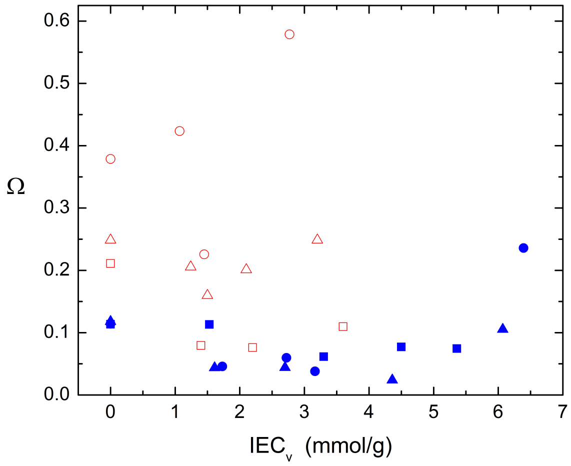

Figure 5.12: Ω, volume fraction of the backbone contributed in forming fluorous domains, is calculated based on Eq. 5.12. Higher Ω values indicate better phase separation. For each given series, samples with higher IEC_v values have the highest Ω value. Our results indicate that samples with higher graft number densities develop better phase separation.

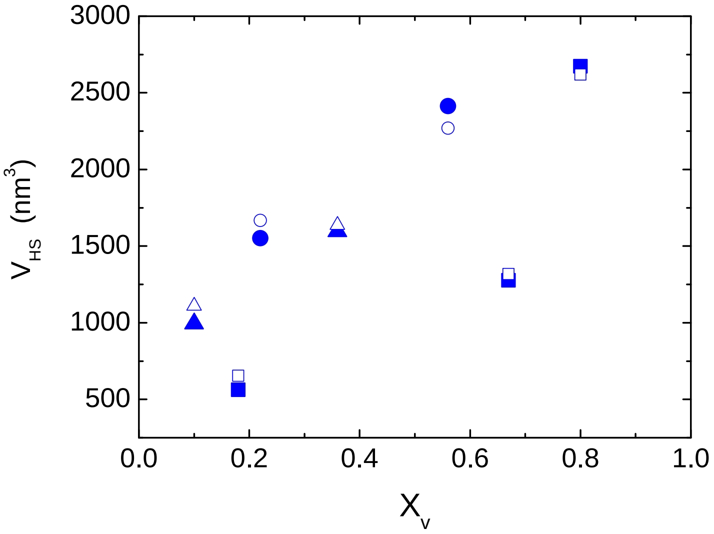

Figure 5.13: Hard-sphere volume for fluorous domains as obtained directly from SANS measurements of hydrated samples V_{p1HS}^{wet} (solid symbols) compared with that of calculated values based V_{p1HS}^{dry} from SAXS measurements and water content values X_v.

rather large water domains and the membrane possesses non-homogeneous swelling. But since the water content in the vicinity of the domains agrees with bulk properties, the first scenario is more probable.

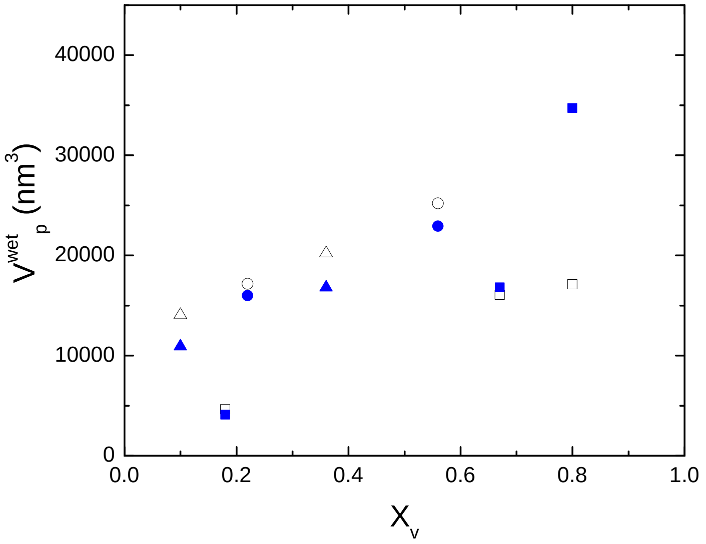

Figure 5.14: V_p, volume of membrane per particle, as obtained based on fitting the model to the hydrated samples (■,▲, ●) and as calculated based on V_p of dry sample and water content values (□,△, ○). Symbols (■,▲, ●) represent samples with low graft number densities and side chain lengths of short, medium and long, respectively. The corresponding calculated values (□,△, ○) are obtained based on Eq. 5.14.

5.4.4 Water content, crystallinity and phase separation

Our results show that the morphology of fluorous domains of the studied system can be described by randomly located polydisperse spheres. However, details of this morphology, such as size and spacing between domains, depend on the graft number density and length of the side chains. Also, we notice that crystallinity hinders the phase separation. The question is whether these differences are correlated to bulk properties such as water content properties.

In Chapter 2 we discussed the water content properties based on mass-based *IEC* values. Since the volume ratios are more relevant to morphological studies, in the following discussion we will concentrate on the water content values expressed as a function of volume-based ion content IEC_{v}. In this representation, if we categorize samples based on the length of their side chains, we see two different behaviours. As shown in Fig. 5.15 (a), all the samples with side chains longer than 78 have similar water content properties. Among these sample sets, the ones with a side chain length of $n = 79$ have the lowest graft number density and a significant degree of crystallinity, while the other two sets have very low degree of crystallinities. These sample sets all have relatively low fluorous ratios, namely lower that 25 vol%, therefore, we conclude that at these low fluorous volume ratios, details of the architecture and morphology are irrelevant to water content properties. However, it does not mean that the fluorous volume ratio is quite irrelevant to water absorption of the samples; all of these samples start to make a gel upon hydration at higher degrees of sulfonation, meaning that there exists a maximum degree of sulfonation beyond which the membrane losses its mechanical integrity upon hydration. This maximum value seems to be positively correlated to the fluorous ratio; for samples containing 8, 14 and 22 vol% fluorous ratios, the maximum degrees of sulfonation are around 33, 41 and 48%, while membranes with a higher fluorous content can accommodate more charge before starting to swell uncontrollable.

Sample containing fluorous ratios higher than 25 vol% show different water content behaviours, as shown in Fig. 5.15, suggesting that water content is affected by other factors such as crystallinity, the length of the side chain and/or the fluorous ratio. Among these three sample sets, partially crystalline samples with the medium side chain have the lowest water content in low IEC_{v} range (< 3 mmol/cm^3). As IEC_{v} values increase, the water content of these samples exceeds that of samples with short side chains. Samples with medium side chains has the lowest fluorous ratio among these three sample sets, which indicates that the total fluorous ratio can have a significant role only at higher IEC_{v} values. The other factor that we can consider is the degree of backbone phase separation. Among these three sets of samples, the samples with the medium side chains have the lowest degrees of phase separation. This can explain lower water content in the moderate IEC_{v} range.

The most interesting samples are those with short side chains. These two sets of samples have very similar fluorous ratios and lengths of the side chains. In addition, their degrees of phase separation are comparable, as shown in Fig. 5.12. However, crystalline samples have a lower water content in the studied IEC_{v} range. Therefore, we suggest that crystallinity plays an important role in the water content when the fluorous ratio is not very low (~ 30 vol%).

Table 5.1: We suggest that in the case of the samples with side chains shorter than 65 monomers, longer lengths of the side chains and a higher degree of crystallinity lead to lower water content values of the membrane when the membrane has a moderate IEC_{v} values *i.e.* IEC_{v} range of 1.5-3.5 mmol/cm^3. However, beyond this IEC_{v} value, the factors that affect water content include the fluorous volume ratio and degree of crystallinity.

Factors affecting water content	IEC_{v} range
1. Length of the side chains 2. Crystallinity	1.5-3.5
1. Fluorous ratio 2. Crystallinity	> 3.5

Table 5.1 summarizes the suggested idea for the samples with side chains shorter than 65 and indicates which factors lead to less water uptake values of the membrane in different ranges of IEC_v.

5.5 Summary

We have quantitatively characterized the morphology of fluorous domains in the studied ionic graft system. The Kinning-Thomas model was successfully applied to interpret SAXS and SANS data. Our results indicate that the fluorous backbones form quasi-spherical fluorous domains. We suggested that the size of the domains in unsulfonated samples depends on the graft number density. Partially sulfonated samples have the smallest domain sizes. We believe that in partially sulfonated samples, the segregation of fluorous monomers is suppressed by the aggregation of the ionic acid groups. Moreover, our results suggest that samples of the HGD series develop a better phase separation. This was examined by comparing the shell thickness to the R_g values of side chains and also the expected shell thickness calculated based on a dense PS shell. Furthermore, we estimated the degree of phase separation by comparing the total PVDF available in the sample with the overall fluorous domain volume, obtained based on the number density of the domains and their average radius. The poor phase separation of the samples of the LGD series was attributed to their significant degree of crystallinity.

We studied the swelling properties of these samples at the nano-scale level and noticed that the swelling properties at this length scale are consistent with the bulk properties.

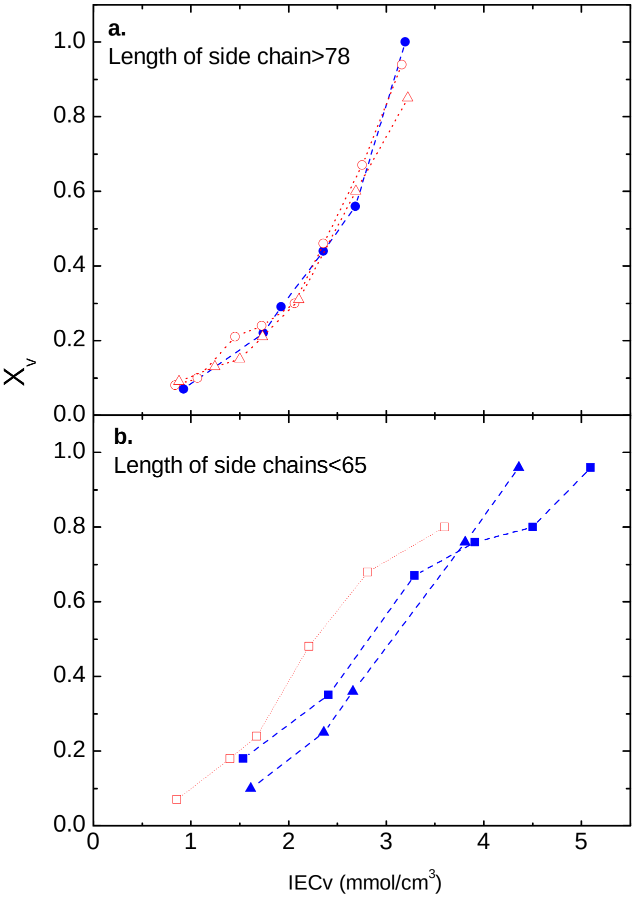

Figure 5.15: Water content of ionic graft copolymers plotted as a function of IEC_{v}. (a) Contains data corresponding to samples with same water content properties. These samples have side chains longer than $n = 78$. (b) Samples with shorter side chains that have different water content properties. We associate these differences to properties such as length of the side chains and degree of crystallinity. More details are included in Table 5.1. The symbols correspond to those introduced in Table 2.1. Data taken from [1, 22].

Moreover, our results indicate that swelling properties are homogeneous in these membranes and water exists even in the vicinity of the fluorous domains, as long as water content is less than 0.8. We concluded that water content of samples with longer side chains (> 79) is independent of the details of micro-structure and other factors such as the degree of crystallinity and phase separation. On the other hand, for samples with side chains shorter than 69, the degree of phase separation and crystallinity can suppress the amount of the water in the membrane.

Chapter 6

Water-rich domains

6.1 Introduction

In this chapter, we focus on the hydrated samples. The level of hydration depends on the *IEC* of the polymer [1]. In the presence of the water, the acid groups tend to aggregate and form clusters to minimize the free energy of the system. The swelling properties are determined by the balance between the electrostatic forces, the osmotic pressure of the counterions and the elastic deformation of the polymer chains [11, 17, 85]. A detailed understanding of water management and formation of water nano-domains in the membrane is crucial in designing new PEM materials because this knowledge helps us to assess the trade-offs between mechanical and transport properties of the membrane [7, 11, 86]. An extensive amount of research has been conducted during the last few decades to investigate the morphology of PEMs and to find out what factors are involved in formation of different phases [5, 7, 9, 10, 11, 18, 64, 87, 88]. In the next section, we will summarize some of the morphological models that have been proposed for the morphology of PEM materials and will address the challenges involved in interpreting the characteristic features in the scattering data. We mainly focus on models proposed for PEMs possessing random morphologies rather than those with lamellar or hexagonal structures. Nafion is one of these PEMs. In the subsequent section, I present our SANS results of the [P(VDF-*co*-CTFE)-*g*-sPS] systems. A morphological model was fit to this data and we were able to characterize the water-rich domains in the samples. Finally, I will discuss the consistency of the model and show how the details of morphology are correlated to conductivity.

6.2 Morphological models

Morphological models for PEMs are inspired by TEM images or scattering data and are quantitatively examined by SAXS and/or SANS measurements. The characteristic parameters obtained based on the models should be consistent with membrane properties such as volume ratios of different phases and swelling properties [15, 17, 18]. The general framework for these studies is to propose a morphological model that is able to predict the scattering intensities in a wide q range and is also able to determine the origin of the scattering features.

We start this section with a description of Nafion, which is the benchmark material in this field, and then introduce some other models used for different ionomers.

6.2.1 Models with spherical symmetry for Nafion

Nafion has a complicated morphology and different models have been used to interpret its scattering features. The different morphological models can be classified into five categories: models with spherical symmetry, models based on layered structure, rod-like structure, network structure and parallel nano-channels. Network structure and parallel nano-channels morphologies have been examined by simulation methods and are beyond the scope of this study [18, 64].

Models assuming spherical domains are the simplest models for Nafion. In most of these models [51, 60, 78], it is assumed that spherical domains are connected by nano-tubes of water, although the intensity profile does not take the nano-channels into account. The scattering intensities can be expressed as a product of two terms. The first term, the form factor $F(q)$, describes the intra-particle scattering and is due to the shape of the particles. The second term, structure factor $S(q)$, is due to interference of the scattered beams from different scattering particles and depends on spatial distribution and spacing between those particle. Therefore, the scattering intensities can be written as

$$I(q) = \frac{(\Delta\rho)^2}{V_p} F(q) S(q) \ , \tag{6.1}$$

where V_p is the average volume per aggregate and $\Delta\rho$ is factor that depends on the contrast between different phases. As mentioned in Chapter 3, the contrast in SAXS and SANS depends on electron density and SLD values, respectively. Early SANS and

SAXS measurements of Nafion showed two characteristic features: a broad peak located at $q = 0.12\ \AA^{-1}$, known as the ionomer peak, and an upturn at smaller q values, as shown in Fig. 6.1. The spherical models mainly focus on the characteristic peak, rather than the upturn at lower q.

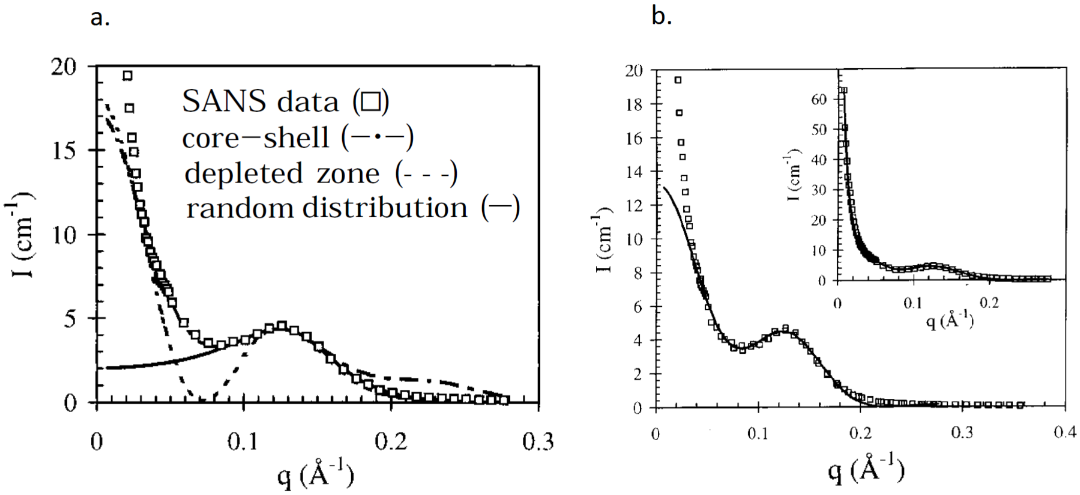

Figure 6.1: Typical SANS data of Nafion showing the characteritic peak located at $q = 0.12\ \AA^{-1}$ and the upturn at low q. (a) 3 different spherical models were fit to the SANS data, all of these models were rejected by Gebel and Lambard [60] whose local order model provides a good fit to the data except at lower q values, as shown in (b), the inset shows how including Debye-Buech model improves the fit at lower q values. From [60], used with permission.

Randomly distributed spheres

Gierke *et al.* [60] proposed a model, consisting of randomly-distributed spheres, to explain the characteristic peak in the SAXS data of Nafion. They noticed that the position of the characteristic peak moved to lower q values upon hydration [60]. They associated this behaviour with swelling of the spherical ion-rich domains. As shown in Fig. 6.1 (a), this model fails to predict the scattering intensities at lower q values ($< 0.1\ \AA^{-1}$).

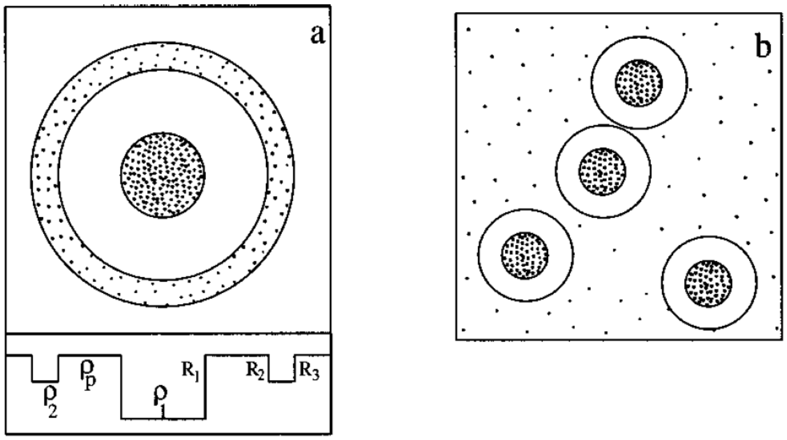

Figure 6.2: Schematics of (a) core shell model and (b) depleted zone core-shell. In the core-shell model ionic cluster full of water have a radius of R_1, each domain is surrounded by a fist and second shell of radii of R_2 and R_3. The ρ values of different shell is not the same, as shown in the bottom of (a). In the depleted zone core-shell model the radius of the outer shell is infinite. From [60], used with permission.

Core-shell model

In the core-shell model [50], ionic clusters full of water are surrounded by a first shell, rich in fluorocarbon chains, and a second shell, containing a relatively low density of ionic groups, as shown in Fig. 6.2 (a). This model also failed to predict the scattering intensities at q values smaller than 0.1 $\AA^{-1}$ [15], as shown in Fig. 6.1 (a).

Depleted zone core shell model

The depleted zone core shell model [50] is basically a core-shell model in which the outer radius of the shell is infinite and is shown in Fig. 6.2 (b). For Nafion, this model works better at lower q values, as low as $q = 0.03\ \AA^{-1}$, but it is not able to produce the scattering intensities at higher q values ($>\sim 0.2\AA^{-1}$), as shown in Fig. 6.1 (a). Moreover, the predicted water absorption based on this model is not consistent with experimental values.

Local order model

Gebel and Lambard [15] developed an improved model capable of predicting the scattering intensities over a wider q range. They still assumed a spherical domains but considered a combination of short-range and long-range order. At short range the four nearest neighbours of a given ionic aggregate were assumed to be located at a well-defined distance D. At long range, the aggregates have liquid-like order. As shown in Fig. 6.1 (b), this model provides a reasonable fit curve in the q range of 0.04 to 0.28 $\mathring{A}^{-1}$.

In order to fit the scattering data over the entire q range, they included the Debye-Buech model to compensate for the upturn at low q range. The Debye-Bueche model [41] describes a two phase system with one characteristic correlation length ξ. It assumes that beyond this length, the spatial correlation vanishes and predicts the scattering intensities to be [41]

$$I(q) = \frac{A_{DB}\xi^3}{(q^2\xi^2+1)^2} \ , \tag{6.2}$$

in which A_{DB} is the scaling amplitude, which depends on the difference between the electron densities of two phases and the volume fraction of each phase. Gebel and Lambard suggested that the upturn at low q values originated from the density fluctuations in the samples. The correlation length corresponding to these fluctuations was determined to be $\xi = 80\ \mathring{A}$. The results are shown in the inset to Fig. 6.1 (b). Among the spherical models of Nafion, the local order model is the most accepted one due to its excellent agreement with experimental data.

6.2.2 Polymer bundles or rod-like structure

Rubatat *et al.* [17] carried out SANS measurements in order to discriminate which part of the SANS spectra was more sensitive to dilutions. They obtained samples with a high water content by boiling the membranes in a pressure vessel for 12 hours at different temperatures, as proposed by Gebel [16]. Figure 6.3 (a) shows the SANS intensities of the hydrated Nafion membranes. Rubatat *et al.* [17] noticed that SANS intensities of membranes with different swelling properties were generally similar, hence, they assumed a simple dilution process for the swelling of Nafion. This study showed that SANS intensities in the middle q range were not affected by water content, while the upturn at ultra small angles and asymptotic behaviour at larger angles were sensitive to the swelling degree of the membrane. They plotted the Bragg d-spacing, corresponded to the ionomer peak position, versus polymer volume fraction ϕ_P, as shown in Fig. 6.4. They also included the Bragg d-spacing corresponding to the matrix knee and observed two different behaviours corresponding to samples with volume ratios below or above $\phi_P = 60\%$. Although these characteristic features correspond to quite different length scales, as shown in Fig. 6.4, the two d-spacings are correlated, meaning that they follow the same dilution law. Therefore, Rubatat *et al.* suggested that the swelling process is a simple dilution process. Since samples containing $\phi_P > 60\%$ were obtained at temperatures higher than T_g of Nafion, they attributed the existence of the two regions to the different equilibrium conditions obtained below or above T_g.

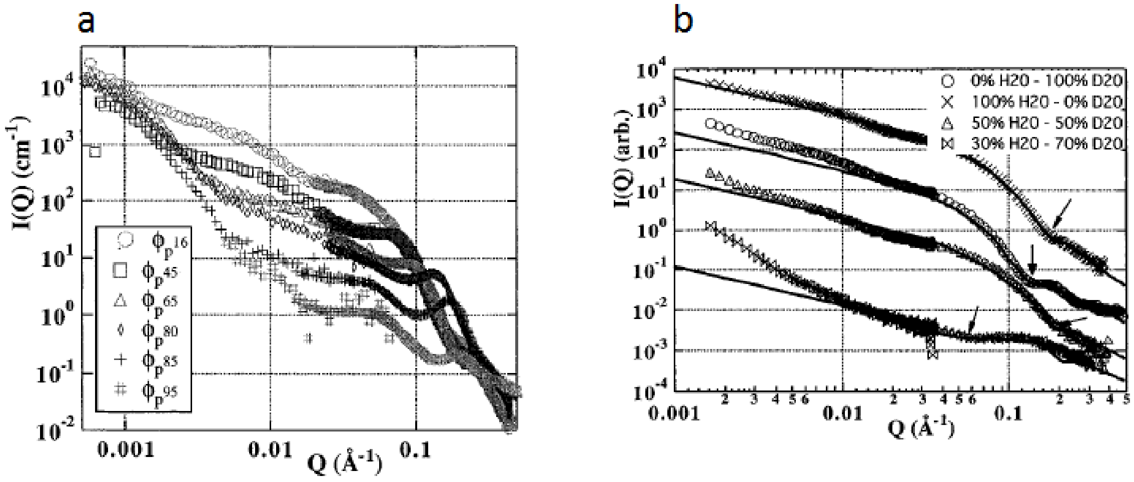

Figure 6.3: (a) SANS profiles corresponding to Nafion membranes possessing different polymer volume fractions, (b) SANS intensities corresponding to samples $\phi_P = 16\%$ swollen in different solvents [17]. From [17], used with permission.

In order to determine the origin of the scattering features, they used the contrast matching technique. Figure 6.3 (b) shows the scattering data corresponding to Nafion membranes soaked in four different solvents. Rubatat *et al.* were able to interpret these results by proposing a three phase system. In fact, they could distinguish if the morphology was that of clusters of water in a polymer matrix or clusters of polymer covered by the solvent's molecules. The proposed model was a shell-cylinder configuration: a polymeric core surrounded by a shell which had a high density of counter ions and was covered by solvent molecules. Their results indicated that Nafion chains in a hydrated state form polymeric bundles with a diameter of $\sim$ 4 nm and a length of 100 nm. Other advanced models of Nafion, such as parallel nano-channels, benefited from the ideas discussed in this model [18].

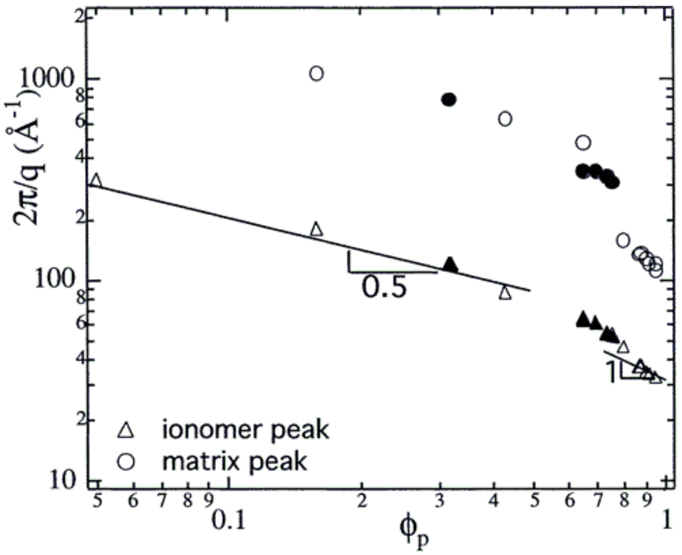

Figure 6.4: Bragg d-spacings corresponding to ionomer peak position and the matrix knee plotted as a function of polymer volume fraction ϕ_P. d-spacings corresponding to these to features are correlated. Below $\phi_P = 0.6$ the slope is 0.5, while above $\phi_P = 0.6$ the slope is close to 1. [17]. From [17], used with permission.

6.2.3 Teubner-Strey model

This model describes a binary system in which one phase forms domains with poorly-defined shapes [89]. This morphology is determined by only two characteristic lengths: domain spacing d_{TS} and a correlation length corresponding to the size of the domain ξ_{TS}. Generally, the scattering function predicted by this model starts with a plateau at the limit of smaller q values, followed by a characteristic peak, and at higher q a q^{-4} decay [89]. A few groups have applied this model to find the origin of the characteristic features in the scattering intensities of PEM materials [72, 90, 91].

Serpico *et al.* [91] used this model to interpret SANS data of sulfonated styrene-ethylene copolymer membranes. The volume ratio of PS was varied from 30 to 75 wt% and the degree of sulfonation from 36 to 45 mol%. They performed SANS measurements on hydrated membranes at two temperatures: 25 and 60° C. Table 6.1 includes their results. This study indicates that the ratio of the domain spacing to the size of the domains d_{TS}/ξ_{TS} increases with temperature. Serpico *et al.* concluded that at higher temperatures the system

Table 6.1: Fit parameters based on the Teubner-Strey model for sulfonated styrene-ethylene copolymer membranes as reported by Serpico *et al.* [91][request the permission].

Temp ($^\circ C$)	d_{TS} (nm)	ξ_{TS} (nm)	d_{TS}/ξ_{TS}
25	7.1	3.8	1.9
60	8.5	3.5	2.4

Table 6.2: Fit parameters based on the Teubner-Strey model. Data for membranes of comb-like copolymers investigated by Nieh *et al.* [72][Permission required].

IEC mmol/gr	d_{TS} (nm)	ξ_{TS} (nm)	d_{TS}/ξ_{TS}
0.87	2.5	1.5	1.7
1.6	3.0	1.2	2.5

becomes more disordered.

As mentioned in the previous chapter, Nieh *et al.* [72] also used this model to describe the morphology of their PEMs based on SANS measurements on hydrated membranes. Their results indicate that by increasing IEC values, the correlation length ξ_{TS} decrease but their average spacing d_{TS} and the ratio d_{TS}/ξ_{TS} increases (Table 6.2). Since d_{TS}/ξ_{TS} increases upon sulfonation, they concluded that the origin of the characteristic peak in the scattering data was the side-chain-rich regions embedded in the nano-size water channels, as shown in Fig. 6.5.

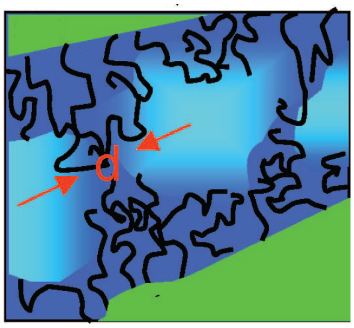

Figure 6.5: The morphology of water-rich domains suggested by Nieh *et al.* [72] The green color represents the hydrophobic domains, solid lines stand for sulfonated PS chains and blue color represents the water-rich domains. In this figure d is the same as d_{TS}, defined in the text; we used the subscript in the text for clarity. From [72], used with permission.

6.2.4 Kinning-Thomas model

The other model that has been widely used to interpret the scattering features of ionomers is the Kinning-Thomas model. In the previous chapter, we applied this model to SAXS and SANS data in order to characterise the fluorous domains. Both monodisperse [24, 92] and polydisperse [90, 93] versions of this model have been used to interpret the SAXS and SANS scattering from ionomers.

Balog *et al.* [24] used the monodisperse version of this model to investigate the morphology of ion-rich domains in ethylene tetrafluoroethylene-g-poly[sulfonated styrene-co-divinylbenzene] (ETFE-g-poly[sPS-co-DVB]). The membranes were immersed in a CsCl solution to exchange protons with Cs and enhance the X-ray scattering from ion-rich domains. They examined the effect of cross-linking the DVB on the aggregation of the acid groups. Using this model, they were able to interpret the characteristic peak in the SAXS intensities of the dry membranes. They discovered that the size and number density of the ion-rich domains decreases with cross-link level, while the spacing between the domains is proportional to the cross-link level. They showed that the membrane proton conductivity of the hydrated membrane is strongly correlated with the structure of ion-rich domains of the dry membranes. By estimating the average number of water molecules in each domain N_{H_2O}, they were able to show that the conductivity increases linearly as a function of $\frac{N_{H_2O}R_2}{r_0}$, where, R_2 and r_0 are the average size of and spacing between the ion-rich domains.

In a similar study, Yoonesi *et al.* [90, 93] employed the polydisperse version of the model to explain the SANS data of sulfonated polyarylenethioethersulfone (SPTES), a random copolymer. The morphology of hydrated samples was investigated by SANS measurements. They studied the morphology of the samples at two different temperatures, 25 and 55°. Two different morphologies were reported for the aggregation of the ionic groups as they varied the sulfonation degree and temperature: polydisperse spherical domains containing water molecules with liquid-like ordering (Kinning-Thomas model), and large scale water pockets (Teubner-Strey model). The Kinning-Thomas model was suitable to fit all of the SANS data taken at the lower temperature of 25° C. However, at 55° C this model worked only for samples with degrees of sulfonation smaller than 55%. They suggested that the morphology of the samples with higher degrees of sulfonation evolves to a bi-continuous morphology and, hence, used the Teubner-Strey model to characterise the scattering intensities. They observed that, by increasing the degree of sulfonation, the radius of the water-rich domains

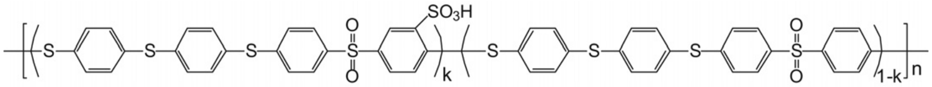

Figure 6.6: Chemical structure of sulfonated polyarylenethioethersulfone (SPTES). From [90, 93], used with permission.

and their volume packing density increase. Therefore they concluded that water-rich domains can hold more water molecules, in the presence of more sulfonic acid groups. According to their results, the size of the water-rich domains increases from 1.3 to 1.7 nm^{-1} as the degree of sulfonation increases from 45 to 71%.

Seitz *et al.* also used the Kinning-Thomas model to investigate the morphology of linear poly(ethylene-co-acrylic acid) zinc-neutralized ionomers. In addition to differential scanning calorimetry (DSC) and scanning transmission electron microscopy (STEM), they performed SAXS measurements to understand the morphology of the membranes. In this study, the size of the ionic aggregates was measured to be around 0.5 nm, independent of the ion content, while the hard-sphere radius and the number density of the domains were strongly affected by the ion content. They emphasized that this model provides an excellent method to analyse the scattering patterns of ionomers.

In a rather different study, Hall *et al.* [94] performed coarse-grained molecular dynamics simulations to investigate the morphology of ionomer melts of different polymer architectures. Based on their simulations, they were able to analyse the expected features of the scattering data. Their results suggested that the Kinning-Thomas model is a proper model to study the ionic aggregates of ionomers and it provides good approximations for the actual aggregate number density, core size, and interaggregate length [94].

Zhou *et al.* [92] studied a series of poly(styrene- styrenesulfonate) ($\mathrm{P(S\text{-}SS_x)}$) membranes. Morphology of both solvent-cast and spin-cast membranes was examined by SAXS and scanning transmission electron microscopy (STEM). Their results confirmed that the values obtained for the size of the ionic aggregates and the sample volume per domain, as obtained by the Kinning-Thomas model, are consistent with values that were obtained based on STEM [92]. In their work, they used the monodisperse version of the model.

In this thesis, we also use a monodisperse version of the Kinning-Thomas model to interpret the characteristic peak located at high q values. We will provide evidence that this peak originates from the scattering of water-rich domains. All analysis is based on

SANS data of hydrated samples.

6.3 SANS measurements

Figures 6.7 (a)-(f) show the SANS data of the sulfonated samples soaked in D_2O. Data corresponding to unsulfonated samples are also included for comparison. All the SANS intensity profiles of sulfonated samples possess a characteristic peak at higher q values. This peak is missing in the SANS data of unsulfonated samples and is the focus of this chapter.

Generally, SANS data of sulfonated samples exhibits two characteristic features. One is the peak located at low q in the q range of 0.1 to 0.4 nm^{-1}. We refer to this peak as peak 1. Peak 1 is either missing or less pronounced in the SANS data of samples with IEC values less than 1.4 mmol/g. The position of this peak moves to smaller q values for samples having higher IEC values, which have higher water content. The other characteristic feature in these SANS intensities is the peak located at $q \sim 2$ nm^{-1}. We refer to this peak as peak 2. Peak 2 is very well pronounced in all the sulfonated samples and its peak position is not much affected by IEC values, except in the case of short samples of HGD series (Fig. 6.7 (d)), where peak 2 is shifted to lower q values and merges with peak 1.

As mentioned before, we can identify the origin of each peak by contrast matching experiments. In Chapter 5, we presented SANS measurements in 30:70 mixtures of D_2O:H_2O. In this case, the SLD value of PS matches that of the solvent and peak 2 disappears, and we were able to identify peak 1 with the fluorous domains, since the position of peak 1 is the consistent with the characteristic peak in the SAXS data.

In addition to 30:70 and pure D_2O, we also made measurements in pure H_2O and a 60:40 mixture of D_2O:H_2O. Figure 6.8 shows typical results. We observed three different behaviours. In most of the cases there are two characteristic peaks when the sample is soaked in either D_2O, H_2O or 60:40, as shown in Fig. 6.8 (a). The positions of the peaks are independent of the solvent, although their relative intensities are solvent dependent. However, peak 2, located at larger q values, completely disappears when samples are soaked in 30:70. As discussed in section 3.3 these observations indicate that this system is a ternary system and we identify the origins of peak 1 and peak 2 being fluorous domains and hydrated water-rich domains, respectively.

We observed two other different cases, which were initially puzzling. As shown in

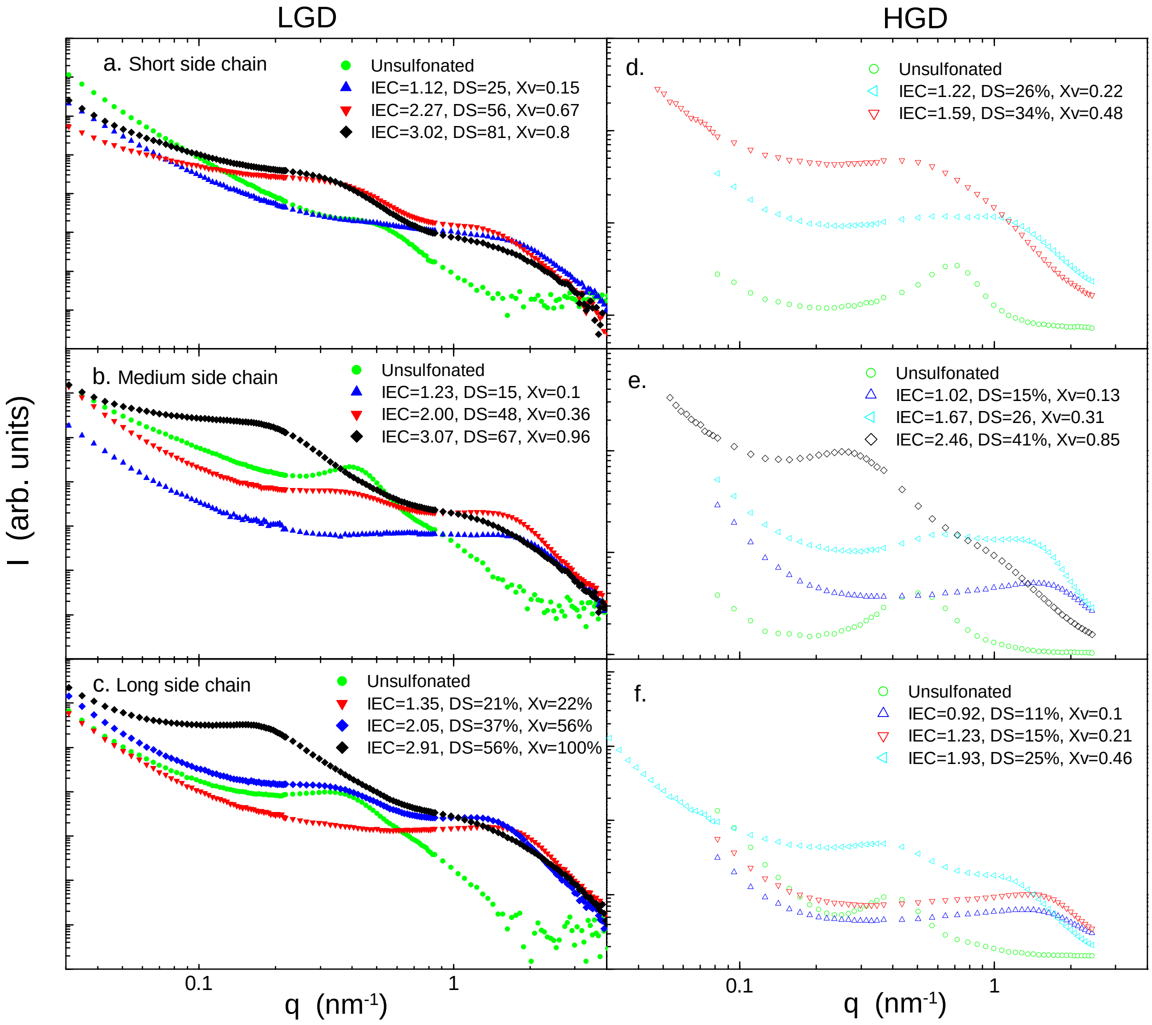

Figure 6.7: SANS intensities of samples soaked in D_2O. The characteristics of sulfonated samples are two peaks located in the q ranges of (0.1 to 0.7) and (1 to 1.2 nm^{-1}). We refer to these peaks as peak 1 and peak 2. Peak position of peak 1 is very sensitive to IEC values and water content for samples with long and medium side chains. Due to contrast matching this peak is missing in some of the data sets. Peak 2 is associated with the scattering from water-rich domains. The position of this peak is most affected by IEC values in samples with short side chains of the HGD series.

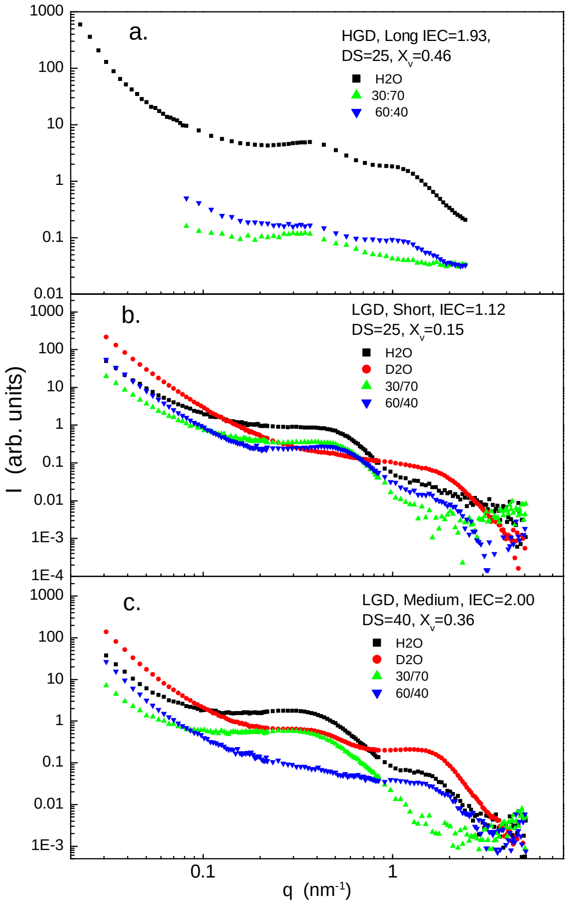

Figure 6.8: SANS data of samples soaked in different solvents. We observed two characteristic peaks. The behaviour of the peaks in different solvents can be explained by considering the SLD of different phases in the samples.

Table 6.3: The average SLD values of the hydrated PS as calculated from Equation 6.3. The values are provided only for the cases in which peak 1 is vanishes. All of the samples belong the LGD series.

Side chain length	IEC (mmol/g)	IEC_{v} (mmol/cm^3)	Solvent	$SLD_{avrg} \times 10^{-4}$(nm^{-2})
Long	1.35	1.7	D_2O	2.1
Long	2.05	2.7	60 : 40	2.9
Medium	1.23	1.6	D_2O	2.2
Medium	2.00	2.7	60 : 40	3.1
Short	1.12	1.7	D_2O	2.6
Short	2.27	2.8	60 : 40	3.1

Fig 6.8 (b), in some cases peak 1 was missing when samples were soaked in D_2O, while in the other cases this peak disappeared when the samples were soaked in the mixture 60:40. Further investigation indicated that in these cases the average of SLD values of solvent, sPS and PS matches with the SLD value of PVDF, and hence, fluorous domains are not distinguishable from the hydrated sPS matrix. The average SLD value of the hydrated and partially sulfonated PS matrix is given by

$$\mathrm{SLD}_{avg} = \frac{V_{solvent}SLD_{solvent} + V_{PS}SLD_{PS} + V_{sPS}SLD_{sPS}}{V_{solvent} + V_{PS} + V_{sPS}} \ , \tag{6.3}$$

in which SLD_{avg} is the average SLD value of water, PS and sPS, and the volume ratios are calculated based on Eq. 2.18. Table 6.3 contains the results for the cases in which peak 1 either vanishes or is poorly pronounced. The values obtained are in good agreement with the SLD value of PVDF ($\mathrm{SLD} = 2.9 \times 10^{-4}\mathrm{nm}^{-2}$) and, hence, are consistent with the absence of peak 1 in the SANS data. Table 6.3 also indicates that for IEC_{v} values of 1.7 and 2.7 (mmol/cm^3) peak 1 disappears in D_2O and 60 : 40, regardless of the length of the side chains. By knowing the origin of the peaks, we were able to analyse the SANS intensities using a ternary morphological model.

6.4 SANS analysis

The fitting function that we considered to characterize the SANS intensities consists of a superposition of two Kinning-Thomas models; one for fluorous domains and one for water-rich domains, in addition to an exponential decay and a constant background. For water-rich domains, we considered a monodisperse version of the model as the number of data points at large q side of the SANS profiles was not sufficient to account for the polydispersity. The fitting function is expressed as,

$$\begin{aligned} & I_{SANS}(q; A1, A2, R_1, R_2, \sigma_1, R_{HS1}, R_{HS2}, \eta_1, \eta_2, A_3, \alpha, Bkg) = \\ & A_1 \cdot I_{KT}(q; R_1, \sigma_1, R_{HS1}, \eta_1) + A_2 \cdot I_{KT}(q; R_2, R_{HS2}, \eta_2) + A_3 \cdot q^{-\alpha_3} + Bkg \ , \end{aligned} \tag{6.4}$$

in which A_i, R_i, σ_i, R_{HSi} and η_i are the amplitudes, average domain sizes, polydispersity, hard sphere radii, and hard sphere volume fractions of fluorous ($i = 1$) and water-rich ($i = 2$) domains. A_3 and α_3 are the amplitude and exponent accounting for the upturn at low angles, and finally Bkg is a constant background. We fit this function to the SANS data using two different methods; first, by fitting each individual data set and secondly, we performed a global fit analysis. The second method was used only for the LGD series, because SANS data for only these samples were available in four different solvents.

The global fit procedure is performed by concatenating the data sets into one large data set. Hence, the χ^2 is defined as,

$$\chi^2 = \Sigma_i\left(\frac{f_1(x_i^1, \hat{\boldsymbol{\theta}}) - y_i^1}{\sigma_i^1}\right)^2 + \Sigma_i\left(\frac{f_1(x_i^2, \hat{\boldsymbol{\theta}}) - y_i^2}{\sigma_i^2}\right)^2 + \cdots + \Sigma_i\left(\frac{f_1(x_i^k, \hat{\boldsymbol{\theta}}) - y_i^k}{\sigma_i^k}\right)^2 \ , \tag{6.5}$$

where x_i^k, y_i^k and σ_i^k are the ith independent variables, its corresponding measured value, and standard deviation for data set k, respectively.

The details of the fitting process for each method are described below.

6.4.1 Fitting each data set individually

Fitting data sets possessing one characteristic peak

As mentioned previously, some of the SANS data sets, particularly those corresponding to samples in the 70:30 solvent, contain only one characteristic peak. For these data sets, we just turn off the contribution of the non-existing peak by setting its amplitude to zero, for example, in the case of 70:30, we set $A_2 = 0$. The fitting process in these cases is similar to that of SAXS data. When dealing with peak 1, the initial values were similar to the ones used for fitting SAXS data. A q range of 0.03 to 2.5 nm^{-1} was chosen for the fitting range. For peak 2, we chose initial values of $R_2 = 1$ nm, $R_{HS2} = 2$ nm and $\eta_2 = 0.2$. In both cases, the initial value of α_3 was -4 and the background was zero. For the first few iterations R_i, R_{HSi}, α_3 and σ_1 were held fixed to reach reasonable values for the amplitudes and background. The fitting process was finalized by letting all of the parameters float.

Fitting data sets containing two characteristic peaks

Fitting this data is more challenging as the fitting function contains 12 parameters. Moreover, in some cases at least one of the peaks was poorly pronounced *i.e.* the ionomer peak in the case of H_2O, as H_2O has a rather low SLD value. Our solution in this case was as follows: for a given sample peak 1 was characterized based on data obtained from samples soaked in 30:70. We used these values in the fitting function and fixed them during the fitting process. This way, the fitting process was reduced to fitting one peak, peak 2, plus the amplitude of peak 1. Hence, we were able to use the same procedure explained for fitting one peak. This approach provides a robust fitting processes. We should emphasize that the proposed model works for samples whose water content is less than 0.8 ($X_v < 0.8$).

One way to validate the proposed model is to check the expected amplitudes with the ones obtained based on the model. The amplitudes of the peaks depend on the SLD values of the solvent in which the sample is soaked. Assuming A_2^{s1} and A_2^{s2} are the amplitudes of peak 2 in solvents 1 and 2, respectively,

$$\frac{A_2^{s1}}{A_2^{s2}} = \frac{(\mathrm{SLD}_{s1} - \mathrm{SLD}_{PS+sPS})^2}{(\mathrm{SLD}_{s2} - \mathrm{SLD}_{PS+sPS})^2} \ , \tag{6.6}$$

where SLD_{PS+sPS}, SLD_{s1} and SLD_{s2} are the SLD values corresponding to the partially sulfonated PS matrix and the two different solvents. SLD_{PS+sPS} depends on the volume ratio of PS and sPS and their SLD values. Of course, the amplitudes of the peaks depend on other factors, such as the number density of the scattering domains, but these factors will not appear in Eq. 6.6 as we are comparing results corresponding to the same sample. Table 6.4 compares the values obtained for the relative intensities of peak 1 and 2 in different solvents, as obtained from the fit results (Expt) and, as calculated based on Eq. 6.6 (Calc). The results are consistent for most of the cases with small deviation between calculated and experimental values. These deviations are larger when the amplitude of peak 1 is small, in at least one of the corresponding SANS data sets. Generally, we believe that the origin of

Table 6.4: The ratio of peak 1 and 2 amplitudes in different solvents as obtained from the fit results (Expt) compared to calculated values (Calc). In most of the cases the experimental and calculated values are consistent with small deviations, the data in bold font indicates that the deviations are large. N/P means that peak 1 does not exist in the SANS intensity, we suggest that this peak vanished because of contrast matching. N/A means that the data was not available.

Sample	peak1				peak2			
	$H2O/D_2O$		$60:40/D_2O$		$H2O/D_2O$		$60:40/D_2O$	
	Exper	Calc	Expt	Calc	Expt	Calc	Expt	Calc
Short $IEC = 1.12$	0.45	0.52	**7.9**	**88.5**	0.23	0.2	0.16	0.18
Short $IEC = 2.27$	0.29	0.21	0.3	0.32	0.23	0.27	N/A	0.16
Medium $IEC = 1.23$	0.72	0.69	N/A	3.5	**7.1**	**0.2**	0.18	0.17
Medium $IEC = 2.00$	0.35	0.36	**18.7**	**2.1**	0.22	0.18	**0.17**	**3.2**
Long $IEC = 1.35$	0.72	0.5	N/P	300.6	0.18	0.21	0.21	0.18
Long $IEC = 2.05$	0.29	0.26	0.38	0.67	1.31	1.32	0.18	0.17

these deviations is the fact that the shell around each fluorous domain contains fluourous chains, as well as PS chains, but in the model we approximate the shell with a pure PS shell. On the other hand, the values obtained for peak 2 are in better agreement with the experimental values.

These results show that the model is self-consistent. For further verification, we explore whether it could be fit to all the SANS data corresponding to the same sample simultaneously.

6.4.2 Global fit

SANS data for the same sample but soaked in different solvents share parameters corresponding to the characteristics of the fluorous and water-rich domains *i.e.* R_1, R_{ca1}, σ_1 and η_1 of peak 1. Only the amplitudes of each peak, due to the contrast factors, should be different. In such a situation, all data sets can be fit simultaneously, through a global fit method. According to Eq. 6.4, for each sample there exists 12 fit parameters for an individual data set, which results in 48 coefficients for four data sets corresponding to one sample. In a global fit, 7 parameters are shared between all the data sets and the number of parameters was reduced to 27.

Global fitting process

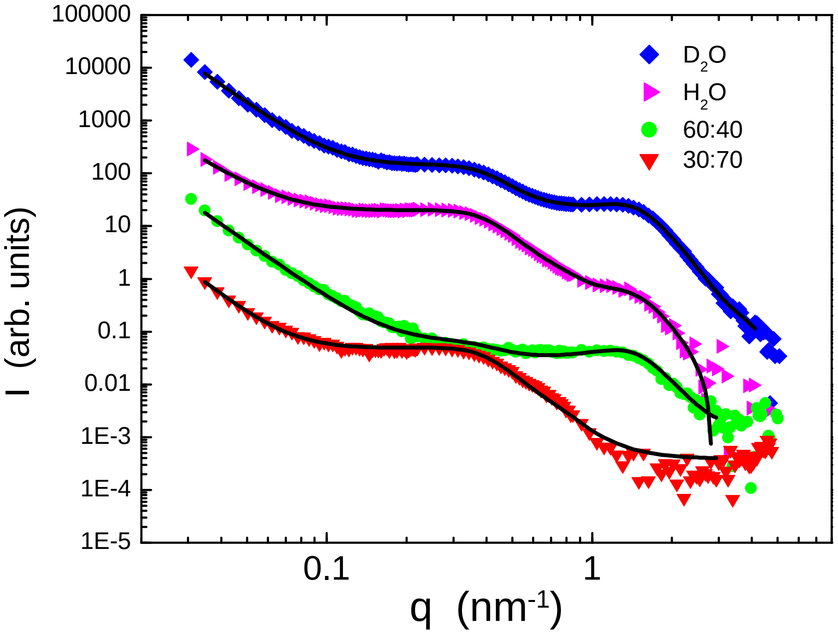

Figure 6.9: SANS data of sample with long side chains and IEC = 2.05 mmol/g of the LGD series. Four data sets correspond to the same sample in different solvents. The black lines are the fit curves obtained based on global fit.

The initial values for the global fit were the same as used for the individual fit. In cases in which one of the peaks was missing, we turned off the contribution of that peak by fixing its amplitude to zero. Of course the other parameters associated with that peak were fixed in such a case. The q range for fitting data were chosen to be 0.03-2.5 nm^{-1}, except for the data corresponding to D_2O for which the fitting range was extended to q = 4 nm^{-1} because, in this case, the data is not noisy at higher q values. As illustrated in Fig. 6.9, the global fit provides excellent fitting curves. The characteristic parameters that were obtained based on this method are consistent to within 5% of the ones obtained by fitting the data individually. We were able to use this method only for samples of the LGD series, because for the other series data was not available in different solvents. Therefore, when comparing the characteristic parameters of the two series, we consider the results obtained based on individual fits for the sake of consistency.

6.5 Fit results

Parameters related to the fluorous domains were discussed in Chapter 5. In this section, we focus on the characterization of peak 2. Figures 6.10 (a)-(c) contain the values obtained for R_2, R_{HS2} and η_2 as a function of X_v.

As shown in Fig. 6.10 (a) and (b), for samples of the LGD series, both R_2 and R_{HS2} increase gradually with water content from 0.9 and 1.4 nm to 1.3 and 2.3 nm, respectively. For the other series, however, no trend is observed in R_2 and R_{HS2} and the values fluctuate around 0.9 and 2 nm, respectively, except for the sample with shortest side chains and higher X_v. This sample exhibits the largest R_2 and R_{HS2} values of all samples.

Figure 6.10 (c) contains the hard-sphere volume fraction η_2. Generally, both series of the samples show a gradual increase in the hard-sphere volume fraction from 10 to 20% as the water content is increased; again the only exception is for sample with the shortest side chains and high X_v. This sample does not follow the same trend as the other samples and has a lower η value if we extrapolate the trend of the other samples of these series. In the next section, we try to analyze this data and find out if these characteristics are correlated with the conductivity.

6.6 Discussion

In Chapter 2, we addressed the relationship between conductivity and details of chemical architecture of the studied materials based on mass-based properties. In this chapter, we will use the volume-based properties as most of our arguments are morphology oriented. Moreover, one of the important factors in conductivity is the conductive volume of the membrane [20, 95]. Since protons travel in the water domains, it has been suggested that the volume of the water in the membrane is a good approximation of the conductive volume [95]. Y. S. Kim and B. S. Pivovar [95] suggested that water content of the fully hydrated PEMs is the most relevant parameter to the conductivity. They demonstrated this idea by plotting conductivity of different PEMs as a function polymer conductive volume or water content. They showed that the conductivities of different materials collapse to one single curve. Following this approach, we decided to compare how the conductivity of different series changes as a function of IEC, IEC_{v} and X_{v}. Figure 6.11 (a)-(c) show the results. Figure 6.11 (a) shows the conductivity as a function of IEC and contains the data

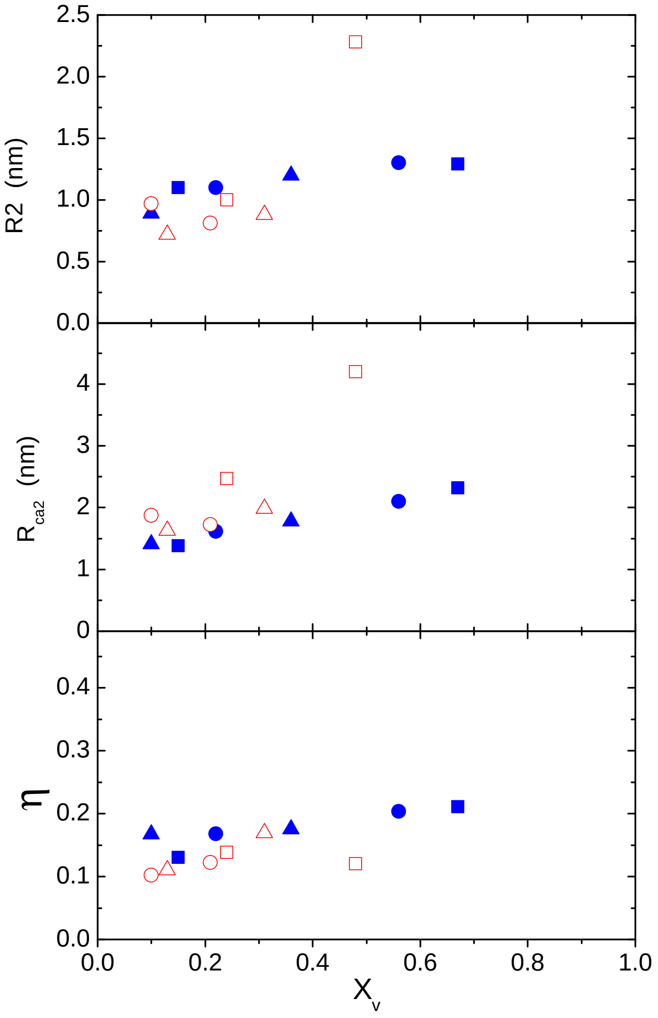

Figure 6.10: Characteristics of hydrated ion-rich domains that were obtained based on a model of monodispersed hard spheres with liquid-like order, the Kinning-Thomas model: (a) radius of the core of water-rich domains, (b) radius of the hard sphere domain (core plus shell), and (c) volume fraction of the hard sphere domains.

reported in Fig. fig:ConWUpvsIEC. In this case we observe a partial collapse of the data at lower IEC range. We notice that by plotting conductivity as a function IEC_{v} only the HGD series collapse into one curve. But when conductivity is plotted as a function of X_{v}, data corresponding to the LGD series collapses to another curve very close to that of the HGD series, as shown in Fig. 6.11 (c). According to Y. S. Kim and B. S. Pivovar [95], this behaviour indicates that the details of morphology and chemical architecture have second order effects on conductivity and water content dictates the conductivity.

Another relevant parameter is the IEC_{water} or the ion content of the water. Figure 6.12 (a) shows how the IEC_{water} values of both series decrease as X_{v} increases. The ions become diluted. This data indicates that IEC_{water} values of all of the samples follow the same trend, independent of the details of chemical structure such as length of the side chains and graft number density. Figure 6.12 (b) shows how the conductivity changes as a function of IEC_{water}. The collapse of the data is even better in this case and we suggest that this parameter may be the most relevant to the conductivity of fully hydrated samples. Note that in Fig. 6.12 (b) data is plotted such that water content increases from left to right. This figure indicates that at low water content the ion content of water is very high but conductivity is very low. By increasing the water content, ions become diluted and conductivity increases. When the IEC_{water} reaches 1.2 (mmol/cm^3) the conductivity of the samples drops. We believe the drop in conductivity is due to the low acid concentration, as proposed by Holdcroft *et al.*[9, 88, 96]. In the last part of this chapter, we propose a model which is able to explain the dilution behaviour observed in Fig. 6.12 (a). We argue that one key parameter in the conductivity of these membranes is the existence of ionic-nano channels which are responsible for the connectivity between the water-domains.

In order to gain insight into the connectivity, we need to know how much of the water participates in forming the spherical water-rich domains Λ, and what is the average spacing between these domains r_0. We know that the volume of each water-rich domain is $V_{R_2} = \frac{4\pi}{3}R_2^3$; therefore, the fraction of water which participates in forming water-rich domains is

$$\Lambda = \frac{V_{R_2}}{X_{\mathrm{v}} V_{p2}} \ . \tag{6.7}$$

The results are shown in Fig. 6.13 as a function X_{v}. The Λ value drops dramatically with increasing the water content. These values are typically smaller than 0.5, which means that most of the water does not contribute in forming the water domains. Interestingly, different

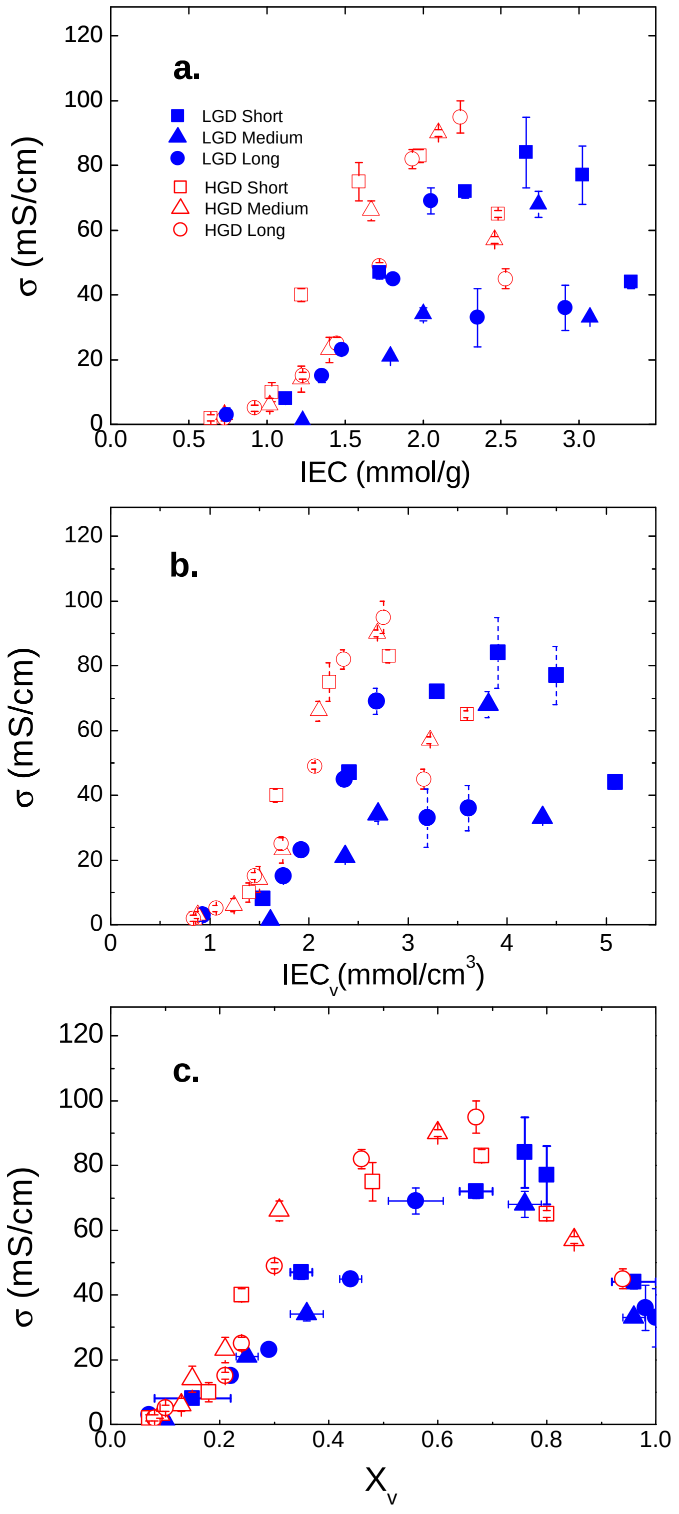

Figure 6.11: Conductivity of different sets of samples plotted as a function of (a)IEC, (b) IEC_v and (c) X_v. Data was provided by Dr. Tsang and Ms. Yang [1, 22].

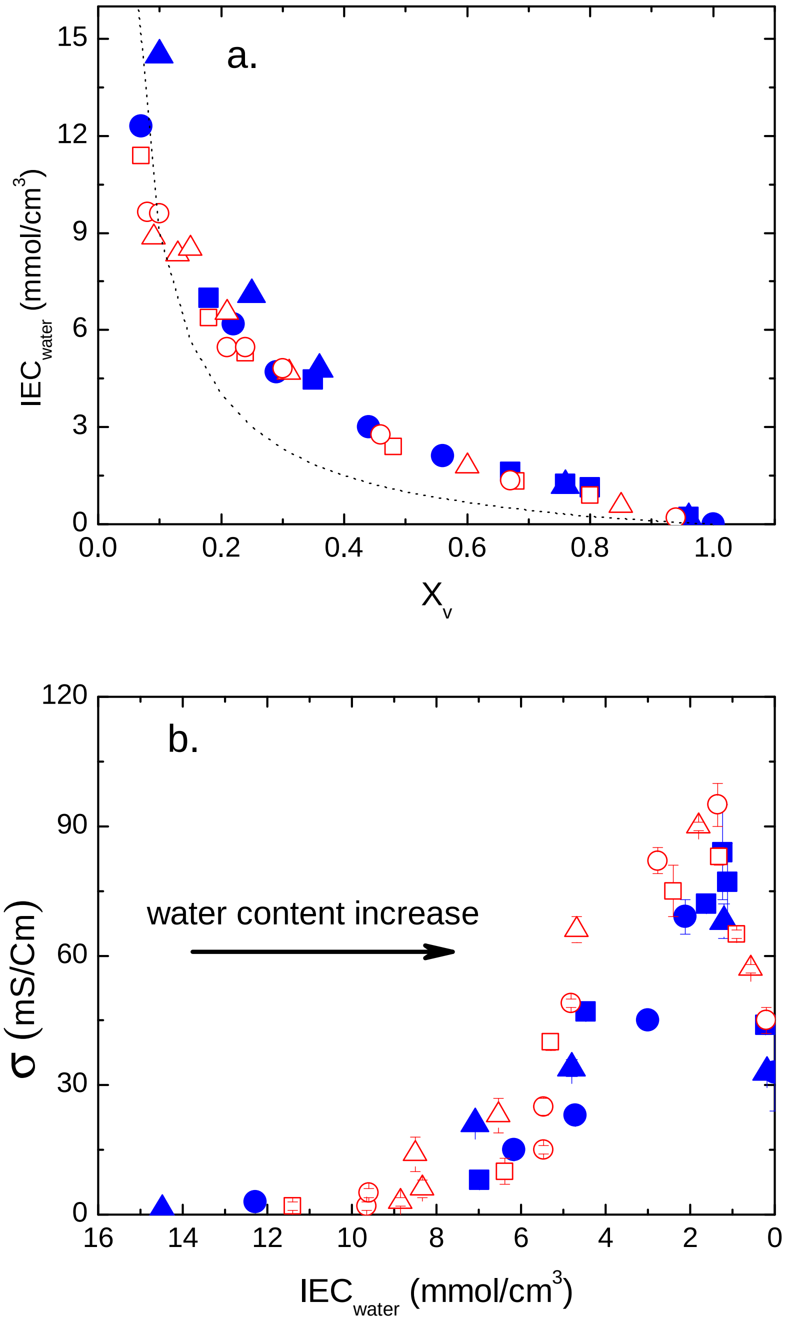

Figure 6.12: (a) Water ion content IEC_{water} plotted as a function of X_{v}. The dotted line represent the ratio of the polymer volume to the water volume. (c) Conductivity plotted as a function of IEC_{water}. The horizontal axis is reverse such that water content increase from left to right, as shown by the arrow.

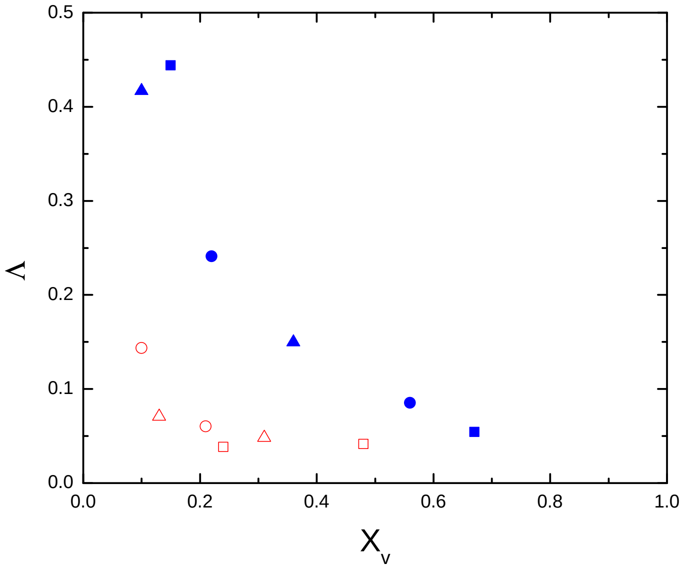

Figure 6.13: The fraction of water that participate in forming water-rich domains Λ plotted as function of X_v. By increasing water content, Λ values decrease in both series. Each series of samples follow a given trend regardless of the length of the side chains.

samples in each series follow the same curve regardless of the length of their side chains, but there is a clear difference between the two series with the fraction of water in the water-rich domains being much higher in the LGD series. This suggests that the graft number density has a strong impact on the distribution of water in the membrane, presumably because of either the crystallinity or degree of phase separation.

One possibility is that the water that is not part of the water-rich domains is forming nano-channels. This idea was proposed originally by Gierke *et al.* [60] and used by other groups latter [21, 24]. Beers and Balsara [21] proposed the existence of ion-free water channels, that is a series of spherical water domains containing ions connected by ion-free nano-channels. Figure 6.14 shows their proposed model. They concluded that the length of the channels should be less than 1 nm in order to have good conductivity. Based on this model, Beers and Balsara argued that the existence of the ion-rich domains impedes the proton conduction. We were curious if the size of the channels in our system follow the condition necessary for the ion-free channels.

The number density of the water-rich domains $n_{\mathrm{water-rich}}$ and their spacing r_0 can be

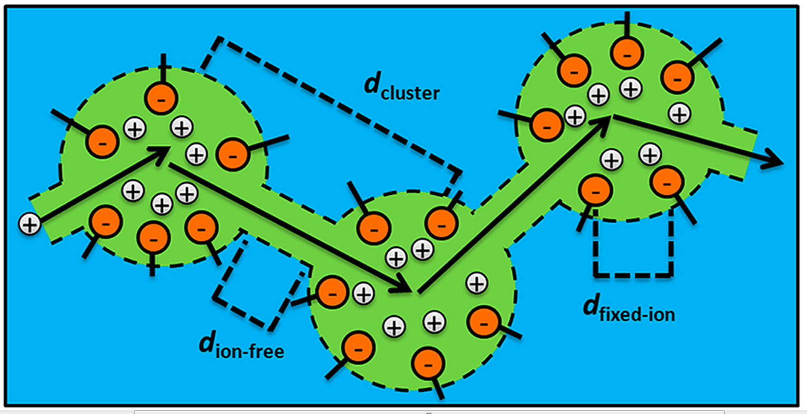

Figure 6.14: Beers and Balsara [21] proposed that there are water nano-channels in the ionomer membrane that are ion-free and therefore protons have to hop cross each channel between domains. From [21], used with permission.

calculated according to the following equations

$$\eta_2 = \frac{4\pi}{3} R_{HS2}^3 n_{\text{water-rich}} \ , \tag{6.8}$$

and

$$V_{p1} = \frac{1}{n_{\text{water-rich}}} = \frac{4\pi}{3} r_0^3 . \tag{6.9}$$

Figure 6.13 (a) and (b) show how the number density of the water-rich domains and their spacing changes as a function of X_v. These results indicate that the spacing between domains increases as X_v increases. It is interesting to notice that r_0 values of the samples of the LGD series follow a linear trend, therefore we suggest that higher degree of crytallinity, larger fluorous domain sizes and/or unsegregated fluorous segments dictate the morphology of the water-rich domains. On the other hand, samples of the HGD series do not follow any specific trend and have lower number densities of water-rich domains compared to the other series, as shown Fig. 6.15 (a). Our results also indicate that samples with short side chains in the HGD series have the largest r_0 values, which is equivalent to lowest number density of the water-rich domains. These results are consistent with the model proposed based on the TEM technique, as discussed in chapter 2. The length of the channels is equal to

$$\text{d}_{\text{channel}} = r_0 - 2R_2 . \tag{6.10}$$

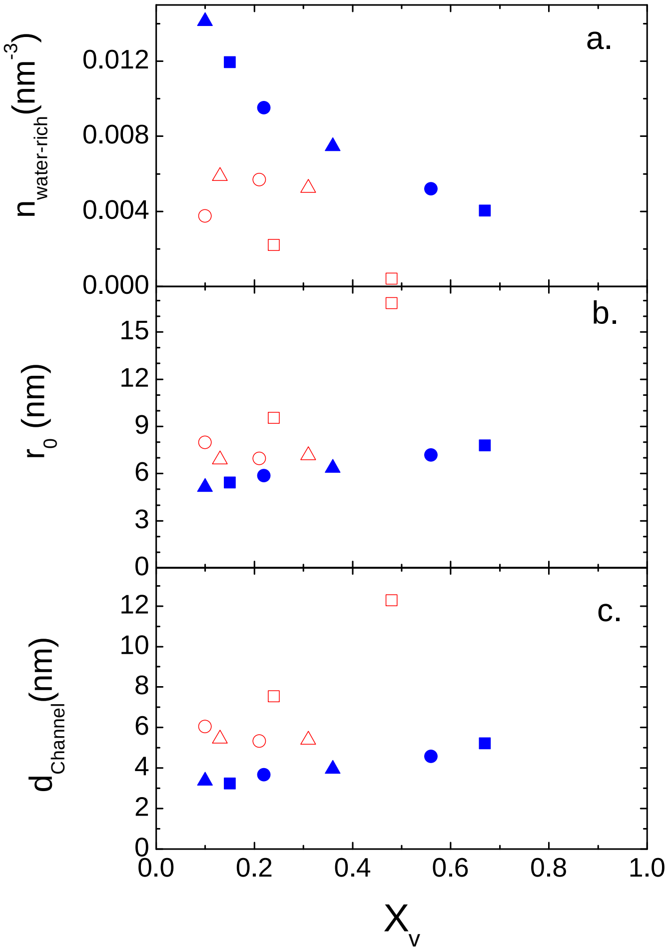

Figure 6.15: (a) number density of the water-rich domains and (b) Spacing between the water-rich domains plotted as a function of water content X_v. As water content increases number density of the domains decreases and they become farther apart. (c) length of the water channels as a function of water content X_v.

Figure 6.13 (c) indicates that the length of the channels also increases as X_v increases, and more importantly in all cases the length of the channels are longer than 3 nm. Therefore, according to Beers and Balsara [21], protons cannot hop through these channels if they are ion-fee. This suggests that if the excess water is in the form of nano-channels between domains, they are not ion-free.

One question to answer is why some of the acid groups do not participate in forming the ionic aggregates. We believe that the answer lies in the conformation of the partially sulfonated PS chains in the vicinity of the water-rich domains. In fact, the formation of the spherical water-rich domains, which minimizes the the local free energy of the ionomer-water system, is dictated by factors such as osmotic pressure, elastic pressure applied by the polymer matrix, Coulombic interactions, and also environmental factors, such as temperature [11]. We suggest that the origin of the water channels are those acid groups that cannot participate in forming spherical water-rich domains. Our explanation is as follows: when an assembly of ionic acid groups forms a water-rich domain,there is a possibility that some other acid groups are dragged toward this aggregate, as they are tethered to the polymer chains. But as the water-rich domain has already obtained its optimum size, the extra acid groups are not welcome to join in. This situation is shown schematically in Fig. 6.16 (a). Moreover, these extra acid groups cannot move around freely and find enough other acid groups to build a water-rich domain. Hence, these acid groups form partially hydrated channel-like structures. By increasing the IEC values, the proximity of the acid groups along the chains increases but the size of the clusters (or water-rich domains) is not much affected, as observed experimentally (Fig. 6.10). This means that at higher IEC values, more acid groups participate in forming water channels rather than spherical domains.

We suggest that at higher water content, the spherical domains disappear, and instead, a connected network of water domains will be obtained. However, we were not able to characterise the SANS intensities of highly swollen membranes; instead we propose to fit these data to the Teubner-Strey model, as future work.

Now, the question is how the details of this proposed morphology is related to the conductivity. We found our answer in the approach proposed by Balog *et al.* [24]. They suggested that the conductivity of the membrane is a linear function of a morphology-related factor, the ratio of the domain size to the separation of the domains $\frac{R2}{r_0}$, and the average number of water molecules associated with each domain. Since their SAXS measurements

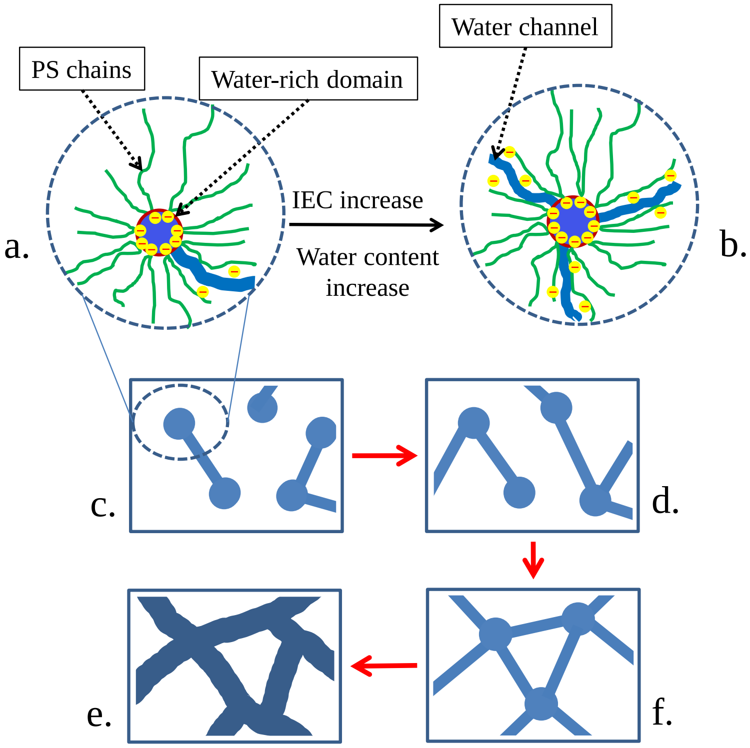

Figure 6.16: (a, b) schematic showing the conformation of the partially sulfonated PS chains in the vicinity of the water-rich domains. We propose that the origin on the water nano-channels are those acid groups that do not participate in forming spherical water domains. Parts (c-f) show how the morphology of the water-rich domains may evolve as the *IEC* of values increases. As *IEC* values increases, the size of the water-rich domains shows a very small increase, while their spacing increases significantly, therefore we propose that the extra volume of the water leads to more and more water channels. Eventually, at higher water content values, the morphology becomes that of connected network.

were performed on dry samples, they had to estimate the number of water domains using X_v. Instead, we consider the average volume of water associated to each domain $X_\mathrm{v}V_{p2}$, in which V_{p2} is the volume of the hydrated sample per water-rich domain.

Figure 6.17 shows the conductivity of the membranes plotted as a function of $X_\mathrm{v}V_{p2}\frac{R2}{r_0}$. Ten of the twelve samples that we can evaluate in this way show a linear relationship between the conductivity and $X_\mathrm{v}V_{p2}\frac{R2}{r_0}$. We think that the slope of the line depends on the properties of the materials *i.e.* proton diffusion in hydrated sPS matrix. By extrapolating the data linearly to zero, we obtain a threshold level, $X_\mathrm{v}V_{p2}\frac{R2}{r_0} = 1.2$ nm^3. This threshold level can be interpreted as the percolation threshold at which a minimum volume of water is required to create connective domains and consequently a conductive membrane.

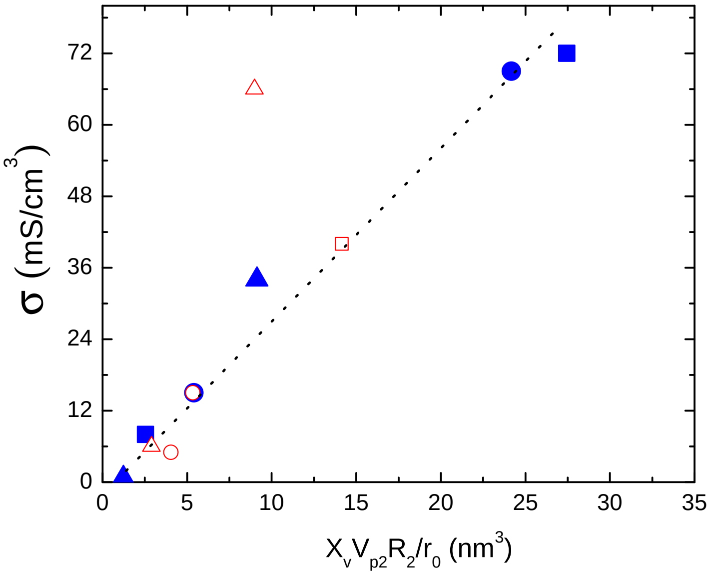

Figure 6.17: Conductivity plotted as a function of $X_\mathrm{v}V_{p2}\frac{R2}{r_0}$. For HGD sample with higher water content, $X_\mathrm{v}V_{p2} = 200\mathrm{nm}^3$ and is out of the range. Among the rest of 11 data points, one of them does not fit the model.

Our results are consistent with results of Balog *et al.* [24]. They studied ETFE-*g*-Poly(sulfonated styrnen-*co*-DVB) membranes in the dry state and were able to measure the size of the domains by staining the samples. They observed that water content decreases with cross-link level, at the same time the size and number density of the ion-rich domains increases. However, in the system that we studied, the size of the water-rich domains increases by increasing the water content, while number density decreases (or in other terms, domain spacing increases). This suggests that the morphology of the water-domains is affected by the nature of the the polymer matrix. Despite these differences, it is very interesting that we could use the same approach to explain the correlation between structural properties and conductivity. This analysis is just a heuristic approach and suggests which factors can contribute to the conductivity of the membrane. Hopefully, other researchers in the field can use these results in more precise ways, for example in computational models.

6.7 Summary

We were able to characterize the morphology of the water-rich domains by analysing the SANS data of hydrated samples. A model of polydisperse spheres with liquid-like order was fit to the data. The model was confirmed by comparing the results obtained for samples soaked in different solvents. Our results indicate that the average size of the domains and the spacing between them increase slightly with water content, but is generally independent of side chain length and graft number density along the backbone. We find that most of the water does not participate in forming water-rich domains and suggest that the extra water in the membrane forms ionic nano-channels of water which are responsible for the connectivity of the spherical water-rich domains. Using the approach proposed by Balog *et al.* [24], we have shown that the conductivity of the membrane is strongly correlated to the size of the water-rich domains, the water volume corresponding to each domain, and inversely correlated to the spacing between the domains.

Chapter 7

Summary and Outlook

In this study, we have used different scattering techniques, WAXS, SAXS and SANS, to obtain an in-depth understanding of the morphology of P[VDF-*co*-CTFE]-*g*-sPS] membranes, both as examples of random graft copolymers and as PEM materials. Previous studies of this material indicated that the ionic groups in these materials develop a random morphology. However, these studies, which were based on TEM analysis, did not provide a precise picture of the overall morphology. In this study, we have proposed a self-consistent morphological model for these membranes. The proposed model consists of spherical fluorous and water-rich domains embedded in a continuous phase of PS. The model was implemented using the Kinning-Thomas model to characterise the different domains in both hydrated and dry states. In forming these domains two processes are involved: the phase separation between the segments of the backbone and side chains, and the aggregation of ionic groups. We determine the degree of phase separation by comparing the volume of the fluorous domains with the fluorous volume available in the samples. Our results indicate that crystallinity hinders the first type of phase separation. The phase separation of fluorous domains is also affected by the aggregation of the ionic groups: unsulfonated and fully sulfonated samples developed the highest degree of phase separation while the fluorous segment phase separation was generally suppressed by the aggregation of the ionic acid groups in partially sulfonated samples. The only sample set in which phase separation of fluorous domains was improved upon partial sulfonation, was the sample set with the longest side chains $n = 154$. Moreover, measurements on hydrated samples indicated that the membrane swelling degree at nano-scale is consistent with water content values, as long as water content is < 0.8.

We also discovered that samples with side chains longer than $n = 78$ have the same water content behaviour, and details of morphology and chemical structure becomes irrelevant to water content. However, in the case of samples with short side chains, having a higher degree of crystallinity and a lower degree of phase separation, improves the resistance of the membrane swelling.

We have shows that the characteristic peak in the SANS intensity data of hydrated samples originates from the water-rich domains. The consistency of the model was verified using the contrast matching technique. We found that the size of the domains and their spacings in the LGD series is not affected by the length of the side chains. However, in the HGD series, samples with short side chains possess larger values when compared to samples with long and medium side chains. Our results also indicates that the spacing between the domains is more affected by X_{v} compared to the size of the water-domains. Moreover, we proposed that IEC_{water} is a relevant parameter to the conductivity. According to our results, most of the water does not participate in forming spherical water-nano domains at higher water content. We suggest that the extra water forms ionic nano-channels rather than ion-free nano-channels, because their average length is larger than 3 nm. We showed that conductivity is proportional to the amount of water corresponding to each water-rich domain and the size of the domains, while inversely proportional to the spacing between them.

7.1 Outlook for data analysis

We would like to apply the Teubner-Strey model for samples with $X_{\mathrm{v}} > 0.5$. We have already pointed out that the Kinning-Thomas model breaks down for samples with $X_{\mathrm{v}} > 0.8$. The Teubner-Strey model may provide a more satisfactory fitting function as it does not consider any well defined shape for the scattering entities.

The other way to analyse the data would be to use the approach proposed by Schmidt-Rohr and Chen [18]. In this approach the 3-D morphology is created and then the scattering intensities are calculated based on the Fourier transformation [97]. Figure 7.1 shows preliminary results for the illustrated morphology. The algorithm to create this morphology was briefly described in Chapter 2. The size of the domains and the thickness of the PS shells are chosen to be close to experimental values. The general scattering intensity that was obtained based on this method is consistent with experimental results. These simulations can improve the validity of the model and also might be used to investigate the morphology of samples with a high water content.

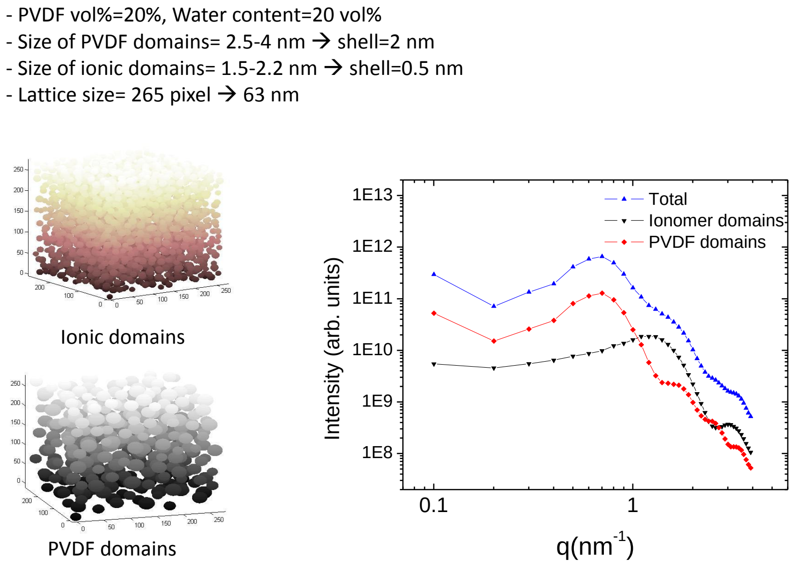

Figure 7.1: Outlook for improving the model based on simulations. On the left hand side the 3-D morphology of VDF and water-domains is illustrated and on the right hand side the calculated scattering intensities are plotted as a function of q.

7.2 Outlook regarding to SANS and SAXS measurements

All of the SANS measurements for the current work were performed on fully hydrated samples. We believe that SANS measurements under humidity controlled conditions will be very useful. In particular, the samples that have very high water content properties are excellent candidates for these kind of measurements, which may give rise to a better understanding of the ion-aggregates upon hydration. The other motivation for these experiments is the fact that conductivity values for such conditions have been measured [22, 1] and a phenomenological model is already available [98] to analyse the experimental data.

7.3 Blend samples

Blending usually involves mixing two polymers with different properties, in order to improve the desired properties of the material. Our collaboration team has done some tests of the effects of blending on the water uptake properties of the available ionomer copolymers [99]. Blending may be a way to further investigate the effects of crystallinity and PVDF ratio on our polymers. Blending not only provides a method to acquire target PVDF ratios but we can also obtain samples with different degrees of crystallinity by blending ionomers with different copolymers. We believe these types of experiments can help us to differentiate between the effects of crystallinity and PVDF ratio on the water content properties. These ideas have been partially implemented; in Ref. [99], we studied the effect of blending PVDF with samples of the HGD series. In this study, PVDF had a molecular weight of $\sim$ 2000Da. We found that, although the ion content of the membrane decreases by more than 50% upon blending, the water content and conductivity of the membranes do not change as much.

In a more recent project, we also tried to blend the samples of the LGD with three different fluorous polymers: PVDF with molecular weight of $\sim$ 2000Da and $\sim$ 270000Da, in addition to the macroinitiator (P[VDF-*co*-CTFE]) containing 2.6% CTEF with molecular weight of $\sim$ 123000Da.

We blend the sample with $IEC = 2.91$g/mol and long side chain of the LGD series with the three mentioned polymers. The blending ratio was 70wt% ionomer content. Figure 7.2 compares the expected water content of this sample with the results of blending with different polymers and also with water uptake properties of sample sets with short side chains of the HGD and LGD series.

Generally, as the blending method leads to more PVDF, one would expect a decrease in water content. One can calculate the expected water uptake upon blending by including the PVDF contribution in the water uptake value of the pristine ionic graft. If we assume that water uptake is only affected by increasing the mass ratio of the PVDF segment, water uptake changes as

$$\text{Water uptake}_{\text{Graft}} = \frac{\text{Water}}{M_{\text{Graft}}} \rightarrow \text{Water uptake}_{\text{Blend}} = \frac{\text{Water}}{M_{\text{Graft}} + M_{\text{PVDF}}} \ , \qquad (7.1)$$

where, M_{PVDF} is the mass increase upon blending and M_{Graft} is the mass of the dry pristine graft sample.

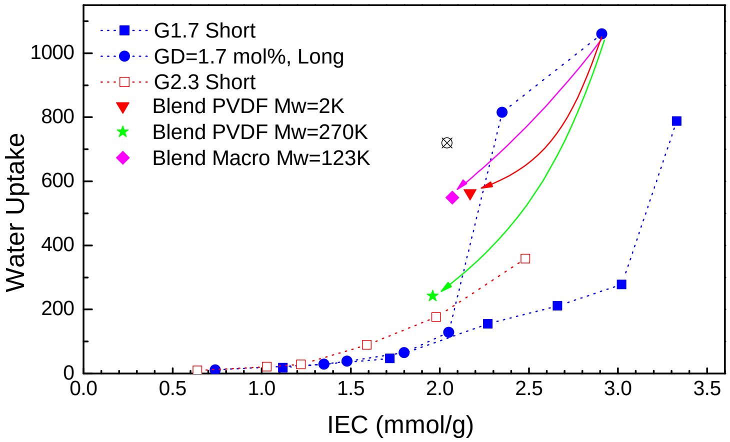

Figure 7.2: Water uptake values of the blend samples compared to the water uptake values of samples of the LGD series with long and short side chains, in addition to that of samples of HGD series and short side chains. As shown by the arrows, for blend samples, the pristine graft copolymer belongs to the LGD series with long side chain and has the highest water uptake. Data provided by Ami C. C. Yang. We also calculated expected water uptake due to increase of the mass ratio of VDF contributes ($\otimes$).

The experimental values obtained for water uptake in all cases are smaller than the calculated values, which indicates the effect of blending is more than just increasing VDF ratios. The most desirable water uptake is obtained by blending the graft ionomer with the PVDF possessing the largest molecular weight. We believe that a deep understanding of these behaviours can be obtained by performing SAXS, SANS and WAXS measurements on these systems. The questions to answer are as follows: how does the blending change the morphology of the fluorous and water-rich domains? Is the water absorption homogeneous at the nano-scale level? Is there any correlation between the conductivity of the membranes and the details of their morphology? These are the questions that we were able to address for a system of pristine ionomer graft copolymers. We believe that answering these questions, in the blend systems, will improve our understanding of the structure-morphology-property of these membranes.

Appendix A

Kinning-Thomas Model

For a system of particles, the scattering intensity depends on the square of the contrast difference Δ^2, the number of the scattering particles N, the shape and size of the particles as expressed as a form factor $F(q)$, and finally, interparticle correlations which are expressed as a structure factor $S(q)$. Therefore, scattering intensities can generally be written as

$$I(q) = \Delta^2 N F(q) S(q) \ . \tag{A.1}$$

In the Kinning-Thomas model the particles are describes as poly-disperse spheres of radius $\bar{R}$. The spheres are embedded in a continuous matrix of another material. This material makes a rigid shell around each domain. We refer to the core and its surrounding shell as hard-sphere. The radius of the hard-spheres is R_{HS} and they have a liquid-like order. However, only the core itself contributes to the form factor.

A.0.1 Form factor of polydisperse spheres

For a system of identical spheres with radius of R, the form factor is equal to

$$F(qR) = \Phi^2(qR) = \left(\frac{3}{(qR)^3} [\sin(qR) - qR\cos(qR)] \right)^2 \tag{A.2}$$

in which $\Phi(qR)$ is the first order Bessel function. If the particles are polydisperse, the form factor can be expressed in term of the average of the form factor. Assume the radius R of the particles is expressed by a distribution of radii $p(R, \bar{R}, \sigma_R)$ where $\bar{R}$ is the average radius, and σ_R is the standard deviation. The form factor of a system of such particles is given by [75, 76]

$$P(q;\bar{R},\sigma_R) = \int_0^\infty p(R,\bar{R},\sigma_R) f^2(q;R) dR / \int_0^\infty p(R,\bar{R},\sigma_R) dR \ , \ . \tag{A.3}$$

where

$$f(q;R) = (\frac{4\pi}{3}) R^3 \Phi(qR) \ . \tag{A.4}$$

One way to analytically calculate this integral is to use a Schulz distribution to describe the polydispersity [100]

$$p(R,\bar{R},\sigma_R) = (\frac{Z+1}{\bar{R}})^{Z+1} R^Z exp[-(\frac{Z+1}{\bar{R}})R]/\Gamma(Z+1) \ , \tag{A.5}$$

where the root mean square deviation is equal to

$$\sigma_R = (\bar{R^2} - \bar{R}^2)^{\frac{1}{2}} = \bar{R}/(Z+1)^{\frac{1}{2}} \ , \tag{A.6}$$

and $\Gamma(X)$ is the Gamma function, Z is width of the distribution, $\bar{R}$ and $\bar{R^2}$ are the mean values of radius and radius squared: $\bar{R} = \int_0^\infty Rp(r)dR$ and $\bar{R^2} = \int_0^\infty R^2 p(r)dR$.

Using this distribution, Kotlarchyk and Chen analyticaly calculated the form factor for a system of polydisperse spheres [100]

$$P(q;\bar{R},\sigma_R) = 8\pi^2 \bar{R}^6 (Z+1)^{-6} \alpha^{Z+7} G_1 \ , \tag{A.7}$$

in which G_1 is

$$\begin{aligned} G_1 \ = \ & \alpha^{-(Z+1)} - (4+\alpha^2)^{-(Z+1)/2} \cos[(Z+1)\tan^{-1}\frac{2}{\alpha}] \\ & -2(Z+1)(4+\alpha^2)^{-(Z+2)/2} \sin[(Z+2)\tan^{-1}\frac{2}{\alpha}] \\ & +(Z+2)(Z+1)(\alpha^{-(Z+3)} + (4+\alpha^2)^{-(Z+3)/2} \cos[(Z+3)\tan^{-1}\frac{2}{\alpha}]) \ , \end{aligned} \tag{A.8}$$

where α is,

$$\alpha = (Z+1)/q\bar{R} \ . \tag{A.9}$$

A.0.2 Structure factor

The structure factor depends on the spatial distribution of the particles. Ornstein and Zernike showed that the structure factor for a system of a dense gases or fluid can be described in terms of direct correlation function [41, 101]. Later, Percus-Yevick found an analytical approximation of the Ornstein-Zernike correlation function which describes a system of hard-spheres with radius R_{HS}. The Percus-Yevick structure factor for hard-sphere depends on the average spacing between the hard-spheres $r_0 > R_{HS}$ can be calculated from the volume of the sample per domain V_p or the number density of the domains n_D

$$V_p = \frac{1}{n_D} = \frac{4\pi}{3} r_0^3 \ . \tag{A.10}$$

The structure factor $S(q; R_{ca}, \eta)$ is an explicit function of the hard-sphere volume fraction η

$$\eta = \frac{4\pi}{3} R_{HS}^3 n_D \ , \tag{A.11}$$

and is given by [76]

$$S(q, R_{HS}, \eta) = \frac{1}{1 + 24\eta G_{ca}(A)/A}, \tag{A.12}$$

where $A = 2qR_{HS}$ and

$$\begin{aligned} G_{ca} = \quad & \frac{\alpha_{ca}}{A^2}(\sin A - A\cos A) + \frac{\beta_{ca}}{A^3}(2A\sin A + (2 - A^2)\cos A - 2) \\ & + \frac{\gamma_{ca}}{A^5}(-A^4\cos A + 4[(3A^2 - 6)\cos A + (A^3 - 6A)\sin A + 6]) \ , \end{aligned} \tag{A.13}$$

in which

$$\alpha_{ca} = \frac{(1+2\eta)^2}{(1-\eta)^4} \ , \beta_{ca} = \frac{-6\eta(1+\eta/2)^2}{(1-\eta)^4} \ , \gamma_{ca} = \frac{1/2\eta(1+2\eta)^2}{(1-\eta)^4} \ . \tag{A.14}$$

A.1 The Kinning-Thomas model

The Kinning-Thomas model expresses the scattering intensities of a system of random spheres in terms of their average size $\bar{R}$, polydisperisty σ_R, radius of the hard-sphere R_{HS}, and finally volume fraction of the hard-spheres η; and is equal to

$$I_{KT}(q;\bar{R},\sigma_R,R_{HS},\eta) = KP(q;\bar{R},\sigma_R)\cdot S(q;R_{HS},\eta)\ , \tag{A.15}$$

in which K is the normalization factor and depends on the scattering at zero angle: $K = I_{KT}(q=0;\bar{R},\sigma_R,R_{HS},\eta)$.

Bibliography

[1] E. M. W. Tsang, Z. Zhang, C. C. Yang, Z. Shi, T. J. Peckham, R. Narimani, B. J. Frisken, and S. Holdcroft, “Nanostructure, Morphology, and Properties of Fluorous Copolymers Bearing Ionic Grafts,” Macromolecules **42,** 9467–9480 (2009).

[2] H. Zhang and P. K. Shen, “Advances in the high performance polymer electrolyte membranes for fuel cells,” Chem. Soc. Rev. **41,** 2382–2394 (2012).

[3] H. Wang, H. Li, and X. Yuan, *Pem Fuel Cell Diagnostic Tools*

[4] R. Devanathan, “Recent developments in proton exchange membranes for fuel cells,” Energy Environ. Sci. **1,** 101–119 (2008).

[5] K. A. Mauritz and R. B. Moore, “State of Understanding of Nafion,” ChemInform **35,** no–no (2004).

[6] M.-H. Kim, C. J. Glinka, S. A. Grot, and W. G. Grot, “SANS Study of the Effects of Water Vapor Sorption on the Nanoscale Structure of Perfluorinated Sulfonic Acid (NAFION) Membranes,” Macromolecules **39,** 4775–4787 (2006).

[7] M. Eikerling, A. A. Kornyshev, and A. R. Kucernak, “Water in Polymer Electrolyte Fuel Cells: Friend or Foe?,” Physics Today **59,** 38–44 (2006).

[8] S. Paddison, “Proton conduction mechanisms at low degrees of hydration in sulfonic acid-based polymer electrolyte membranes,” ANNUAL REVIEW OF MATERIALS RESEARCH **33,** 289–319 (2003).

[9] T. J. Peckham and S. Holdcroft, “Structure-Morphology-Property Relationships of Non-Perfluorinated Proton-Conducting Membranes,” Advanced Materials **22,** 4667–4690 (2010).

[10] A. Kusoglu, S. Savagatrup, K. T. Clark, and A. Z. Weber, “Role of Mechanical Factors in Controlling the StructureFunction Relationship of PFSA Ionomers,” Macromolecules **45,** 7467–7476 (2012).

[11] M. H. Eikerling and P. Berg, “Poroelectroelastic theory of water sorption and swelling in polymer electrolyte membranes,” Soft Matter **7,** 5976–5990 (2011).

[12] L. Rubatat, Z. Shi, O. Diat, S. Holdcroft, and B. J. Frisken, "Structural Study of Proton-Conducting Fluorous Block Copolymer Membranes," Macromolecules **39,** 720–730 (2006).

[13] G. Gebel and O. Diat, "Neutron and X-ray Scattering: Suitable Tools for Studying Ionomer Membranes," Fuel Cells **5,** 261–276 (2005).

[14] B. Chu and B. S. Hsiao, "Small-Angle X-ray Scattering of Polymers," Chemical Reviews **101,** 1727–1762 (2001).

[15] G. Gebel and J. Lambard, "Small-Angle Scattering Study of Water-Swollen Perfluorinated Ionomer Membranes," Macromolecules **30,** 7914–7920 (1997).

[16] G. Gebel, "Structural evolution of water swollen perfluorosulfonated ionomers from dry membrane to solution," Polymer **41,** 5829–5838 (2000).

[17] L. Rubatat, A. L. Rollet, G. Gebel, and O. Diat, "Evidence of Elongated Polymeric Aggregates in Nafion," Macromolecules **35,** 4050–4055 (2002).

[18] K. Schmidt-Rohr and Q. Chen, "Parallel cylindrical water nanochannels in Nafion fuel-cell membranes," Nature Materials **7,** 75–83 (2008).

[19] C. K. Knox and G. A. Voth, "Probing Selected Morphological Models of Hydrated Nafion Using Large-Scale Molecular Dynamics Simulations," The Journal of Physical Chemistry B **114,** 3205–3218 (2010), pMID: 20158234.

[20] X. Wang, K. M. Beers, J. B. Kerr, and N. P. Balsara, "Conductivity and water uptake in block copolymers containing protonated polystyrene sulfonate and their imidazolium salts," Soft Matter **7,** 4446–4452 (2011).

[21] K. M. Beers and N. P. Balsara, "Design of Cluster-free Polymer Electrolyte Membranes and Implications on Proton Conductivity," ACS Macro Letters **1,** 1155–1160 (2012).

[22] C. C. Yang, E. M. W. Tsang, Z. Zhang, R. Narimani, B. J. Frisken, and S. Holdcroft, to be published .

[23] X. Wang, M. Goswami, R. Kumar, B. G. Sumpter, and J. Mays, "Morphologies of block copolymers composed of charged and neutral blocks," Soft Matter **8,** 3036–3052 (2012).

[24] S. Balog, U. Gasser, K. Mortensen, H. B. youcef, L. Gubler, and G. G. Scherer, "Structure of the ion-rich phase in DVB cross-linked graft-copolymer proton-exchange membranes," Polymer **53,** 175 – 182 (2012).

[25] G. Strobl, *The Physics of Polymers: Concepts for Understanding Their Structures and Behavior* (Springer-Verlag Berlin Heidelberg, 2007).

[26] Y. Yang and S. Holdcroft, “Synthetic Strategies for Controlling the Morphology of Proton Conducting Polymer Membranes,” Fuel Cells **5,** 171–186 (2005).

[27] I. Hamley, *The Physics of Block Copolymers*, *Oxford Science Publications* (Oxford University Press, USA, 1999).

[28] F. S. Bates and G. H. Fredrickson, “Block Copolymers—Designer Soft Materials,” Physics Today **52,** 32–38 (1999).

[29] M. Xenidou, F. L. Beyer, N. Hadjichristidis, S. P. Gido, and N. B. Tan, “Morphology of Model Graft Copolymers with Randomly Placed Trifunctional and Tetrafunctional Branch Points,” Macromolecules **31,** 7659–7667 (1998).

[30] L. Zhang, J. Lin, and S. Lin, “Effect of Molecular Architecture on Phase Behavior of Graft Copolymers,” The Journal of Physical Chemistry B **112,** 9720–9728 (2008), pMID: 18630957.

[31] S. Qi, A. K. Chakraborty, H. Wang, A. A. Lefebvre, N. P. Balsara, E. I. Shakhnovich, M. Xenidou, and N. Hadjichristidis, “Microphase Ordering in Melts of Randomly Grafted Copolymers,” Phys. Rev. Lett. **82,** 2896–2899 (1999).

[32] S. Qi, A. K. Chakraborty, and N. P. Balsara, “Microphase segregation in molten randomly grafted copolymers,” The Journal of Chemical Physics **115,** 3387–3400 (2001).

[33] M. J. Park and N. P. Balsara, “Phase Behavior of Symmetric Sulfonated Block Copolymers,” Macromolecules **41,** 3678–3687 (2008).

[34] T. E. Patten and K. Matyjaszewski, “Atom Transfer Radical Polymerization and the Synthesis of Polymeric Materials,” Advanced Materials **10,** 901–915 (1998).

[35] P. W. M. Haynes, P. David R. Lide, and P. Thomas J. Bruno, *CRC Handbook of Chemistry and Physics 2012-2013*, *CRC Handbook of Chemistry & Physics* (Taylor & Francis Group, 2012).

[36] T. J. Peckham and S. Holdcroft, “Structure-Morphology-Property Relationships of Non-Perfluorinated Proton-Conducting Membranes,” Advanced Materials **22,** 4667–4690 (2010).

[37] E. M. W. Tsang, Z. Zhang, Z. Shi, T. Soboleva, and S. Holdcroft, “Considerations of Macromolecular Structure in the Design of Proton Conducting Polymer Membranes: Graft versus Diblock Polyelectrolytes,” Journal of the American Chemical Society **129,** 15106–15107 (2007), pMID: 18004848.

[38] Z. Zhang, E. Chalkova, M. Fedkin, C. Wang, S. N. Lvov, S. Komarneni, and T. C. M. Chung, “Synthesis and Characterization of Poly(vinylidene fluoride)-g-sulfonated Polystyrene Graft Copolymers for Proton Exchange Membrane,” Macromolecules **41,** 9130–9139 (2008).

[39] R. Roe, *Methods of X-ray and Neutron Scattering in Polymer Science*, *Topics in Polymer Science* (Oxford University Press, USA, 2000).

[40] B. Warren, *X-Ray Diffraction*, *Dover Books on Physics* (Dover Publications, 1990).

[41] J. Higgins and H. Benoit, *Polymers and Neutron Scattering*, *Oxford science publications* (Oxford University Press, USA, 1997).

[42] S. Zumdahl and D. DeCoste, *Introductory Chemistry*, *Available 2011 Titles Enhanced Web Assign Series* (Cengage Learning, 2010).

[43] R. Roe, *Methods of X-Ray and Neutron Scattering in Polymer Science*, *Topics in Polymer Science* (Oxford University Press, 2000).

[44] L. Alexander, *X-ray diffraction methods in polymer science*, *Wiley series on the science and technology of materials* (Wiley-Interscience, 1969).

[45] http://www.ncnr.nist.gov/resources/sldcalc.html.

[46] R. Young and P. Lovell, *Introduction to Polymers* (CRC Press, 2009).

[47] H. Uehara, M. Kakiage, M. Sekiya, T. Yamagishi, T. Yamanobe, K. Nakajima, T. Watanabe, K. Nomura, K. Hase, and M. Matsuda, "Novel Design Solving the Conductivity vs Water-Uptake Trade-Off for Polymer Electrolyte Membrane by Bicontinuous Crystalline/Amorphous Morphology of Block Copolymer," Macromolecules **42,** 7627–7630 (2009).

[48] G. Gebel, P. Aldebert, and M. Pineri, "Structure and related properties of solution-cast perfluorosulfonated ionomer films," Macromolecules **20,** 1425–1428 (1987).

[49] T. D. Gierke, G. E. Munn, and F. C. Wilson, "The morphology in nafion perfluorinated membrane products, as determined by wide- and small-angle x-ray studies," Journal of Polymer Science: Polymer Physics Edition **19,** 1687–1704 (1981).

[50] M. Fujimura, T. Hashimoto, and H. Kawai, "Small-angle x-ray scattering study of perfluorinated ionomer membranes. 1. Origin of two scattering maxima," Macromolecules **14,** 1309–1315 (1981).

[51] M. Fujimura, T. Hashimoto, and H. Kawai, "Small-angle x-ray scattering study of perfluorinated ionomer membranes. 2. Models for ionic scattering maximum," Macromolecules **15,** 136–144 (1982).

[52] P. C. van der Heijden, L. Rubatat, and O. Diat, "Orientation of Drawn Nafion at Molecular and Mesoscopic Scales," Macromolecules **37,** 5327–5336 (2004).

[53] A. Sacc, A. Carbone, R. Pedicini, G. Portale, L. DIlario, A. Longo, A. Martorana, and E. Passalacqua, "Structural and electrochemical investigation on re-cast Nafion membranes for polymer electrolyte fuel cells (PEFCs) application," Journal of Membrane Science **278,** 105 – 113 (2006).

[54] R. B. Moore and C. R. Martin, "Chemical and morphological properties of solution-cast perfluorosulfonate ionomers," Macromolecules **21,** 1334–1339 (1988).

[55] Y. Luan, H. Zhang, Y. Zhang, L. Li, H. Li, and Y. Liu, "Study on structural evolution of perfluorosulfonic ionomer from concentrated DMF-based solution to membranes," Journal of Membrane Science **319,** 91 – 101 (2008).

[56] W. W. Doll and J. B. Lando, "Polymorphism of poly(vinylidene fluoride). III. The crystal structure of phase II," Journal of Macromolecular Science, Part B **4,** 309–329 (1970).

[57] R. Hasegawa, Y. Takahashi, Y. Chatani, and H. Tadokoro, "Crystal Structures of Three Crystalline Forms of Poly(vinylidene fluoride)," Polymer Journal **3,** 600–610 (1972).

[58] C. Ayyagari, D. Bedrov, and G. D. Smith, "Structure of Atactic Polystyrene: A Molecular Dynamics Simulation Study," Macromolecules **33,** 6194–6199 (2000).

[59] M. Zhang and T. P. Russell, "Graft Copolymers from Poly(vinylidene fluoride-co-chlorotrifluoroethylene) via Atom Transfer Radical Polymerization," Macromolecules **39,** 3531–3539 (2006).

[60] T. D. Gierke, G. E. Munn, and F. C. Wilson, "The morphology in nafion perfluorinated membrane products, as determined by wide- and small-angle x-ray studies," Journal of Polymer Science: Polymer Physics Edition **19,** 1687–1704 (1981).

[61] H. G. Haubold, T. Vad, H. Jungbluth, and P. Hiller, "Nano structure of NAFION: a SAXS study," Electrochimica Acta **46,** 1559 – 1563 (2001).

[62] "Structure alterations of perfluorinated sulfocationic membranes under the action of ethylene glycol (SAXS and WAXS studies)," Polymer **44,** 5789 – 5796 (2003).

[63] B. Loppinet and G. Gebel, "Rodlike Colloidal Structure of Short Pendant Chain Perfluorinated Ionomer Solutions," Langmuir **14,** 1977–1983 (1998).

[64] J. A. Elliott, D. Wu, S. J. Paddison, and R. B. Moore, "A unified morphological description of Nafion membranes from SAXS and mesoscale simulations," Soft Matter **7,** 6820–6827 (2011).

[65] L. Rubatat, G. Gebel, and O. Diat, "Fibrillar Structure of Nafion: Matching Fourier and Real Space Studies of Corresponding Films and Solutions," Macromolecules **37,** 7772–7783 (2004).

[66] O. Diat and G. Gebel, “Proton channels,” Nature Materials **7,** 13–14 (2008).

[67] L. Rubatat, C. Li, H. Dietsch, A. Nykanen, J. Ruokolainen, and R. Mezzenga, “StructureProperties Relationship in Proton Conductive Sulfonated PolystyrenePolymethyl Methacrylate Block Copolymers (sPSPMMA),” Macromolecules **41,** 8130–8137 (2008).

[68] P. Knychaa, M. Banaszak, M. J. Park, and N. P. Balsara, “Microphase Separation in Sulfonated Block Copolymers Studied by Monte Carlo Simulations,” Macromolecules **42,** 8925–8932 (2009).

[69] M. Goswami, B. G. Sumpter, T. Huang, J. M. Messman, S. P. Gido, A. I. Isaacs-Sodeye, and J. W. Mays, “Tunable morphologies from charged block copolymers,” Soft Matter **6,** 6146–6154 (2010).

[70] M. Goswami, R. Kumar, B. G. Sumpter, and J. Mays, “Breakdown of Inverse Morphologies in Charged Diblock Copolymers,” The Journal of Physical Chemistry B **115,** 3330–3338 (2011).

[71] H.-C. Lee, H. Lim, W.-F. Su, and C.-Y. Chao, “Novel sulfonated block copolymer containing pendant alkylsulfonic acids: Syntheses, unique morphologies, and applications in proton exchange membrane,” Journal of Polymer Science Part A: Polymer Chemistry **49,** 2325–2338 (2011).

[72] M.-P. Nieh, M. D. Guiver, D. S. Kim, J. Ding, and T. Norsten, “Morphology of Comb-Shaped Proton Exchange Membrane Copolymers Based on a Neutron Scattering Study,” Macromolecules **41,** 6176–6182 (2008).

[73] J. Ding, C. Chuy, and S. Holdcroft, “Enhanced Conductivity in Morphologically Controlled Proton Exchange Membranes: Synthesis of Macromonomers by SFRP and Their Incorporation into Graft Polymers,” Macromolecules **35,** 1348–1355 (2002).

[74] J. Ding, C. Chuy, and S. Holdcroft, “A Self-organized Network of Nanochannels Enhances Ion Conductivity through Polymer Films,” Chemistry of Materials **13,** 2231–2233 (2001).

[75] D. J. Kinning, E. L. Thomas, and L. J. Fetters, “Morphological studies of micelle formation in block copolymer/homopolymer blends,” The Journal of Chemical Physics **90,** 5806–5825 (1989).

[76] D. J. Kinning and E. L. Thomas, “Hard-sphere interactions between spherical domains in diblock copolymers,” Macromolecules **17,** 1712–1718 (1984).

[77] J. K. Percus and G. J. Yevick, “Analysis of Classical Statistical Mechanics by Means of Collective Coordinates,” Phys. Rev. **110,** 1–13 (1958).

[78] G. Gebel and J. Lambard, “Small-Angle Scattering Study of Water-Swollen Perfluorinated Ionomer Membranes,” Macromolecules **30,** 7914–7920 (1997).

[79] P. Debye and A. M. Bueche, “Scattering by an Inhomogeneous Solid,” Journal of Applied Physics **20,** 518 –525 (1949).

[80] E. M. W. Tsang, Z. Shi, and S. Holdcroft, “Ionic Purity and Connectivity of Proton-Conducting Channels in Fluorous-Ionic Diblock Copolymers,” Macromolecules **44,** 8845–8857 (2011).

[81] Z. Shi and S. Holdcroft, “Synthesis and Proton Conductivity of Partially Sulfonated Poly([vinylidene difluoride-co-hexafluoropropylene]-b-styrene) Block Copolymers,” Macromolecules **38,** 4193–4201 (2005).

[82] D. Gromadzki, P. ernoch, M. Janata, V. Kdela, F. Nallet, O. Diat, and P. tpnek, “Morphological studies and ionic transport properties of partially sulfonated diblock copolymers,” European Polymer Journal **42,** 2486 – 2496 (2006).

[83] D. Lanson, F. Ariura, M. Schappacher, R. Borsali, and A. Deffieux, “Comb Copolymers with Polystyrene and Polyisoprene Branches: Effect of Block Topology on Film Morphology,” Macromolecules **42,** 3942–3950 (2009).

[84] L. J. Fetters, N. Hadjichristidis, J. S. Lindner, and J. W. Mays, “Molecular Weight Dependence of Hydrodynamic and Thermodynamic Properties for Well-Defined Linear Polymers in Solution,” Journal of Physical and Chemical Reference Data **23,** 619–640 (1994).

[85] A. Eisenberg, B. Hird, and R. B. Moore, “A new multiplet-cluster model for the morphology of random ionomers,” Macromolecules **23,** 4098–4107 (1990).

[86] M. A. Hickner, “Water-mediated transport in ion-containing polymers,” Journal of Polymer Science Part B: Polymer Physics **50,** 9–20 (2012).

[87] A.-C. Dupuis, “Proton exchange membranes for fuel cells operated at medium temperatures: Materials and experimental techniques,” Progress in Materials Science **56,** 289 – 327 (2011).

[88] T. J. Peckham, J. Schmeisser, and S. Holdcroft, “Relationships of Acid and Water Content to Proton Transport in Statistically Sulfonated Proton Exchange Membranes: Variation of Water Content Via Control of Relative Humidity,” The Journal of Physical Chemistry B **112,** 2848–2858 (2008), pMID: 18288828.

[89] K.-V. Schubert, R. Strey, S. R. Kline, and E. W. Kaler, “Small angle neutron scattering near Lifshitz lines: Transition from weakly structured mixtures to microemulsions,” The Journal of Chemical Physics **101,** 5343–5355 (1994).

[90] M. Yoonessi, H. Heinz, T. D. Dang, and Z. Bai, "Morphology of sulfonated polyarylenethioethersulfone random copolymer series as proton exchange fuel cells membranes by small angle neutron scattering," Polymer **52,** 5615 – 5621 (2011).

[91] J. M. Serpico, S. G. Ehrenberg, J. J. Fontanella, X. Jiao, D. Perahia, K. A. McGrady, E. H. Sanders, G. E. Kellogg, and G. E. Wnek, "Transport and Structural Studies of Sulfonated StyreneEthylene Copolymer Membranes," Macromolecules **35,** 5916–5921 (2002).

[92] N. C. Zhou, C. D. Chan, and K. I. Winey, "Reconciling STEM and X-ray Scattering Data To Determine the Nanoscale Ionic Aggregate Morphology in Sulfonated Polystyrene Ionomers," Macromolecules **41,** 6134–6140 (2008).

[93] M. Yoonessi, T. D. Dang, H. Heinz, R. Wheeler, and Z. Bai, "Investigation of nanostructures and properties of sulfonated poly(arylenethioethersulfone) copolymer as proton conducting materials by small angle neutron scattering," Polymer **51,** 1585 – 1592 (2010).

[94] L. M. Hall, M. E. Seitz, K. I. Winey, K. L. Opper, K. B. Wagener, M. J. Stevens, and A. L. Frischknecht, "Ionic Aggregate Structure in Ionomer Melts: Effect of Molecular Architecture on Aggregates and the Ionomer Peak," Journal of the American Chemical Society **134,** 574–587 (2012).

[95] Y. S. Kim and B. S. Pivovar, "Moving beyond mass-based parmeters for conductivity analysis of sulfonated polymers," Annu. Rev. Chem. Biomol. Eng. **1,** 123 (2010).

[96] T. J. Peckham, J. Schmeisser, M. Rodgers, and S. Holdcroft, "Main-chain, statistically sulfonated proton exchange membranes: the relationships of acid concentration and proton mobility to water content and their effect upon proton conductivity," J. Mater. Chem. **17,** 3255–3268 (2007).

[97] K. Schmidt-Rohr, "Simulation of small-angle scattering curves by numerical Fourier transformation," Journal of Applied Crystallography **40,** 16–25 (2007).

[98] M. Eikerling, A. A. Kornyshev, and U. Stimming, "Electrophysical Properties of Polymer Electrolyte Membranes: A Random Network Model," The Journal of Physical Chemistry B **101,** 10807–10820 (1997).

[99] T. Weissbach, E. M. W. Tsang, A. C. C. Yang, R. Narimani, B. J. Frisken, and S. Holdcroft, "Structural effects on the nano-scale morphology and conductivity of ionomer blends," J. Mater. Chem. pp. – (2012).

[100] M. Kotlarchyk and S.-H. Chen, "Analysis of small angle neutron scattering spectra from polydisperse interacting colloids," The Journal of Chemical Physics **79,** 2461–2469 (1983).

[101] M. Plischke and B. Bergersen, *Equilibrium Statistical Physics* (World Scientific, 2006).